Numerical Modelling of Track-Ground Response Induced by Train Passage

Kaitai Dong

School of Energy, Geoscience, Infrastructure and Society
Heriot-Watt University

This dissertation is submitted for the degree of
Doctor of Philosophy

March 2020

Thesis Outcomes

This work has led to 3 journal papers and 5 conference papers by the author.

Journal papers

1. **Dong, K.**, Connolly, D., Laghrouche, O., Woodward, P. and Alves Costa, P. (2019) Non-linear soil behavior on high speed rail lines, *Computers & Geotechnics*, 112, 302-318, https://doi.org/10.1016/j.compgeo.2019.03.028

2. **Dong, K.**, Connolly, D., Laghrouche, O., Woodward, P. and Alves Costa, P. (2018) The stiffening of soft soils on railway lines, *Transportation Geotechnics*, 17, 178-191, https://doi.org/10.1016/j.trgeo.2018.09.004

3. Connolly, D., **Dong, K.**, Alves Costa, P. and Woodward, P. (2019) High speed railway ground dynamics: a multi-model analysis, *International Journal of Rail Transportation*, 1-28. https://doi.org/10.1080/23248378.2020.1712267

Conference papers

1. **Dong, K.**, Connolly, D., Laghrouche, O., Woodward, P., and Alves Costa, P. (2019) Optimising soil stiffness on high speed rail lines to prevent vibration. In *Proceedings of the 26th International Congress on Sound and Vibration* https://iiav.org/archives_icsv/2019_icsv26/content/papers/papers/full_paper_55_20190122104743471.pdf

2. **Dong, K.**, Connolly, D., Laghrouche, O., Woodward, P. Ho, C. and Alves Costa, P. (2018) The effect of soil non-linearity on mixed traffic railway lines: Passenger vs Freight loads, In *Proceedings of GeoShanghai 2018 International Conference*, 227-236, https://doi.org/10.1007/978-981-13-0011-0_25

3. **Dong, K.**, Connolly, D., Laghrouche, O., Woodward, P., and Alves Costa, P. (2018) Non-linear soil behavior on freight and passenger lines, *WIT Transactions on the Built Environment*, 181, 507-516, https://www.witpress.com/Secure/elibrary/papers/CR18/CR18045FU1.pdf

4. **Dong, K.**, Connolly, D., Laghrouche, O., Woodward, P., and Alves Costa, P. (2018) The effect of non-linear soil behavior on mixed traffic railway lines, *Numerical Methods in Geotechnical Engineering IX*, Volume 2, 1445-1449, https://www.taylorfrancis.com/books/e/9780429446924/chapters/10.1201/9780429446924-68

5. **Dong, K.**, Connolly, D., Laghrouche, O., Woodward, P., and Alves Costa, P. (2017) Earthwork strategies to reduce dynamic amplification on new high-speed rail lines, *International Railway Conference*, Edinburgh, UK

Acknowledgements

The work described in this thesis was carried out at the School of Energy, Geoscience, Infrastructure and Society, Heriot-Watt University, between October 2015 and August 2019. The project was initially proposed by **Dr. David Connolly**, who also acted as my main research supervisor. I am deeply indebted to him for offering me the scholarship to take on this project, providing me with endless advice, guidance, encouragement and answering my questions whenever I had doubts on any subject. I started this project with no knowledge in railway engineering, but I now have developed in-depth understanding of the topic and also gained an extensive insight into the railway industry, in general. None of these would have been achieved without his support.

I would also like to thank **Prof. Omar Laghrouche** for his constant support. I received help, constructive suggestions and encouragement from him throughout my project. His sincerity and dedication will always influence me in the next chapter of my life. I would also like to thank **Prof. Peter Woodward**, who was the Head of the Institute for Infrastructure and Environment when I arrived at Heriot-Watt University, for his trust, encouragement and appreciation. I am grateful for the generous financial support you provided to help me get through my PhD.

I would also like to offer my sincere gratitude to **Dr. Pedro Alves Costa** for the selfless share of his research results and constant guidance in the development of the Thin-Layer Method (TLM). I learned substantially through the discussions we had and the technical support you gave me. I also thank **Prof. Pedro Galvin** for the detailed explanation and countless help on the development of 2.5D FEM model. I am truly blessed to have all those experts available to help me and guide me throughout my project.

Special thanks go to my colleague and friend **Mr. Ahmet Esen** for always being there for me whenever I had difficulties and concerns, and also for sharing his expertise in AutoCAD and making the research an enjoyable experience for me.

Finally, I wish to thank my parents. I would never have been in a position to produce this thesis without their encouragement and support.

Thank you so much for everything that has turned it into an amazing journey.

Abstract

The global railway network is undergoing rapid expansion, with train vehicles becoming faster. Increases to operational train speed mean that it is more likely vehicles will induce larger dynamic effects within the supporting track and soil structure. At the same time, it is challenging to determine the type and depth of ground remediation required to reduce the track deflections. The present dissertation addresses the subject of vibrations induced by the passage of high-speed trains. The main aim of this work is to develop numerical tools that allow analysing track behaviour efficiently, investigating material non-linearity effect on the track dynamics, and also assessing the soil remediation strategies.

Firstly, A semi-analytical model is proposed and designed for the dynamic analysis of track-ground vibrations induced by high speed rails. The model uses analytical expressions for the railroad track, coupled to a thin-layer element formulation for the ground. The model is validated using a combination of experimental railway field data, published numerical data and a commercial finite element package. It is shown to predict track and ground behaviour accurately for a range of train speeds. Moreover, it is used to investigate the effect of soil replacement/improvement below railway lines due to its low computational costs.

Secondly, new insights are given to non-linear subgrade behaviour on high speed railway track dynamics. Built upon the proposed semi-analytical model, material non-linearity is accounted for using a 'linear equivalent' approach which iteratively updates the soil material properties. The model is validated using published datasets and in-situ field data. Four case studies are used to investigate the non-linear behaviour, each with contrasting subgrade characteristics. It is found that the critical velocity can shift to as low as 80% of the linear case, while rail deflections are up to 30% higher, depending on the material properties.

Finally, a novel 2.5D FEM-BEM-TLM model is developed to include material non-linearity for both track structure and soil. The track structure is represented by a finite element model and the soil responses are obtained from boundary element model and thin-layer model. Material non-linearity is included using the

proposed 'linear equivalent' approach. The model is validated against the commercial FE software ABAQUS and numerical results from published literature. Two case studies are conducted to shed light upon the full material non-linearity effect on the dynamic track-ground responses from the train passage, revealing the necessity of its use, especially when high strains occur.

Table of Contents

Thesis Outcomes ii

Acknowledgements iii

Abstract v

List of Figures xi

List of Tables xvi

1 Introduction 1

1.1 Motivation of the research . . . 1

1.2 Objectives of the research . . . 2

1.3 Outline of the thesis . . . 3

2 Literature Review 5

2.1 Introduction . . . 5

2.2 Wave propagation . . . 5

2.3 Critical velocity . . . 7

2.4 Train-induced vibration models . . . 9

2.4.1 Analytical models . . . 10

2.4.2 Semi-analytical models . . . 12

2.4.3 Numerical models . . . 14

2.5 Soil non-linearity . . . 22

2.5.1 Experimental approach . . . 22

2.5.2 Numerical approach . . . 24
2.6 Ballast/Subballast non-linearity . . . 25
2.6.1 Experimental approach . . . 26
2.6.2 Numerical approach . . . 29
2.7 Conclusion . . . 31

3 Fully linear track and subgrade behaviour 32

3.1 Introduction . . . 32
3.2 Model description . . . 34
3.2.1 Track model . . . 34
3.2.2 Soil model . . . 39
3.3 Model validation . . . 44
3.3.1 Soil replacement validation . . . 44
3.3.2 Numerical validation . . . 46
3.3.3 Experimental validation . . . 50
3.4 Soil replacement strategies . . . 52
3.4.1 Soil case 1 . . . 53
3.4.2 Soil case 2 . . . 56
3.4.3 Soil case 3 . . . 58
3.5 Discussion . . . 60
3.6 Conclusion . . . 61

4 Non-linear subgrade behaviour 62

4.1 Introduction . . . 62
4.2 Equivalent linear model . . . 63
4.2.1 Brief introduction . . . 63
4.2.2 Equivalent linear formulation . . . 64
4.3 Model validation . . . 66
4.3.1 Soil stress validation . . . 66
4.3.2 Experimental validation . . . 67
4.4 Numerical analysis . . . 74

4.4.1 Soil case 1 . . . 76
4.4.2 Soil case 2 . . . 80
4.4.3 Soil case 3 . . . 84
4.4.4 Soil case 4 . . . 86
4.5 Discussion . . . 87
4.6 Linear and non-linear comparison . . . 89
4.7 Conclusion . . . 91

5 Fully non-linear track and subgrade behaviour 92
5.1 Introduction . . . 92
5.2 2.5D FE model . . . 94
5.2.1 General equilibrium equations . . . 94
5.2.2 Element formulation . . . 96
5.3 2.5D FEM-BEM-TLM model . . . 99
5.3.1 Generalities . . . 100
5.3.2 2.5D BEM-TLM formulation . . . 101
5.3.3 Equivalent linear track model . . . 106
5.4 Model validation . . . 108
5.4.1 Model validation 1 . . . 108
5.4.2 Model validation 2 . . . 111
5.4.3 Model validation 3 . . . 113
5.5 Numerical analysis . . . 114
5.5.1 Case study 1 - Freight train . . . 117
5.5.2 Case study 2 - High-speed train . . . 119
5.6 Discussion . . . 121
5.7 Conclusion . . . 122

6 Conclusions and recommendations for future work 123
6.1 Conclusions . . . 123
6.2 Recommendations for future work . . . 125

References 127

Appendix A Dynamic Flexibility Matrix 144

Appendix B Equivalent Stiffness Formulation 147

List of Figures

2.1 Generation and propagation of the vehicle induced vibrations 15

2.2 Schematic illustration of (a) 3D FE model (b) 3D BEM (surface) 17

2.3 Railway track as a periodic structure, the basic periodict finite element slice is on the left (Arlaud et al. [11]) 20

2.4 Schematic illustration of 2.5D BEM and/or FEM 21

2.5 Strain-stress records of different stages under a cyclic loading (Iwasaki et al. [88]) 23

2.6 Shear modulus and damping ratio against shear strain (Iwasaki et al. [88]) 23

2.7 Triaxial test setup for ballast material (Dyvik and Kaynia [54]) 27

2.8 Cross-section of the facility (Thom et al. [165]) 28

2.9 Servo-controlled hydraulic actuators (Thom et al. [165]) 28

2.10 End-view diagram of the testing facility designed by Aursudkij et al. [14] 29

3.1 Schematic illustration of the analytical track model coupled with linear TLM ground model 33

3.2 Ballasted track model structure 35

3.3 Slab track model structure 36

3.4 Illustration of scaling factor of the track-ground coupling for ballasted track 38

3.5 Illustration of scaling factor of the track-ground coupling for slab track 38

3.6 Schematic drawing of the procedure of the vertical discretization and domain transform in the thin-layer method 39

3.7 Discretization into thin layers with quadratic interpolation 40

3.8 Layout of soil replacement geometry 45

3.9 Comparison between simplified and detailed soil replacement geometry (a) static rail receptance excitation; (b) moving load excitation time history 46
3.10 Schematic representation of track-ground interaction model 47
3.11 Train boogie loads applied in the numerical simulation 47
3.12 Track displacement for Southbound train at 70km/h (case 1) in timn domain (a) and frequency domain (b) 49
3.13 Track displacement for Northbound train at 185km/h (case 1) in timn domain (a) and frequency domain (b) 49
3.14 Track displacement for Southbound train at 200km/h (case 1) in timn domain (a) and frequency domain (b) 49
3.15 Geometry and mechanical properties of the Alfa-Pendular train 50
3.16 Rail displacement due to the train passage in both time content (a) and in frequency content (b) 51
3.17 Vertical sleeper velocity due to the train passage in both time content (a) and in frequency content (b) 52
3.18 Maximum vertical rail displacement for Soil 1. (a) Ballasted track; (b) Slab track 54
3.19 Maximum vertical rail displacement vs train speed, for Soil 1 with 1m of soil replacement. (a) Ballasted track; (b) Slab track; Dashed black line represents train speed 55
3.20 Stress time history comparison at the surface for ballasted track. (a) c=20m/s (b) c=92m/s . 56
3.21 Maximum vertical rail displacement for Soil 2. (a) Ballasted track; (b) Slab track 57
3.22 Maximum vertical rail displacement vs train speed, for Soil 2 with different depths of soil replacement strategies. (a) Ballasted track; (b) Slab track 57
3.23 Rail displacement comparisons for Soil 2. (a) Original soil; (b) 5m depth of improvement . 58
3.24 Schematic diagram of the slab track used in the simulation overlaying on the soil 59
3.25 Maximum vertical rail displacement for Soil 3. (a) Ballasted track; (b) Slab track 59
3.26 Vertical stress vs Depth for Soil case 3. (a) Ballasted track; (b) Slab track 60

4.1 Schematic illustration of the analytical track model coupled with non-linear TLM ground model 63
4.2 Strain-stress path during cyclic loading 64
4.3 Schematic diagram of Chen's validation model 66

4.4 Comparisons of the dynamic stresses of an element at (0, 0, -2m) underneath the moving load 67

4.5 Geometric dimensions at the Ledsgard site 68

4.6 Geometric and mechanical properties of the X2000 train 69

4.7 (a) Shear modulus reduction curves; (b) Damping ratio for different soil layers at Ledsgard 71

4.8 Measured and simulated time histories of track displacements for different train speeds: (a) c=70km/h; (b) c=140km/h; (c) c=180km/h; (d) Peak displacements versus train speeds (Southbound) 73

4.9 (a) Embankment shear modulus reduction process at each iteration step at speed of 204km/h; (b) Young's modulus comparison over the depth for speeds of 70km/h and 204km/h 73

4.10 Variation of maximum octahedral shear strain with depth for train speed at (a) 70km/h; (b) 204km/h 74

4.11 Wave speeds demonstration for different soil conditions 75

4.12 Soil case 1 comparisons of linear and equivalent non-linear DAF curves of (a) rail displacements (b) ballast velocity (c) octahedral strain at Point A (d) octahedral strain at Point B 77

4.13 Maximum octahedral strain vs depth for c = 10 m/s and c = 80 m/s for non-linear Soil case 1 78

4.14 Stress history of Point A underneath the centre line of the track structure at the speeds of (a) c = 10m/s (b) c = 80m/s (c) c = 130m/s 79

4.15 DAF curves for stress components (peak-to-peak) at Point A in Soil case 1 80

4.16 Soil case 2, (a) comparisons of linear and non-linear DAF rail displacement curves, (b) Maximum (non-linear) shear strain vs depth for c = 10 m/s and c = 90 m/s 81

4.17 Soil case 2 comparisons of linear and non-linear DAF curves of maximum octahedral strain (a) at Point A (b) at Point B 81

4.18 Stress path followed at point A during the load passage with different speeds (a) c = 10 m/s (b) c = 90m/s (c) c = 110 m/s 83

4.19 Soil case 3, (a) comparisons of linear and non-linear DAF rail displacement curves, (b) Maximum (non-linear) shear strain vs depth for c = 10 m/s and c = 80 m/s 84

4.20 Soil case 3 comparisons of linear and non-linear DAF curves of maximum octahedral strain (a) at Point A (b) at Point B 85

4.21 Normalised ground surface contours (a) Linear: c = 10 m/s (b) Non-linear: c = 10 m/s (c) Linear: c = 80 m/s (d) Non-linear: c = 80 m/s 86

4.22 Soil case 4, (a) comparisons of linear and non-linear DAF rail displacement curves, (b) Maximum (non-linear) shear strain vs depth for c = 10 m/s and c = 150 m/s 87

4.23 (a) Non-linear soil improvement quantification, (b) Corresponding DAF curves for 1m improvement 90

5.1 Schematic illustration of the proposed 2.5D FEM-BEM-TLM model 93

5.2 Schematic plot of an 8-node quadratic element (a) and its representation in the local coordinate system (b) 97

5.3 Schematic diagram of the coupling between FEM and BEM-TLM domain 100

5.4 Ground under pressure applied to an area inscribed on the free surface 102

5.5 Schematic diagram of the layout of the matrix [T] 104

5.6 (a) Shear modulus reduction curve; (b) Damping ratio elevation curve obtained from large-scale triaxial tests (Dyvik and Kaynia [54]) 107

5.7 Schematic diagram of the embankment structure 109

5.8 Embankment nodal displacements comparison between FE and ABAQUS model for frequencies (a) *real*(u) at f = 5Hz; (b) *imag*(u) at f = 5Hz; (c) *real*(u) at f = 30Hz; (d) *imag*(u) at f = 30Hz 110

5.9 Schematic representation of the slab-subgrade model 111

5.10 Slab nodal displacements comparison between 2.5D FEM-BEM-TLM and ABAQUS model at f = 5Hz (a) *real*(u) (b) *imag*(u) 112

5.11 Slab nodal displacements comparison between 2.5D FEM-BEM-TLM and ABAQUS model at f = 30Hz (a) *real*(u) (b) *imag*(u) 113

5.12 Schematic representation of the slab-subgrade model 114

5.13 Schematic representation of the train-embankment-ground model 116

5.14 Comparisons between non-linear subgrade and non-linear track-subgrade model (a) Octahedral strain vs depth (b) Young's modulus reduction with depth 118

5.15 Track displacements due to the passage of freight train in (a) time domain (b) frequency domain 118

5.16 Track velocities due to the passage of freight train in (a) time domain (b) frequency domain 119

5.17 (a) Linear track strain variations (b) Non-linear track strain variations 119

5.18 Comparisons between non-linear subgrade and non-linear track-subgrade model (a) Octahedral strain vs depth (b) Young's modulus reduction with depth 120

5.19 Track displacements due to the passage of high-speed train in (a) time domain (b) frequency domain 120

5.20 Track velocities due to the passage of high-speed train in (a) time domain (b) frequency domain 121

A.1 The coordinate system with horizontally parallel layers 144

List of Tables

2.1 Maximum operational speeds of in-service high speed rail lines by country (Loubinoux [124]) 9

3.1 Soil properties used in the simulation for train velocity of 70km/h and 200km/h (Kaynia et al. [100]) . . . 47

3.2 Velocity and direction of the compared simulation cases . . . 48

3.3 Soil properties . . . 53

3.4 Track properties (ballasted track and slab track) . . . 53

3.5 Rail displacement improvement in percentage terms for Soil 1 at a train speed of 330km/h 54

3.6 Rail displacement improvement in percentage terms for Soil 2 at a train speed of 330km/h 57

3.7 Rail displacement improvement in percentage terms for Soil 3 at a train speed of 330km/h 60

4.1 Properties of the beam and the ground for Chen's validation . . . 66

4.2 Track parameters at the Ledsgard site . . . 69

4.3 Velocity and direction of the compared simulation cases . . . 71

4.4 Soil properties used in the case studies . . . 75

4.5 Ballasted track properties . . . 76

4.6 The magnitude of maximum stress components (peak-to-peak) at various speeds . . . 80

4.7 Summary of effect of non-linearity on rail displacements and critical velocity . . . 88

5.1 Shape functions of 8-node elements . . . 97

5.2 Properties of the embankment for model 1 . . . 109

5.3 Properties of the slab and subgrade for model 2 . . . 111

5.4 Properties of the embankment . . . 117

5.5 Load information for the case study 117

5.6 Summary of effect of full material non-linearity on track-ground responses 122

Chapter 1

Introduction

The global railway network is undergoing rapid expansion, with train vehicles becoming faster and heavier. This is problematic because high axle loads cause excessive track deflection, especially on soft soil sites. Similarly, increased dynamic track-ground amplification occurs when the train speed approaches the ground critical speed. Elevated levels of track dynamic are undesirable on railway lines due to the fact that they cause safety concerns and result in accelerated track degradation. One example of where high dynamic track amplification was recorded is in Sweden, where shortly after the opening of a new high speed line, large deflections were measured in the track (Takemiya [161], Kaynia et al. [100], Madshus and Kaynia [128]). This was expensive to remediate, requiring a combination of speed restrictions and soil stiffening.

When designing lower speed lines it is important to consider the static stiffness of the track-ground system, however for high speed lines, the dynamic stiffness of the system must also be considered due to high levels of wave effects. Therefore, it is important to have a methodology capable of investigating and modelling the track dynamics, ensuring track deflections meet desired tolerances. This research aims to develop a better understanding of track/ground responses from the railway lines and propose a novel methodology where Thin-Layer Method (TLM) is adopted and combined with other analytical and numerical models to generate new insights into the track dynamics problem.

1.1 Motivation of the research

High speed railway track and earthwork structures experience varied levels of dynamic amplification depending upon train speed. It brings the challenge when designing track and earthwork structures to

protect against dynamic amplification due to the complexity of wave propagation within both track and soil structures. This problem is of increasing importance for the following reasons:

- **Rapid expansion and increasing usage of railways**: Nowadays the development of railway lines has prompted the change in the choice of public transportation. In comparison, trains have lower carbon dioxide emission than airplanes, and are more sustainable and faster than private vehicles. There has been an increasing number of people using railways in the past decade due to its capacity, convenience and eco-friendliness. It is key to delivering passengers great travel experience and satisfaction.
- **Environmental impacts**: The consequences of relentlessly increasing traffic induce adverse effects on human health and both the local and global environment. The environmental impacts railways have are considerably less than both road and air travel. Therefore, a substantial shift of passengers from road and air to rail would benefit everyone through reduced congestion and less damage to the environment.
- **Economic concerns**: Frequent exposure to large deflections is likely to cause rail unevenness and track degradation, which leads to increasing costs on maintenance and renewal. It is reported that Network Rail UK spent £1.3bn on maintenance of its railway lines across the UK in 2017 (Carne [29]). Therefore, it is of critical importance to come up with more sustainable rail designs.

With growing construction, environment and finance concerns, it is of critical importance to investigate the effect of vibrations induced by railway lines and provide practical solutions for engineers and rail designers.

1.2 Objectives of the research

The present dissertation investigates the effect of vibrations generated by the passage of high-speed trains. The main objective of this thesis is to develop a numerical tool capable of predicting the vibrations generated by moving vehicles in an efficient and accurate way. The purpose of the numerical tool is to provide the practitioners with a framework for investigations, which at the beginning of the PhD activities was not available. To fulfil the main goal of the research, the following specific objectives are achieved:

1. **Numerical model with linear material properties**: Most existing numerical models for full track behaviour analysis are computationally costly. This research work has led to successful development of

an efficient numerical model to rapidly calculate dynamic, multi-layered soil response in the presence of ballast and slab track structures under the assumption of linear material behaviour. It can be an effective tool to identify the critical velocity and investigate its effect rapidly and accurately.

2. **Numerical model with non-linear material properties**: A challenge with the majority of analytical and numerical approaches proposed for railway modelling is the assumption of linear elastic material behaviour. However, when the train speed is high, large strains are often induced in the soil and track, thus causing non-linear stiffness and damping behaviour. This research work also gives new insights into non-linear track and subgrade behaviour on railway track dynamics, especially the change of critical velocity and dynamic amplification effect.

3. **Soil remediation/replacement strategies**: Soil replacement or improvement is commonly used on new railway lines to increase track stiffness. However this is expensive. Therefore, this research has utilised models capable of rapidly assessing the effect of different soil improvement depths and stiffnesses on track behaviour to optimise soil replacement with respect to construction cost.

1.3 Outline of the thesis

This thesis comprises six chapters in total.

Chapter 1 includes a brief introduction of some infrastructure problems faced in the railway industry and the motivations behind this research work. A number of objectives are brought forward, followed by the outline of this thesis.

Chapter 2 reviews the literature relevant to the work presented in the following chapters. Particularly, it reviews the research developments on the modelling of dynamic responses from the passage of trains. It covers the analytical, semi-analytical and numerical approaches, both in time and wavenumber-frequency domains. Material non-linearity is also introduced in terms of experimental and numerical approaches.

Chapter 3 comprises a comprehensive development of TLM formulations and then proposes a linear semi-analytical model, which couples TLM with analytical track solutions, to predict the track responses and determine the critical speed. It includes both ballasted and slab track solutions. The proposed model is validated against the results of Madshus and Kaynia [128] and is applied to analyse different soil replacement strategies.

Chapter 4 is built upon the work carried out in Chapter 3. It takes into account the soil non-linearity by considering an equivalent linear analysis to iteratively update the material properties. The proposed non-linear model is validated against the published data from Chen et al. [32] and in-situ data obtained from the Ledsgard site in Sweden (Alves Costa et al. [3], Shih et al. [157]). Four case studies are conducted to investigate non-linear behaviour, each with contrasting subgrade characteristics.

Chapter 5 provides a thorough development of a novel 2.5D FEM-BEM-TLM model that enables to include full material non-linearity for track response prediction. The model is validated by the commercial FE software ABAQUS and published work from Chen et al. [32]. Two case studies are compared using the proposed non-linear track and subgrade model to emphasize the impact of full material non-linearity on the track and soil responses.

Chapter 6 summarises the results of this research and provides suggestions for future work.

Chapter 2

Literature Review

2.1 Introduction

Railways are a solution to traffic congestion and environmental pollution, however one concern is the issue of noise and vibration. Much time and effort have been spent with the aim of mitigating vibrations in the vehicle itself while, at the same time, improving passengers comfort and satisfaction. The vibration levels are merely a function of the forces exerted by the train. Therefore, it is crucial to model the vehicle characteristics correctly, in order to understand the vibration generation mechanisms and predict the railway vibration.

This chapter aims to give a comprehensive review of vehicle modelling methodologies and provide a resource for further research. A brief introduction of wave propagation mechanism and critical velocity effect is given in Section 2.2 and Section 2.3, followed by a comprehensive review of the research developments on the vehicle dynamic response modelling. Section 2.4 includes the analytical, semi-analytical and numerical approaches that have been proposed in the past, both in time and frequency domain. In the end, Section 2.5 and Section 2.6 review the experimental and numerical material non-linearity approaches for soil and ballast/subballast respectively. Section 2.7 draws the conclusion for this chapter.

2.2 Wave propagation

The pioneering work of studying the response of an isotropic and homogeneous elastic half-space to point loads is introduced by Lamb and it contains the basis of development of the analytical solution on sources

and transmission paths in soils. The principal features of the response of an elastic half-space to point load are examined by Barkan [17] and Richart et al. [145].

When an oscillating point load is applied to the surface of an elastic half-space, three types of waves are generated from the loading point. One is a surface wave, often referred to as Rayleigh wave (or 'R-wave'), of which horizontal and vertical magnitudes decline exponentially with the coordinate normal to the surface. However, in the far field, it decreases along the surface at a rate inversely proportional to the square root of the surface distance. The other two waves are termed body waves, i.e. the compression wave (or 'P-wave') and the shear wave (or 'S-wave'). Unlike the Rayleigh wave, the magnitudes of both body waves fall off in a manner inversely proportional to the spherical distance from the source point. When monitored on the surface, the body waves' manigutdes decrease in a way inversely proportional to the square of the surface distance. Therefore, at the surface, the body waves will be of mcuh smaller magnitudes than the Rayleigh waves. It is also of interest to mention that, for a small rigid disk vibrating on a half-space surface, 67% of the input energy goes into Rayleigh waves, 26% into S-waves, and only 7% into P-waves (Gutowski and Dym [73]). As a result, Rayleigh waves are of critical importance in railway studies because they will carry the majority of excitation energy from a passing train, hence Rayleigh waves are most likely to cause vibration effects on both the railway lines and nearby structures.

The Rayleigh wave is the slowest of the three wave types and the P-wave is the fastest, with the speed of S-wave being in between (i.e. $c_R < c_S < c_P$). Typically, the ground is comprised of several layers, each one with specific properties. Given the assumption of the elastic and linear behaviour for each layer, then the two fundamental wave speeds of the corresponding layer i, i.e., $c_{P,i}$ (P-wave) and $c_{S,i}$ (S-wave), can be defined as follow:

$$c_{P,i} = \sqrt{\frac{2G_i + \lambda_i}{\rho_i}} \tag{2.1}$$

and

$$c_{S,i} = \sqrt{\frac{G_i}{\rho_i}} \tag{2.2}$$

Where G_i is the shear modulus (i being the index of the studied layer), ρ_i is the density, and λ_i is first Lame parameter which can be obtained from:

$$\lambda_i = \frac{E_i \nu_i}{(1+\nu_i)(1-2\nu_i)} \tag{2.3}$$

Where E_i represents its Young's modulus and ν_i stands for Poisson's ratio. For linear elastic media, the Rayleigh wave speed can be approximated as:

$$c_{R,i} = \frac{0.862 + 1.14\nu_i}{1+\nu_i} c_{S,i} \tag{2.4}$$

It can be observed from Equation 2.4 that Rayleigh waves occur with a wave speed that is slightly lower than the shear wave speed. The velocity of a surface wave in a layered ground is determined by frequency. Moreover, soil damping is found to play an important role in influencing the soil response (Thompson [166]). Therefore, its modelling methodology relies on the simulation approach. Frequency domain simulation can work with both hysteretic and viscous damping models, while time domain approach is limited to viscous damping models only.

2.3 Critical velocity

With increasing train speed, the amplitude of the track vibration can become very large. At Stilton Fen, England, measurements on rail deflections were carried out over different train speeds. It revealed that the track deflection reached 12 mm at a speed of 185 km/h, which almost doubled the response at lower speed (Hunt [81]). In 1998, an extensive study was conducted by the Swedish State Railways at a rail line site in Ledsgard, Sweden. The vibrations of the rail, embankment and ground induced by the passage of an X-2000 train were of very high levels when the train speed approached 200 km/h. It showed that the maximum downward rail deflection reached 15-20 mm, which exceeded the safety limits of train operation by a large extent (Kaynia et al. [100] and Madshus and Kaynia [128]). Since then, the investigation and assessment of the critical velocity has become an important issue for railway engineering because large responses from the passage of trains might lead to damages in the track components and further cause environmental impact on the buildings nearby (Sheng et al. [152], Thompson [166], Connolly et al. [36] and Auersch [13]).

Critical velocity can also be studied using simple track models. Eason [55] firstly discovered that the displacement was amplified to a large extent on a semi-infinite homogeneous isotropic elastic solid through an analytical model, when the speed of a moving point load approached the Rayleigh wave speed. A more

complex model, which used an Euler-Bernoulli elastic beam, to represent rail and sleeper, was introduced by Krylov [111, 112] and it was also indicated that the large rail displacement would occur when the load speed was approaching the Rayleigh wave speed. Furthermore, Dieterman and Metrikine [44, 45] discovered two critical velocities for a beam on a homogeneous half-space. The beam was used to replace the track and embankment. It was revealed that the first critical velocity was very close to the Rayleigh wave speed. However, the other critical velocity was slightly lower, which was mainly determined by the bending stiffness and the mass of the beam (Dieterman and Metrikine [44, 45]).

A semi-analytical approach was proposed by Alves Costa et al. [5] and Mezher et al. [133] who modelled the track responses when the track is laid on a layered soil. It included soil critical velocity as a contribution to the dynamic effect. Two distinctive critical velocities were found when the upper layer was stiffer than the lower layer. More specifically, the first critical velocity was close to the shear wave speed of the lower layer and the second critical velocity was approximately the Rayleigh wave speed of the upper layer. In addition, the thickness of the lower layer had an impact on the magnitude of the critical velocity effect (Alves Costa et al. [5]).

The majority of the aforementioned works used simplified beam-on-ground models to analyse the ground vibrations under moving train loads. Although these solutions could be used to understand the vibration generation mechanism, these methods are not able to deal with the complex track structures and ground soils. Determining the critical speed of train operation remains difficult due to the complex properties of the track, embankment and ground. Three-dimensional finite element models may be used to account for details of the track structure and ground, however its main disadvantage is very time-consuming (Bian and Hu [21], Zhai et al. [187], Galvín et al. [68]). To overcome the disadvantage of traditional numerical methods for simulating train induced vibrations, Yang and Hung [181] originally proposed a highly efficient 2.5D finite element method for treating vibrations in half-space media induced by moving trains, and the infinity of the ground was dealt with by the use of infinite elements in the wavenumber domain. Later, same method was used to investigate underground train induced ground vibrations (Yang and Hung [182] and Hung and Yang [80]).

Generally, the analytical and semi-analytical methods are more convenient in introducing critical velocity (Alves Costa et al. [5], Auersch [13] and Ni et al. [137]) and a number of works (Krylov [111], Dieterman and Metrikine [44], Mezher et al. [133] and Hu et al. [78]) have shown that the Rayleigh wave speed in the

soil is vital for the assessment of critical velocities. Therefore, for a line load moving on an elastic half-space, two distintive velocity regimes can be defined around the Rayleigh wave speed (Kouroussis et al. [106]):

- **Sub-Rayleigh** - the load moves at a speed less than the Rayleigh wave speed ($v_0 < c_R$)
- **Super-Rayleigh** - the load moves at a speed greater than the Rayleigh wave speed ($v_0 > c_R$)

The typical range of the Rayleigh wave speeds is 250 - 500 m/s (Krylov [113]), however, this value can drop to as low as 40 - 50 m/s when the soil is very soft (Kaynia et al. [100] and Madshus and Kaynia [128]). As Rayleigh waves are dominant during train passage, it is of specific concern to the railway industry, especially when designing the maximum operational speed. Table 2.1 is an overview of the maximum operational speed of high speed rail in service in different countries, ranked by the track length in service (Loubinoux [124]).

Table 2.1 Maximum operational speeds of in-service high speed rail lines by country (Loubinoux [124])

Country	Continent	In operation (km)	Max. speed (km/h)
China	Asia	31000	350
France	Europe	3300	320
Spain	Europe	3240	310
Germany	Europe	3045	300
Japan	Asia	2764	320
Sweden	Europe	1706	205
United Kingdom	Europe	1377	300

2.4 Train-induced vibration models

Experience with high-speed train in recent years has demonstrated unexpected settlement problems at certain sections of railway lines. This has caused railway companies expensive maintenance work and has become a concern in expanding high speed services which provide effective and environment-friendly transportation. A number of projects are proposed in Europe to devise reliable numerical models accounting for train-track interaction and non-linear behaviour of track components with a more cost effective design. In 2002, to improve the sustained performance of railway tracks, SUPERTRACK programme was established and

institutes from France, Spain and Sweden participated the project. It is the first European railway project and it has successfully improved performance of railway ballasted tracks and reduced maintenance costs by understanding the dynamic and long-term behaviour of ballast using large-scale laboratory tests. It marks the beginning of the comprehensive railway research in Europe and paves the way for the projects ahead.

2.4.1 Analytical models

In an attempt to simulate track dynamics, early researchers such as Lamb [117], Kenney [101] and Fryba [65] used analytical expressions to model the problem as a moving point load placed on an elastic half-space. Later, Patil [141] established an analytical approach to investigate the dynamic response of an infinite Euler-Bernoulli beam due to a vibrating point load. The ground was combined with the track model to form a continuous damped elastic Winkler foundation and the results were obtained in the frequency domain. Knothe and Grassie [102] reviewed three types of track model, which consist of one-, two- and three-layer supports that are made up from stiffness and damping. Two types of beams commonly used in the model, Euler-Bernoulli and Timoshenko formulations, were also discussed in the paper. The former accounts only for the bending behaviour while the latter takes into account also shear deformations and rotary inertia of the beam. For a low frequency of excitation, where the propagating wave has a wavelength much greater than the beam-cross-sectional dimensions, both formulations converge to the same solution. However, for a high frequency of excitation, Timoshenko formulation is necessary for an accurate solution (Bogacz et al. [26] and Knothe and Grassie [102]). It is worth mentioning that high frequency excitation is not used in this dissertation, therefore Euler-Bernoulli formulation is chosen in the model for this research work.

The spring foundation is not sufficient to represent the soil because it cannot describe the complex soil mechanics and wave propagation in the ground (Knothe and Grassie [102]). Krylov [110] proposed an analytical model to calculate the train-induced vibration generated by quasi-static moving load. It took into account contribution of each sleeper of the track subjected to the action of all wheel axles, where the track was formulated as Euler-Bernoulli elastic beam. Green's function of an elastic half-space was used to represent the wave propagation in the soil. Furthermore, Krylov [111, 113] investigated the level of ground vibrations when the train speed was very high, especially when the train travelled with a speed greater than the Rayleigh wave speed in the soil. However, the layering of the ground was not considered.

De Barros and Luco [41] computed the dynamic displacements and stresses within a multi-layered viscoelastic half-space produced by a constant moving line load. The effects of layering were included by use of an exact factorization of the displacement and stress fields in terms of generalized transmission and reflection coefficients. Dieterman and Metrikine [44, 45] also used a model of a point harmonic load moving along an elastic layer resting on a half-space or a rigid foundation to study the existence of critical speeds, in which an analytical formulation computed by the Green's function was then proposed to represent the soil support.

A more complex analytical model that considered the coupling between railway structure and the ground was introduced by Sheng et al. [150, 151]. Rather than use either the exact or discretized dynamic stiffness matrix, it was found that improved computational efficiency could be achieved by using the flexibility matrix approach as set out by Thomson [167] and Haskell [75]. Jones et al. [89] continued to investigate the effect of train speeds on the dynamic response of the track/ground system. Later, based on the model of Krylov [111], Degrande and Lombaert [42] computed the free field response to moving loads using the dynamic reciprocity theorem, which showed greater computational efficiency. Takemiya and Bian [162] used the substructuring technique to represent the dynamic interaction of a railway track and ground under a running train. The ground was modelled as a multi-layered half-space and the rails were represented by Euler-Bernoulli beam on discrete sleepers with railpad spring connections. The transfer matrix method was used for the dispersive wave field analysis. A similar approach was taken by Karlstroem and Boström [94] to model the ground as a stratified half-space with linearly viscoelastic layers and the sleepers as an anisotropic Kirchhoff plate. The simulations were validated against the field measurements and achieved good agreement. Most recently, Lai et al. [116] completed an anlytical study on dynamic response of multiple simply supported beam system subjected to moving loads. To validate the analytical method reported in the paper, the dynamic response measurement of a typical double simply supported rail-bridge beam system of high-speed railway in China subjected to a moving load was carried out.

The vehicle model was neglected in the methods mentioned above. A more complex analytical model, including vertical vehicle/track interaction and a multi-body dynamic vehicle model, was then proposed by Cai and Raymond [28]. Subsequently, Zhai et al. [185] added the lateral vehicle/track interactions in the vehicle-track system, in which the vehicle subsystem was modelled as a multi-body system and the track substructure as a discretely supported system of elastic beams. Datoussaid et al. [40] and Mazilu

[130] proposed a framework intended to predict the level of ground vibrations induced by tramways rolling on discontinuities at the wheel-rail interface. The vehicle and track were based on multi-body and finite element approach, and the propagation of vibrations was computed from the Green's function. Most of these models only took into account the vibration generated by moving 'quasi-static' axle loads. In fact, Lai et al. [115] showed that consideration of only quasi-static loads would underestimate the actual response level, especially for higher excitation frequencies. Sheng et al. [152, 153] indicated that it was of great importance to include the dynamic loads when calculating the ground vibration in the far field. This is because the dynamic mechanism of vibration generation is considerably more important than the quasi-static axle loads for environmental vibration study (Sheng et al. [153]). Similar models have been then applied by several authors (Auersch [12], Dimitrovová and Varandas [46], Xia et al. [178]) and Lombaert and Degrande [122] showed how train speeds could affect quasi-static and dynamic contribution.

2.4.2 Semi-analytical models

Expanding upon the analytical methods above to simulate more complex layered soil cases, more sophisticated semi-analytical models have been proposed. A two-dimensional semi-analytical model of ground vibration due to a moving harmonic strip load was developed by Lefeuve-Mesgouez et al. [118]. The model consisted of an elastic, isotropic and homogeneous half-space, with modified hysteretic damping. It showed the existence of Doppler effect in the subsonic case. Hung and Yang [79] adopted a similar approach to study the effect of various vehicle loads. Kaynia et al. [100] proposed a semi-analytical model for the prediction of ground response. An embankment was modelled using an infinite viscoelastic beam and Green's function was used to calculate the ground stiffness matrix, developed by Kausel and Roesset [99]. Good agreement was achieved between simulated results and measurements obtained at the Ledsgard site in Sweden. Further, Lefeuve-Mesgouez et al. [119] improved the previous model and developed a three-dimensional semi-analytical model of ground vibration due to a moving harmonic rectangular load. The equations of motion were solved with the aid of the Fourier transform and dynamic stiffness matrix approach. It allowed to predict more accurately the realistic wave motions. The stiffness matrix approach was also applied in the works of Takemiya [161], Picoux and Le Houedec [142] and Picoux et al. [143]. Note that the solutions were obtained in the frequency domain, so the inverse Fourier transform would lead

to the solution in the time domain. Moreover, Grundmann and Lenz [71] utilized the Wavelet transform combined with the Fast Fourier Transform (FFT) for an efficient inverse technique.

Further, Sheng et al. [152] and Thompson [166] proposed a semi-analytical approach in which the track was modelled analytically in the frequency domain and the soil was modelled using an integral transformation method, which was similar to that developed by Jones and Petyt [90]. This model took two loading modes into account (static and dynamic) and revealed the importance of the dynamic regime in the case of super-Rayleigh for the amplification of vibration (Sheng et al. [152]). It also showed a better efficiency and accuracy in the results. Later on, Liao et al. [120] analysed the steady-state response in an elastic half-space generated by a surface sub-Rayleigh point load. A new numerical technique was proposed to calculate the integral in the wavenumber domain based on the method of steepest descent, which turned out to be very helpful in computing efficiency.

Bian and Chen [18] developed an explicit time domain semi-analytical solution for the dynamic response of a layered ground due to a moving harmonic load. The solution was based on eigenvalue decomposition with respect to the Laplace parameter for the governing equation in the transformed domain. This proposed explicit time domain thin-layer method is a powerful and versatile solution, which is accurate in the horizontal direction and has the same accuracy in the vertical direction as the finite element method (Bian and Chen [18], Bierer and Bode [24]). Steenbergen and Metrikine [158] derived the formulation for the equivalent dynamic stiffness of the half-space, where the coupling between the track and soil is achieved by taking into account the equilibrium of loads and the compatibility of displacements along the track-ground interface. This coupling strategy was also applied by Alves Costa et al. [4] and Alves Costa [1]. The model was found to be in agreement with field data collected at Ledsgard, Sweden.

When the system is considered invariant in the horizontal direction, the dynamic response of the ground can be simulated using a combination of analytical equations, combined with finite elements for the non-invariant direction (i.e., the vertical direction). This approach is known as the Thin-Layer Method (TLM), where the medium is discretised into thin layers in one direction (vertical). These elements are similar to traditional 1D finite elements, however the horizontal directions are solved analytically, thus allowing the solution to be computed in a fraction of the time required for a full 3D model. The TLM was first introduced in 1970s (Lysmer and Waas [127], Waas [173]) and since then it has found use in several areas related to wave propagation in layered media and in soil-structure interaction problems. The development of the

generalised TLM was described by Kausel [96], Kausel and Roesset [99], and Kausel [97, 98]. It has been used for railway problems by Bian and Chen [18], Alves Costa [1], Alves Costa et al. [3] and Bian et al. [20] to predict train induced vibrations.

2.4.3 Numerical models

In comparison to analytical and semi-analytical models, numerical models are more versatile and can be efficiently used to study the effect of train speed or weight, track type, material resiliency, ground conditions, etc. To correctly model vibrations induced by vehicles, it is of importance to understand the generation and propagation mecahnisms, as shown in Figure 2.1. When the vehicle interacts with the track, it induces a moving stress field on it. The stresses are transmitted from the vehicle to the track through contact surfaces (i.e., wheels) that move in space. Due to the dynamic behaviour of the vehicle and its interaction with the track, the vehicle is subjected to accelerations and so the contact stresses, besides moving with the vehicle, also change their value in time. The non-varying component of the contact stresses is known as quasi-static excitation while the component varying with time is termed as dynamic excitation. During the wave propagation process, the stress fields (or the vibrations) propagate through the track and part of them is transmitted into the ground. These stresses continue to propagate in the ground, being reflected or refracted whenever a different material or a barrier is encountered, before eventually reaching the building nearby. The vibrations that reach the building will generate a dynamic response on it and affect the perception of people inside.

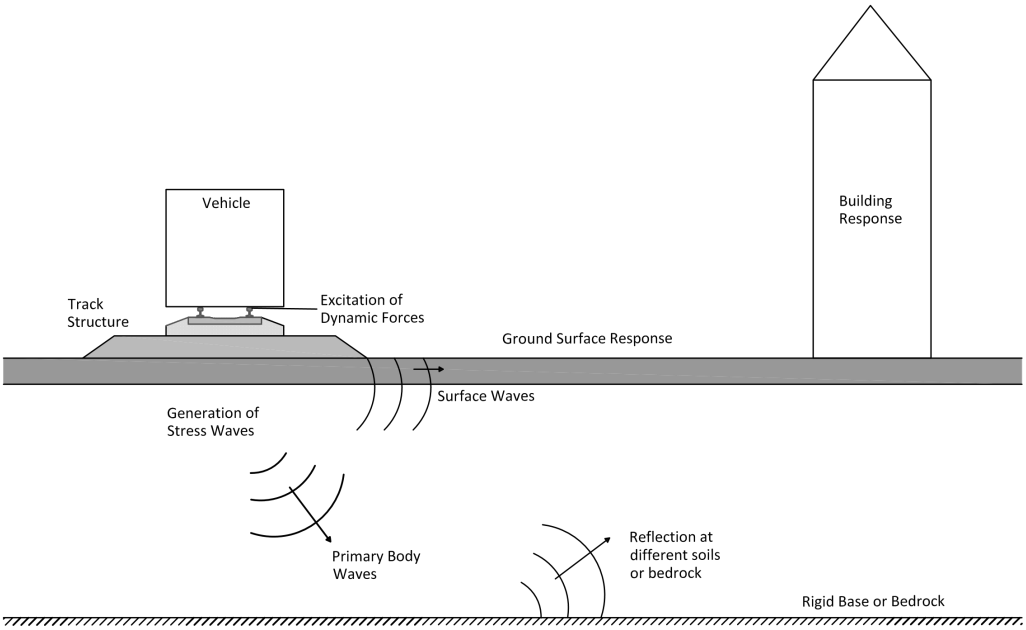

Fig. 2.1 Generation and propagation of the vehicle induced vibrations

2D models

The modelling of vehicle generated vibrations should be three dimensional, i.e., the vehicle moves in one direction while the waves propagate in the ground in all three directions (vertical, horizontal and longditudinal). Therefore, modelling a three dimensional problem can become very complicated and time consuming. For this reason, early works described it with 2D models. Gutowski and Dym [73] mentioned in their review paper that the vibrations generated along a railway track could be modelled as a line source as long as the railway was relatively uniform and the receiver was in the far field, but close enough to the source (less than $1/\pi$ times the length of the train). The authors also supplemented that if the ground motions were dominated by the surface waves, then there would be no geometric damping. Hence the vibrations would attenuate solely due to material damping. In another 2D model, in which a finite element model was used, the efficiency of soil improvement via the lime pile technique as a countermeasure was studied (Taniguchi and Okada [163]). Later, Chua et al. [34] used 2D FE model to predict the vibration levels in a four-storey podium block due to the passage of trains in a double-box tunnel, accounting both for the quasi-static and dynamic excitation. A parametric study was then carried out by Yang and Hung [180] to analyse different types of wave-barriers in reducing ground vibrations induced by a vehicle. A 2D finite/infinite element scheme was adopted to allow for the modification of the geometric and material parameters. Wang and Zeng [174] presented a 2D finite element model to study the effectiveness of rubber-modified asphalt concrete (RMAC) for the vibration attenuation of high-speed railways. A similar approach was then applied to predict

the vibration from the tunnels by Fujii and Takei [66]. Yang et al. [179] developed a 2D dynamic finite element model in ABAQUS to investigate the effects of train speed, acceleration/braking and geometric variation in rail head level. Instead of using a constant axle load, Pakbaz et al. [140] applied a uniform distributed load in the 2D finite element model to simulate the subway induced vibrations in Iran-Ahwaz city. Further, Çelebi and Goktepe [59], Çelebi and Kırtel [60] included non-linearity behaviour in the 2D model under plane-strain condition with elasto-plastic Mohr-Coulomb constitutive law. Moreover, a number of vibration mitigation methods (i.e., wave impeding barriers and thin-walled trench) were also studied by several researchers using 2D finite element models (Saikia and Das [147] and Bose et al. [27]).

3D models

With the improvement of computational performance, both in terms of memory and speed, the use of 3D models became possible. Conventional methods used for the analysis of three dimensional problems, such as the finite element (FE) method and the boundary element (BE) method, have been employed to analyse the problem of induced vibrations (as shown in Figure 2.2). The FE method requires the discretization of the domain, which will lead to a large number of degrees of freedom and sparse symmetric matrices. It is also possible to model irregular domains in the FE model. However, the classical FE model is unable to simulate infinite domains, so particular procedures need to be dealt with at the boundaries of the truncated domains in order to avoid fictitious reflections (Alves Costa et al. [2]). Conversely, the BE method only requires the discretization of the boundary of the domain, thus resulting in less degrees of freedom. Nonetheless, it causes full non-symmetric systems of equations. The BE method considers the radiation of waves towards infinity, but cannot take into account non-linearity so that it needs the knowledge of Green's functions or fundamental solutions (O'Brien and Rizos [138] and Galvín et al. [68]). To combine the merits of BE and FE method, the hybrid FE-BE method is used when the coupling between irregular domains and unbounded domains is needed.

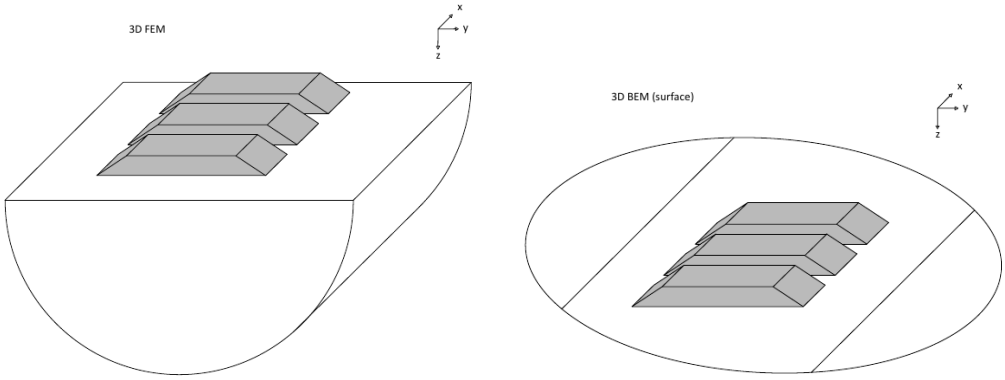

(a) (b)

Fig. 2.2 Schematic illustration of (a) 3D FE model (b) 3D BEM (surface)

Regarding the FE method, Hall [74] developed a 3D finite element track-soil model using ABAQUS, which was subjected to moving point loads. In the model, the reflections at the boundaries were treated using dashpots. The author also compared the results obtained from the 3D model with those computed by a 2D model, it was concluded that the 2D model could be used to study certain effects of vehicle induced vibrations but not to obtain accurate predictions of the levels of vibrations. In another work using the FE approach, Ekevid and Wiberg [57] used a similar approach but instead of treating the boundaries of the mesh as dashpots, the authors utilised the scaled boundary finite element method (Wolf [176]). Despite the proposed apporach being able to account for the radiation of the waves to infinity, the fact of using a 3D mesh demanded a considerably large computational cost. Following these FE methods, Ju and Lin [91] developed a 3D formulation to simulate soil vibrations due to a passing train and to study the efficiency of soil improvement as a countermeasure. The boundaries were treated as first-order absorbing boundaries and the systems of equations were solved by the pre-conditioned conjugate gradient method. Later, Powrie et al. [144] studied the stress change experienced by different soil layers below the track structure. A more completed and integrated train-track-ground dynamic model had been presented on the basis of the vehicle-track coupled dynamics and the finite element method by Zhai et al. [186]. The authors indicated that the influence of the wheel-rail dynamic interaction caused by track irregularities on the ground acceleration was significant.

Further, a number of researchers also proposed 3D FE models in the time domain using ABAQUS (Anastasopoulos et al. [7], Connolly et al. [36, 35], Kouroussis et al. [107] and Varandas et al. [170]). A 3D finite element model was developed using ABAQUS by Bian et al. [22] and 8-node hexahedron reduced

integration solid elements were used in the analysis. It was then used to predict permanent settlement of a railway structure under a cyclic traffic loading. Kouroussis et al. [108] later used sub-modelling, where a multibody vehicle model was considered and combined with a 3D ABAQUS ground model surrounded by infinite elements. Banimahd et al. [15] continued to study the problem of railway stiffness transitions numerically in terms of track deterioration and passenger comfort using 3D FE representation of the railway track interacting with a passing train. El Kacimi et al. [58] developed a Fortran based 3D FE code in the time domain and investigated the effect of fundamental passing frequency of a high-speed train on dynamic track response, under a varying range of velocities. Ekanayake et al. [56] developed a 3D dynamic finite element model using ABAQUS/Explicit programme to numerically simulate the attenuation of ground vibration using open and in-filled wave barriers. ABAQUS/Explicit could perform dynamic analysis using explicit central difference time integration. Recently, Shih et al. [156, 157] capitalised on the 3D FE model developed by ABAQUS to represent a load moving on a railway track on a flexible ground. A systematic study is carried out to compare different sizes and shapes of finite element mesh grid, different boundary conditions intended for suppressing reflections from the truncated model boundaries, and different models of soil damping. Moreover, Feng et al. [62] found out that the use of absorbing boundaries and Rayleigh damping approach could prevent wave reflections from the artificial edges and simulate the material damping, respectively. Besides ABAQUS, 3D FE models in the time domain were also built in other commercial softwares for dynamic vibration analysis, i.e., VAMPIRE (Morales-Ivorra et al. [135]) and PLAXIS (Kalliainen et al. [93]). The majority of the models mentioned above is in the time domain, while frequency domain solutions in FE models also have been proposed by a number of authors. Ju [92] investigated the derailment of trains moving on multi-span simply supported bridges with foundation settlements or rotation using a frequency domain FE model. Feng et al. [61] then developed a 3D FE track-ground model to study vibrations induced by high-speed train. The loads of the train were simplified as a series of point loads and the Fourier transform was applied to solve the track-ground system. Koroma et al. [104] provided a procedure for studying track dynamics that made use of both space-time and wavenumber-frequency techniques, in which the railway track was modelled in the space-time domain using the 3D FE method and the ground was modelled in the wavenumber-frequency domain.

As for the BE and hybrid FE-BE approaches, Bode et al. [25] used the BE method to model the ground and the FE approach for the sleepers and rails. The methodology was formulated in the time domain and

was used to predict the vibrations in the free-field and to investigate the effect of the soil-sleeper coupling scheme. The half-space Green's function was utilised for the soil, thus limiting its discretization to the regions interacting with the sleepers. A similar strategy was followed by O'Brien and Rizos [138], but instead of using half-space Green's function, full-space Green's function was adopted, which required the additional discretization of the free surface of the soil and led to an increase in the number of degrees of freedom. The 3D FE-BE model was then coupled with a multi-body system for the vibration prediction. The work was then extended and the FE method was combined with the BE method in an attempt to include the train-track-soil interaction and to consider the irregularities of the vehicle/track system and the discrete sleeper support (Auersch [12]). Later, Galvín and Dominguez [67] used 3D BE approach for the analysis of soil vibrations induced by high-speed moving loads. In the paper, only the quasi-static component of the train excitation was considered.

A challenge however with full 3D numerical modelling is that it is computationally demanding. In the past decade, approaches that take advantage of the invariance or periodicity of the geometry in the longitudinal direction have been developed to reduce the number of degrees of freedom (Chebli et al. [31] and Chebli et al. [30]). To do so, the track is assumed to be longitudinally split in several cross-section 3D FE slices (as shown in Figure 2.3) and these slices are periodically repeated and have the same model behaviour consideration. Then assembling several repeated slices along the longitudinal direction, the global track model is built and a vehicle model is made to move at a certain speed, making up the complete model. Through this methodology, the model is capable of making simulations of railway tracks with hundreds of meters long that can be quickly solved for each train passage. Arlaud et al. [10], Ferreira and Pita [63] and Arlaud et al. [11] utilised Dynavoie software to use 3D periodic computations to analyse track dynamic properties in detail. In Dynavoie, the track-soil can be divided into thin 3D finite element slices, the periodic modes are computed and the solution is transferred to the space-time domain via the Floquet transform. However, these approaches cannot be used to predict the vibrations inside buildings, while they can still be used to determine the wave fields that reach the buildings.

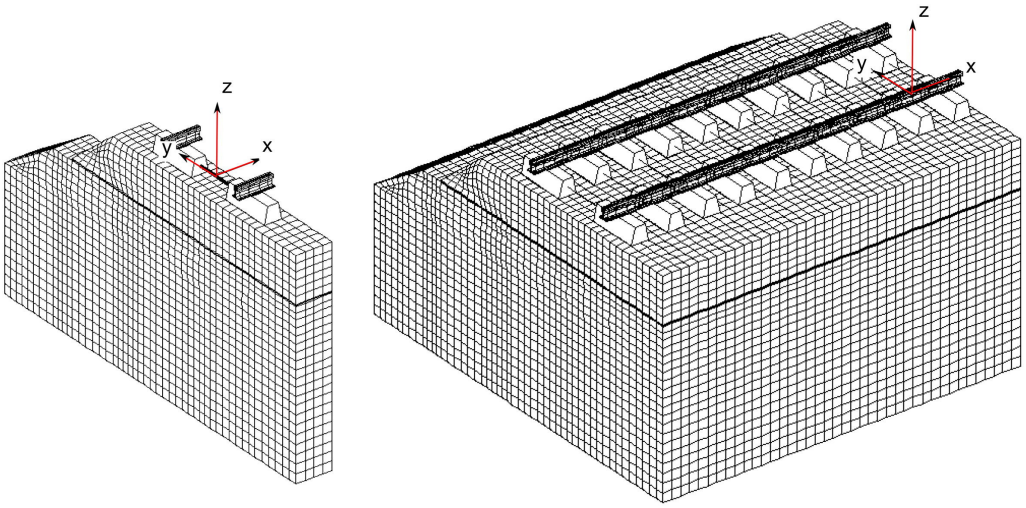

Fig. 2.3 Railway track as a periodic structure, the basic periodict finite element slice is on the left (Arlaud et al. [11])

2.5D models

Alternatively, to further reduce the computational requirements, 2.5D models can be used to approximate 3D problem (as shown in Figure 2.4), and only require a similar number of computations as a 2D problem. Yang et al. [183] approached the problem using finite/infinite elements formulated in the wavenumber-frequency domain (Yang and Hung [181]). This method has the advantage of considering the transverse stiffness of the track and allowing more complex geometries both for track and soil. However, it caused the number of degrees of freedom to increase significantly. The authors used the proposed methodology to study the stiffness, damping and stratification of the underlying ground, and concluded that increasing the stiffness led to the decrease of vibration magnitude, and that the soil stratification was extremely important due to the fact that the cut-off frequencies depend on the layers depths. Later, Alves Costa et al. [3] and Alves Costa [1] used an equivalent linear 2.5D FE-IE model to investigate the effects of soil non-linearity on the dynamic response of high-speed lines. The model was validated against data collected from the well-known Ledsgard site in Sweden. Bian et al. [19] developed an efficient 2.5D finite element numerical modelling approach to simulate wave motions generated in the ground by high-speed train passages. The track structure and supporting ballast layer were simplified as a composite Euler beam resting on the ground, while the ground with complex geometry and physical properties was modelled by 2.5D quadrilateral elements. Bian et al. [23] then upgraded the model to combine a 2.5D FE model with one-quarter car model to study the vibrations caused by vertical track irregularities. It revealed that the track irregularity amplitude had a direct impact on the vertical response for low-speed trains, both for short wavelength and long wavelength irregularities. Track

irregularity with shorter wavelength could generate stronger track vibration for both low- and high-speed cases. Besides FE models, hybrid FE-BE methods formulated in the 2.5D domain have also been used. François et al. [64] and Galvín et al. [68] presented efficient approaches for coupling both 2.5D FE and 2.5D BE models, where the irregular domain was modelled using 2.5D finite elements and the ground modelled using 2.5D boundary elements. Alves Costa et al. [2] also proposed a numerical scheme, based on the coupling between 2.5D FE-BE, to obtain the track-ground response. The results were found to agree well with field data from a test site in Portugal. These hybrid approaches have proven to be more efficient and more versatile than the predictions that simply rely on one of these methods.

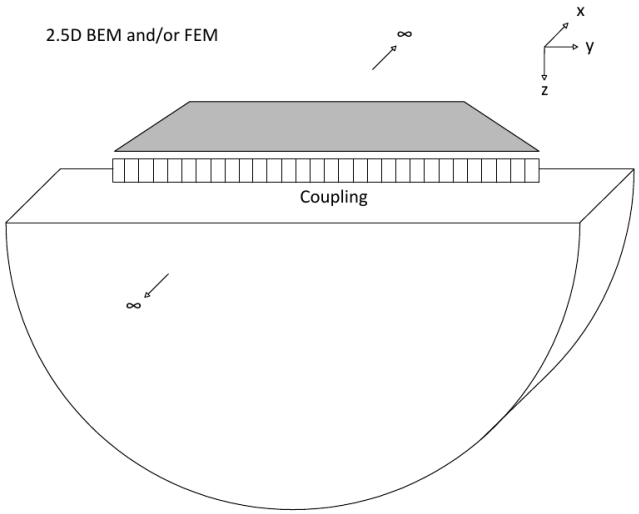

Fig. 2.4 Schematic illustration of 2.5D BEM and/or FEM

Also regarding tunnels, Gupta and Degrande [72] and Galvín et al. [68] adopted a periodic FE-BE methodology and used it extensively in the numerical prediction of vibrations induced by railway traffic in tunnels. Rieckh et al. [146] developed an invariant model in which the anisotropy of the soil was considered. The model was built on the basis of a boundary element formulation, and it used the 2.5D fundamental solutions of layered and anisotropic media to enhance the stability and efficiency of the numerical calculations.

To complete the discussion on prediction models, one must add that in recent years new approaches using meshless methods (or mesh-free methods) were proposed and have shown to be an alternative to the boudanry element and finite element methods. The name meshless is given because these methods do not require the discretization neither in the interior or the boundary of the domain of interest. A typical approach is named *Method of Fundamental Solutions* (MFS), which resembles the BE method in the sense that it

requires the availability of the fundamental solutions, but overcomes the need for evaluating the boundary integral, thus avoiding complications associated with the singularities of the fundamental solutions (Godinho et al. [69], Godinho and Soares Jr [70] and Mendes et al. [132]).

2.5 Soil non-linearity

According to laboratory tests, soil stiffness is related to a number of parameters such as cyclic strain amplitude, void ratio, mean principal effective stress, plasticity index (PI), over-consolidation ratio, and the number of loading cycles (Kramer [109]). The most important parameter for modelling non-linear soil behaviour, especially when shear strains are larger than 10^{-5} to 10^{-4}, is the shear modulus (Zhang et al. [189]). It was found that the shear modulus decreases with increasing shear strain above this level. This phenomenon is often referred to as *shear modulus degradation* (or *stiffness degradation*). Further, Zhang et al. [189] indicated that the key factors for shear modulus degradation are the shear strain, mean effective confining stress, soil type and plasticity index, whereas other factors including the loading frequency, number of loading cycles, over-consolidation ratio, void ratio, degree of saturation, and grain characteristics are less important. Moreover, damping ratio is found to rise along with shear strain, which will also play a key role in soil non-linearity behaviour (Zhang et al. [189]).

When the soil is subject to small strains, the stresses and strains are directly proportional, meaning the soil response can be considered linear and elastic. Linear-elastic models are normally used for studying ground vibration due to railway traffic. However, it has been observed that the large strains would occur when the train speed approaches the critical velocity (Krylov [111], Madshus and Kaynia [128] and Kaynia et al. [100]). Under this circumstance, non-linear soil behaviour occurs and it causes soil stiffness to decrease. Therefore, the linear-elastic model cannot be used to simulate such dynamic responses.

2.5.1 Experimental approach

The non-linearity of the shear stiffness and damping ratio with increasing shear strain can be seen from measurement data of shear stress behaviour under a cyclic loading, as shown in Figure 2.5 and Figure 2.6. To be more specific, Figure 2.5 shows the hysteresis loop to represent the strain-stress relation from cyclic loading. From left to right, the hysteresis loops at 7 different stages are drawn. Shear modulus and damping

ratio are then plotted against the strain level in Figure 2.6. It can be seen that the shear modulus of soil decreases with the increasing strain level whereas the damping ratio would rise as the strain becomes larger.

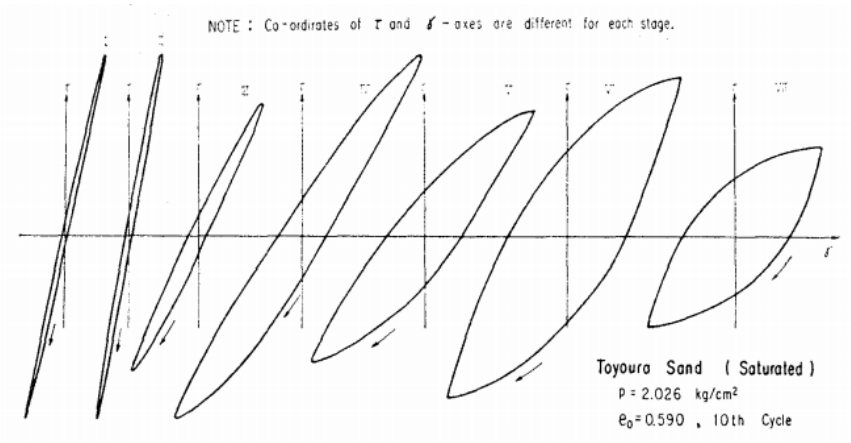

Fig. 2.5 Strain-stress records of different stages under a cyclic loading (Iwasaki et al. [88])

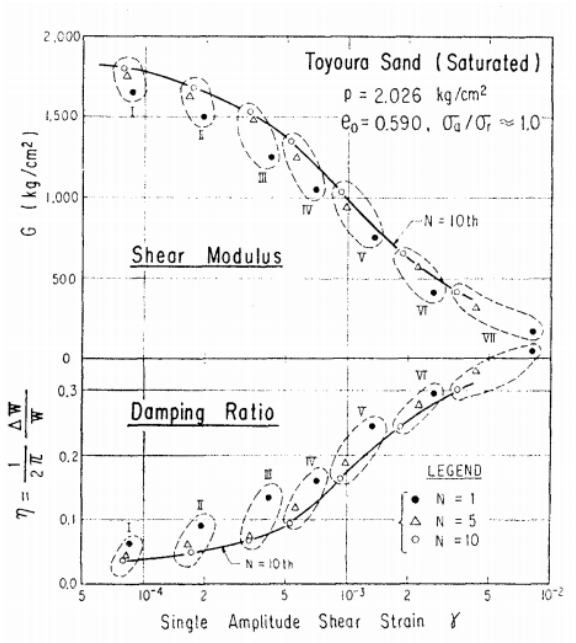

Fig. 2.6 Shear modulus and damping ratio against shear strain (Iwasaki et al. [88])

Normally, the shear modulus degradation curve can be derived from stress-strain behaviour by normalizing the shear modulus (i.e., dividing the shear modulus G by its maximum value G_{max}), where G_{max} is the shear modulus at very low strain levels ($< 10^{-6}$), which can be obtained from laboratory results (Kramer [109]).

The shear modulus and damping ratio are also found to be significantly influenced by the confining stress, especially for soils of low plasticity (Santos and Correia [148]). The higher the confining stress, the stiffer the curves would appear. In contrary, as the confining stress increases, the shear modulus increases

and the damping ratio decreases. Vucetic and Dobry [172] found out that the plasticity index (PI) would have a significant effect on the cyclic stress-strain parameters of saturated soils. Moreover, soils with higher plasticity tend to have a more linear cyclic stress-strain response at smaller strains and degrade less at larger shear strain. On the other hand, soils with higher plasticity index have smaller damping ratio at higher shear strain than those with lower plasticity index. Additionally, Lin and Huang [121] indicated that the frequency of cyclic loading did not affect the shear modulus, however it would have a noticeable influence on the damping ratio.

2.5.2 Numerical approach

To include non-linear material effects, Madshus and Kaynia [128], Kaynia et al. [100], Sheng et al. [152] and Hall [74] used models with manually adjusted soil stiffness to predict the response of track in Ledsgard, Sweden. Furthermore, Thach et al. [164] used a similar approach to investigate the response of a piled embankment. A challenge with this approach is that manually choosing stiffness' values is often inaccurate and it is only practical to implement stiffness changes over large depths of soil (e.g. across an entire soil layer). Alternatively, Banimahd et al. [15] considered non-linear elastic behaviour when modelling the response of the same Swedish site using a time domain 3D finite element model. This allowed for the non-linearity of all finite elements to be considered individually, however, a challenge with constitutive models though is that they require a large number of input parameters, many of which are difficult to quantify. Therefore, Alves Costa et al. [3] proposed a 2.5D finite/infinite element method, coupled with an iterative, 'linear equivalent' procedure that used strain levels and degradation curve data to automatically adjust material stiffness and damping based upon strain levels. This 'element-by-element' non-linear approach was used to validate against the Ledsgard site data and strong agreement was achieved. Cunha and Correia [39] and Correia and Cunha [37] implemented the nonlinear simulation using a cyclic nonlinear model that simulates the hysteretic behaviour according to the Masing rules. The authors then presented the simulation of rail track response using a 3D FE model considering nonlinear subgrade properties.

To compare the difference between a constitutive non-linear material model and a linear equivalent model, Shih et al. [157] compared both using a 3D finite element approach. To reduce the complexity of the linear equivalent formulation, a horizontal 'layer-by-layer' 'linear equivalent' approach was used. This assumed that the same non-linear changes to material properties below the track centre-line also propagated to the

far-field. Therefore the elastic material properties away from the track were considered to degrade in an overly conservative manner. Despite this assumption, for locations near the track, it was found that the linear equivalent approach gave similar results but with reduced computational requirements. Dong et al. [52, 51] built upon the linear equivalent approach to simulate soil non-linearity using thin-layer method (TLM). The track-ground models were coupled and the overall model was computed in an iterative (thin) 'layer-by-layer' manner to include the effects of non-linearity. This greatly reduces the computational time, and due to the very thin nature of elements used in the thin-layer method, stiffness changes due to non-linearity can be simulated with much finer granularity compared to Shih et al. [157].

In order to iteratively update the strains and soil stiffness, the value used for the calculation of the effective shear strain in this process is chosen as a certain proportion of the maximum effective shear strain. It is important to determine this factor appropriately if accurate results are to be obtained from the equivalent linear model (Yoshida et al. [184]). Different values for this factor have been found empirically. For instance, 0.65 was recommended and used for seismic analysis (Kramer [109] and Alves Costa et al. [3]). However, overestimation of the amplitude has been seen when the value of 0.65 was used in situations where particularly large strains occur (Yoshida et al. [184] and Shih et al. [157]). Therefore, careful consideration of the value of this factor might be required for different conditions.

2.6 Ballast/Subballast non-linearity

In recent years, faster and heavier trains have been introduced owing to a growing demand from commuters and industry. This has resulted in an increase in track degradation, lateral instability, and therefore the frequency and cost of maintenance. This problem becomes more severe under conditions of railroad ballast fouling (Indraratna and Nimbalkar [85]). Particles of ballast/subballast become degraded in railroad tracks under heavy cyclic loading, thereby increasing the overall compressibility (Lu and McDowell [125] and Indraratna et al. [86]). The resilient behaviour of track geomaterials (mainly ballast or subballast) is usually assumed to be linear elastic and elastic modelling can be used to estimate the behaviour of materials within a small strain level, but it is incapable of predicting the material behaviour for stresses that exceed the limit. Consequently, the use of linear elastic geomaterials might not be appropriate and can lead to inaccurate and misleading results. This results in the introduction and inclusion of non-linearity to the track materials.

In this section, non-linearity of ballast/subballast is reviewed in terms of both experimental and numerical strategies.

2.6.1 Experimental approach

Granular materials play an essential role in the overall deformation behaviour of ballast/subballast. Monotonic and cyclic material testing are two common test procedures for understanding the material characteristics of ballast. Figure 2.7 shows the test setup used in the trixial tests and it includes a closed-loop sevo-hydraulic loading system.

Typically, monotonic tests are applied to investigate the stress-strain behaviour, strength and degradation, which are the foundations for the studies of granular material non-linearity. A large-scale triaxial test was proposed by Indraratna et al. [82] to study the mechanical behaviour of railway ballast. Repeated load triaxial test, with variable or constant confining pressure, have also been used for more than one decade to evaluate the mechanical properties of unbound granular materials (Correia et al. [38]). Later, a series of high frequency cyclic triaxial tests were conducted by Indraratna et al. [84] and Lackenby et al. [114] to examine the effects of confining pressure and deviatoric stress magnitude on ballast deformation (permanent and resilient) and degradation. Experimental results indicated that for each deviatoric stress considered, an optimum range of confining pressures existed such that degradation was minimised. This range was found to vary from 15 – 65 kPa for a maximum deviatoric stress of 230 kPa, to 50 – 140 kPa when deviatoric stresses increased to 750 kPa. Indraratna et al. [86] presented the results of the influence of frequency on the permanent deformation and degradation behaviour of ballast during cyclic loading. The non-linear behaviour of ballast under numerous cycles was investigated through a series of large-scale cyclic triaxial tests. The results showed that permanent deformation and degradation of ballast increased with the frequency of loading and number of cycles. The behaviour of railroad ballast under monotonic and cyclic loading could be found in the work of Anderson and Fair [9].

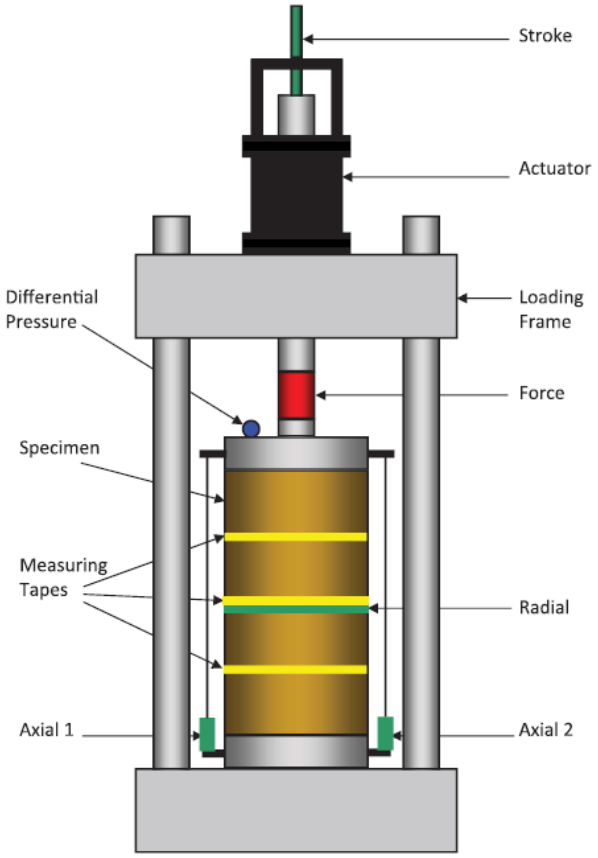

Fig. 2.7 Triaxial test setup for ballast material (Dyvik and Kaynia [54])

Despite that the mechanical properties of ballast can be obtained by monotonic and cyclic triaxial tests, measurements taken in railway sites are more desirable and accurate. Nonetheless, it is of great difficulty to control the test parameters and to collect the data. Therefore, different laboratory facilities have been used to mimic the conditions in a real track. A major new full-scale laboratory test facility for railway trackbeds was designed and developed by the research team at the University of Nottingham (Thom et al. [165]), as shown in Figure 2.8 and Figure 2.9. The facility allowed application of cyclic loads of up to 94 kN directly to the sleepers using a loading system constructed in a laboratory test pit. Three sleepers are involved, and loads are applied by servo-controlled hydraulic actuators (as displayed in Figure 2.9) with the inputs phased to simulate a moving wheel.

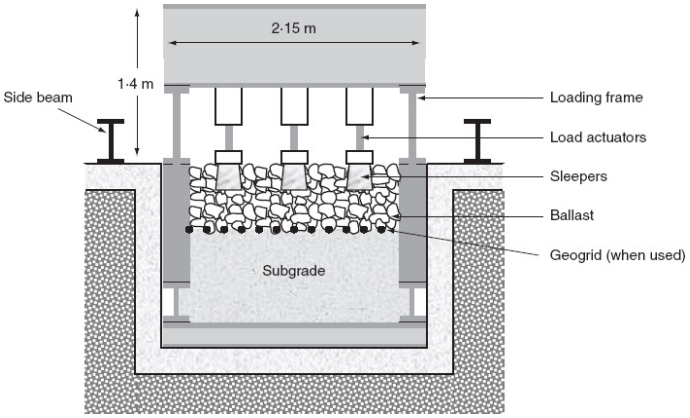

Fig. 2.8 Cross-section of the facility (Thom et al. [165])

Fig. 2.9 Servo-controlled hydraulic actuators (Thom et al. [165])

Aursudkij et al. [14] developed a large-scale triaxial test apparatus, as displayed in Figure 2.10, for railway ballast testing that comprised a double-cell arrangement for measuring volume change by differential pressure. In the triaxial test, a pressure of 200 - 250 kPa was applied as cyclic loading corresponding to the maximum contact pressure at the sleeper base and a 30 kPa confining pressure was applied.

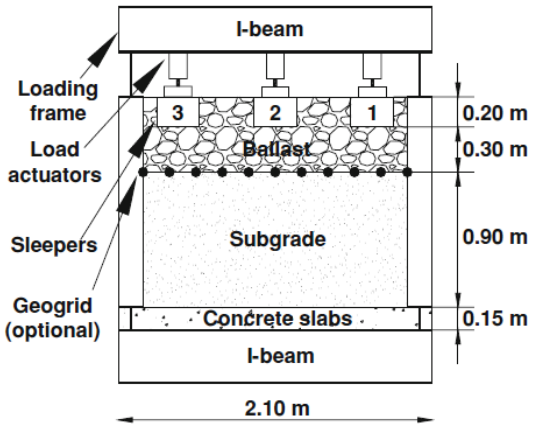

Fig. 2.10 End-view diagram of the testing facility designed by Aursudkij et al. [14]

2.6.2 Numerical approach

Ballast/subballast cannot resist a tensile stress as it is granular material. The stiffness is usually low because of the weakness of bonding. Despite that most of the deformation of ballast is recoverable, permanent strain could occur during the cyclic loading. The resilient modulus normally rises with the increasing number of applied load cycles and eventually reaches an approximately constant value after a certain number of repeated loads.

Nguyen et al. [136] proposed a no-tension constitutive law for modelling granular materials. Significant differences occurred in the results from linear and non-linear elastic models. Nonetheless, confining stress was not taken into account in the model, in spite of being an important parameter in modelling the ballast mechanical responses (Indraratna et al. [84], Lackenby et al. [114], Aursudkij et al. [14]).

The most commonly used model to describe the non-linear resilient nature of unbounded granular material is the $K-\theta$ model, proposed by Hicks and Monismith [77]. The resilient modulus can be derived as:

$$E = K_1(\frac{\theta}{\theta_0})^{K_2} \tag{2.5}$$

Where θ is the sum of the effective principal stresses and θ_0 is a reference value, which is normally set as 100 kPa. K_1 and K_2 are constants to be determined from experimental results. Further, a 3D FE model of railway track taking into account the ballast non-linearity was developed by Varandas [171]. Dynamic results from two different load speeds were compared with the results from a linear model. It revealed that

the dynamic responses were approximately similar from linear and non-linear models when the speed was 22% of the critical velocity, however, difference was found when the speed was raised to 75% of the critical velocity.

The resilient modulus does not rely solely on the effective principal stresses, it is also determined by the shear strain induced by the deviatoric stress. Therefore, a modified $K-\theta$ model was used by Uzan [169], as shown in Equation 2.6.

$$E = K_1(\frac{\theta}{\theta_0})^{K_2}(\frac{q}{\theta_0})^{K_3} \tag{2.6}$$

Where $q = \sigma_1^{'} - \sigma_3^{'}$ represents the deviatoric stress ($\sigma_1^{'}$ and $\sigma_3^{'}$ are the principal stresses). This method was capable of capturing better variations of the resilient modulus and was adopted to assess the critical speed by Woodward et al. [177].

Models that consider the factors such as initial state, volume behaviour, drainage conditions, stress-strain behaviour and possible rotation of principal stress axes are normally referred to as advanced constitutive models. An elastoplastic constitutive model for coarse granular aggregate ballast incorporating particle breakage was proposed by Indraratna et al. [82] and Indraratna et al. [84], which took into consideration the degradation of particles due to shearing. The model was based on the ratio between the deviatoric and mean stresses as a function of dilatancy, strength and particle breakage. Due to the fact that the resilience is related to the number of load cycles, a cyclic densification model was then proposed by Indraratna et al. [83]. It was able to capture the realistic deformation and degradation of ballast at various frequencies and confining pressures for a large number of cycles.

Additionally, more advanced technique such as discrete element method (DEM) has also been used to represent the ballast mechanical properties by a number of researchers (Cheng et al. [33], Lu and McDowell [125] and Lu and McDowell [126]). It is based on the normal and transverse contact forces between a collection of rigid particles in an explicit scheme. The main advantage of this approach is that the micromechanics of the ballast layer are well represented. Hence this method becomes more suitable for studying granular thin layers and the localized rigid structures during cyclic loading. The commonly used material constitutive law (Nguyen et al. [136] and Indraratna et al. [84]) is not required in the model. However, the significant drawback of using DEM is that the computational cost is high.

2.7 Conclusion

In order to understand the vibration generation mechanisms and predict the railway vibration, a wide variety of vehicle modelling methodologies have been proposed in the past four decades. A comprehensive review of these modelling techniques and methodologies is provided in this chapter. It covers the analytical and numerical approaches in both time and frequency domains. Additionally, it reviews the importance of material non-linearity in the prediction of dynamic vehicle response and the uses of both experimental and numerical methods in modelling the material non-linearity. These works have laid the foundation for the research conducted in this thesis.

Chapter 3

Fully linear track and subgrade behaviour

3.1 Introduction

Railway tracks experience elevated rail deflections when the supporting soil is soft and/or the train speed is greater than approximately 50% of the wave propagation velocity in the track-soil system (i.e. the critical velocity). Such vibrations are undesirable, so remediation on the natural soil (or alternatively mini-piles or lime-cement treatment) is often used to increase track-ground stiffness prior to line construction. Although areas of existing soft subgrade might be easily identified on a potential new rail route, it is challenging to determine the type and depth of ground remediation required because soils are typically multi-layered and the dynamic behaviour of the track-soil system depends on multiple variables such as train speed. Therefore, on a new line there are 2 challenging scenarios which may be encountered after a critical velocity scoping study:

1. A low stiffness soil configuration which will likely require remediation (e.g. train speed > 70% of critical velocity)

2. A semi low stiffness soil configuration for which the need for remediation is unclear (e.g. train speed between 50-70% of critical velocity)

For both of these cases it is desirable to know how ground remediation will affect the track behaviour. Two types of remediation often used on new lines are soil replacement and soil improvement (Steenbergen et al. [159]), and they are potentially expensive. Therefore, major cost savings can be made by optimising ground replacement/improvement strategies before construction.

This chapter presents a numerical railway model, designed for the dynamic analysis of track-ground vibrations induced by high speed rail lines. The model simulates the ground using a linear thin-layer finite element formulation (TLM) capable of calculating 3D stresses and strains within the soil during train vehicle passage. The railroad track is modelled using a multi-layered formulation which permits wave propagation in the longitudinal direction, and is coupled with the soil model in the frequency-wavenumber domain. The model is validated using a combination of experimental railway field data, published numerical data and a commercial finite element package. It is shown to predict track and ground behaviour accurately for a range of train speeds with much less computational cost than other numerical models.

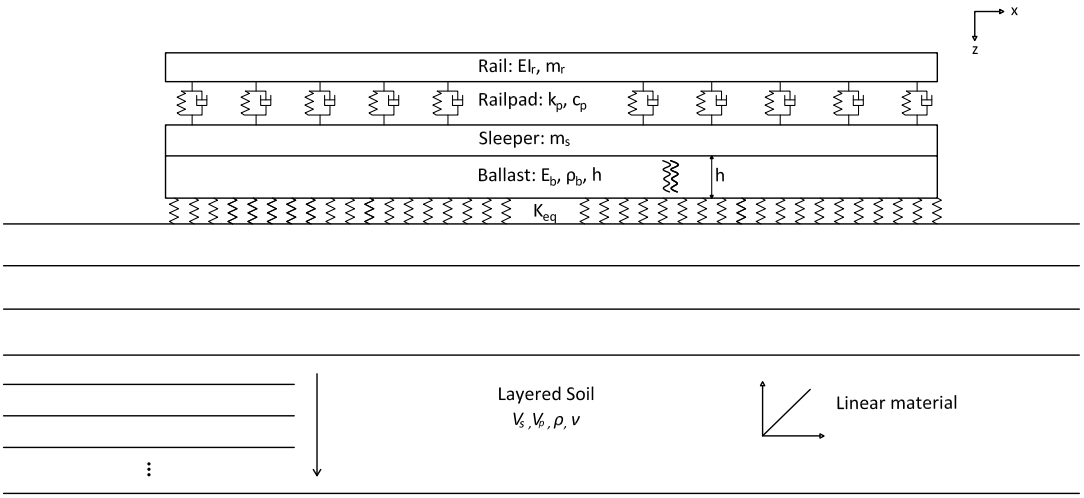

Fig. 3.1 Schematic illustration of the analytical track model coupled with linear TLM ground model

This chapter is organised in five sections. An analytical track model and linear TLM soil model are described in Section 3.2. The schematic diagram for the model is shown in Figure 3.1. The proposed model is then validated against numerical results from Madshus and Kaynia [128] in Section 3.3. Three soil-embankment examples are used to compare the effect of different combinations of stiffness improvement on track behaviour and results are discussed in Section 3.4. Section 3.5 presents discussion over the replacement strategies used. In the end, a short conclusion for the chapter is given in Section 3.6.

3.2 Model description

The model is based on a semi-analytical approach to compute vertical track displacements and three dimensional soil stresses/strains. It comprises of two main components: 1) an analytical track model, and 2) a semi-analytical thin-layer method ground model. Both sub-models are solved in the frequency domain and coupling is performed in the wavenumber-frequency domain, using relaxed boundary conditions between the track and soil. This means that only the vertical components are used for coupling because the 1D track model and 3D soil model have different numbers of degrees of freedom (Kaynia et al. [100], Herraiz et al. [76]). The advantage of this approach is that the deep-wave propagation generated near critical velocity can be simulated both accurately and efficiently.

3.2.1 Track model

The track model is modelled in the wavenumber-frequency domain as previously described in the works of Alves Costa [1], Alves Costa et al. [5], Mezher et al. [133], Dong et al. [53]. It reveals that the proposed model is continuous and it indicates that the discrete elements (such as sleepers and railpads) are modelled through an equivalent continuous formulation. This simplification has a huge advantage in terms of mathematical formulation because the model becomes invariant in the direction of rail road. The validity of equivalent continuous models has been discussed by several researchers who have come to the conclusion that for excitation frequencies below 600Hz there is no significant difference between the responses generated by discrete models and continuous models (Knothe and Wu [103], Takemiya and Bian [162], Knothe and Grassie [102], Sheng et al. [154]). It also should be clarified that the effect of parametric excitation induced by the periodicity of sleepers cannot be met in equivalent continuous model, due to the fact that it arises owing to the displacement discrepancies at the wheel-rail interaction points Alves Costa [1].

The modelling of rail can be normally done through Timoshenko beam or Bernoulli-Euler beam. Moerover, several researchers have found out that the differences in the results obtained by two beam fomulations are minimal in the frequency range up to 500Hz (Mann [129], Alves Costa [1]). In this work, the Bernoulli-Euler beam is chosen to model the rail because of its formulation simplicity.

Different formulations are used to describe the ballasted and concrete slab tracks, respectively, both of which assume the track to be infinite in the direction of train passage. Figure 3.2 illustrates the ballasted

track model. It is composed of rail, railpad, sleeper and ballast components, with the properties of discrete elements (e.g. sleepers and railpads) distributed along its length.

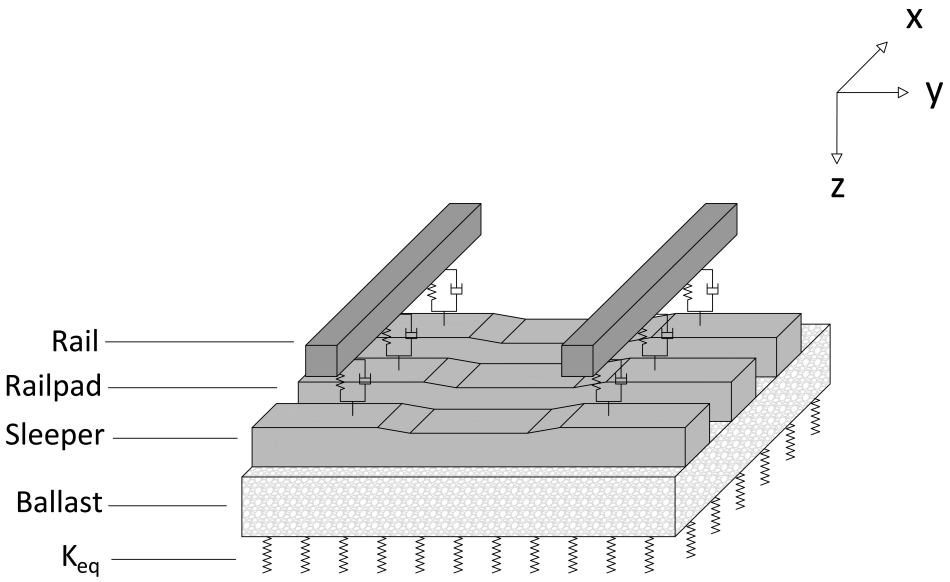

Fig. 3.2 Ballasted track model structure

Equation 3.1 describes the global formulation which permits 1D wave propagation, where: k_x is the Fourier images of coordinate x; m_r and m_s are the mass of rail per metre and the equivalent distributed mass of the sleepers respectively; k_p^* is the complex stiffness of the railpad, which is used to represent the connection between rail and sleeper, i.e., including damping ($k_p^* = k_p(1 + i\omega c_p)$), where * indicates a complex number and k_p and c_p are stiffness and damping of the railpad, of which values correspond to each individual railpad divided by its longitudinal spacing. Regarding the formulation of the ballast, it is assumed that the granular layers (i.e. ballast or sub-ballst layers) can be simulated through a single element with equivalent properties. In this work, it is achieved by using elements obtained through the equation of unidirectional wave propagation (i.e. vertical direction). Hence the simulation of wave propagation on the lateral and longitudinal directions are not taken into account, which is also agreed by Sheng et al. [150], Lombaert and Degrande [122]. The proposed model for the formulation of the granular layer is defined by the following parameters: C_p is the ballast compressional wave speed; E_b is the ballasts Young's modulus; h_b is the ballast thickness; $2b$ is the track width; $\tilde{u_r}$, $\tilde{u_s}$ and $\tilde{u_{bb}}$ are the rail, sleeper, and ballast (bottom) displacements respectively ($\sim$ represents frequency domain response); P is the vertical force acting on the rail.

$$\begin{bmatrix} EI_r k_x^4 + k_p^* - \omega^2 m_r & -k_p^* & 0 \\ -k_p^* & k_p^* + \frac{2\omega E_b^* b\alpha}{\tan(\frac{\omega h_b}{C_p})C_p} - \omega^2 m_s & \frac{2\omega E_b^* b\alpha}{\sin(\frac{\omega h_b}{C_p})C_p} \\ 0 & \frac{2\omega E_b^* b\alpha}{\sin(\frac{\omega h_b}{C_p})C_p} & \frac{2\omega E_b^* b\alpha}{\tan(\frac{\omega h_b}{C_p})C_p} + k_{eq} \end{bmatrix} \begin{pmatrix} \tilde{u_r}(k_x,\omega) \\ \tilde{u_s}(k_x,\omega) \\ \tilde{u_{bb}}(k_x,\omega) \end{pmatrix} = \begin{pmatrix} \tilde{P}(k_x,\omega) \\ 0 \\ 0 \end{pmatrix} \tag{3.1}$$

Moreover, the parameter α is introduced in Equation 3.1 because not all the ballast mass particiate in the dynamic balance of the system. A number of experimental studies carried out by Zhai et al. [188], Zhang et al. [190], Lombaert et al. [123] show that only a fraction of the ballast granulars contributes to the balance of the system. Therefore, the value of 0.5 for the parameter α is chosen according to Alves Costa [1].

The formulation of slab track system is slightly different because the characteristics of the slab are different than the ballast. Figure 3.3 illustrates the layout of the slab track model, and it shows the concrete slab rests directly on the foundation (i.e. k_{eq}). The rails are simulated as a Bernoulli-Euler beam connected to spring-damper assemblies. Unlike the ballasted track, the slab is formulated as the Bernoulli-Euler beam. Therefore, the governing equations for the global slab track are shown in Equation 3.2, where: EI_{sl} is the bending stiffness of the slab; m_{sl} is the mass of the slab per metre and $\tilde{u_{sl}}$ is the vertical slab displacement in the frequency domain.

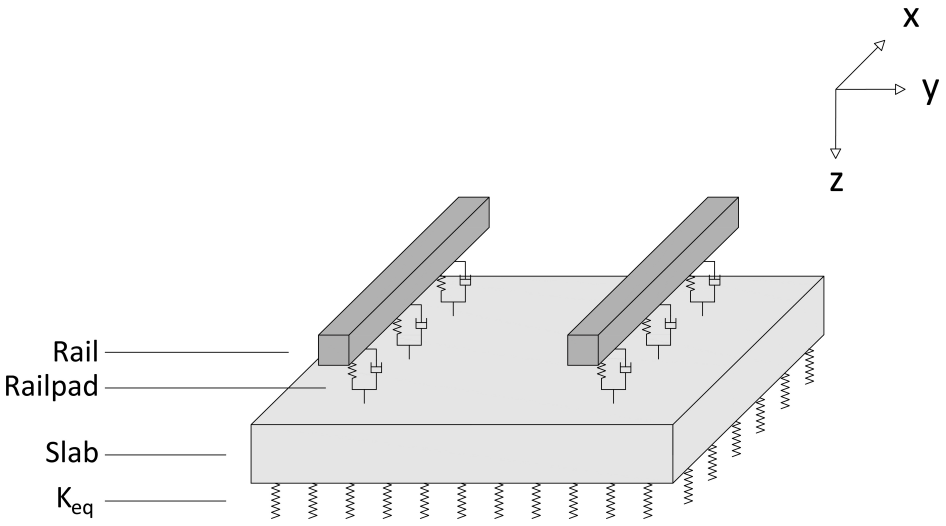

Fig. 3.3 Slab track model structure

$$\begin{bmatrix} EI_r k_x^4 + k_p^* - \omega^2 m_r & -k_p^* \\ -k_p^* & EI_{sl} k_x^4 + k_p^* - \omega^2 m_{sl} + k_{eq} \end{bmatrix} \begin{pmatrix} \tilde{u_r}(k_x,\omega) \\ \tilde{u_{sl}}(k_x,\omega) \end{pmatrix} = \begin{pmatrix} \tilde{P}(k_x,\omega) \\ 0 \end{pmatrix} \tag{3.2}$$

For both track types, track-soil coupling is achieved using a complex equivalent stiffness (k_{eq}) in the vertical direction only, defined in the wavenumber-frequency domain, as shown in Equation 3.3. Higher train speeds typically result in greater wave propagation across the track-soil interface, meaning the deeper soil layers affect the track response. Therefore, the accuracy of coupling across this interface is vital for reliable simulation, especially as the train speed approaches the critical velocity. In this equation, $\tilde{u}^G_{zz}$ is the Green's function of vertical displacement of the uppermost soil surface (z=0) and corresponds to the z-direction term (Q_{33}) of the dynamic flexibility matrix $[Q]$ in the transformed domain (Alves Costa [1]). A thorough derivation of the dynamic flexibility matrix $[Q]$ is given in Appendix A. While k_x and k_y are the Fourier images of coordinates x and y, representing longitudinal and lateral directions, respectively. For both tracks, coupling is achieved by taking into account the equilibrium of loads and the compatibility of displacements along the track-ground interface (Steenbergen and Metrikine [158]):

$$\tilde{k}_{eq}(k_x,\omega) = \frac{2\pi}{\int_{-\infty}^{+\infty} \tilde{u}^G_{zz}(k_x,k_y,z=0,\omega)C_{tg}dk_y} \tag{3.3}$$

Where C_{tg} is a scaling factor used to adjust the track-ground coupling depending upon whether the track is slab or ballasted. In the case of a ballasted track, coupling is achieved through compatibility of displacements at the track centre point on the track-ground boundary (Equation 3.4), as demonstrated in Figure 3.4:

$$C_{tg} = \frac{\sin(k_y b)}{k_y b} \tag{3.4}$$

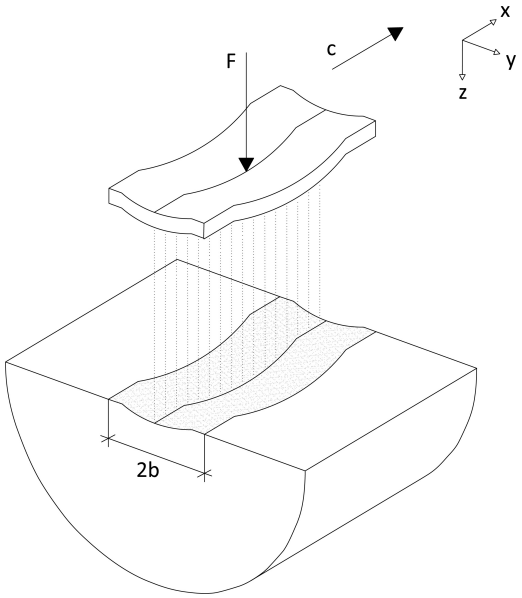

Fig. 3.4 Illustration of scaling factor of the track-ground coupling for ballasted track

Whereas for the slab track, coupling is achieved through compatibility of the average displacements across the track-ground boundary (Equation 3.5), via the approach outlined in Figure 3.5:

$$C_{tg} = \frac{\sin(k_y b)^2}{(k_y b)^2} \tag{3.5}$$

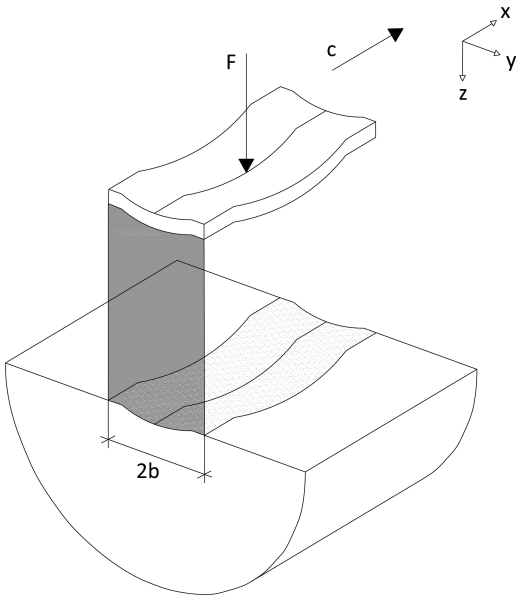

Fig. 3.5 Illustration of scaling factor of the track-ground coupling for slab track

The detailed explanation and derivation of the equivalent stiffness k_{eq} for the ballasted and slab tracks are given in Appendix B. For both track cases, relaxed boundary conditions are assumed, i.e., the compatibility

and equilibrium conditions are only respected in the vertical direction. This is considered valid because vertical excitation is dominant during train passage.

3.2.2 Soil model

Thin-layer method formulation

The thin-layer method (TLM) is a semi-analytical approach commonly used to solve wave propagation problems in 3D unbounded domains (e.g. soils). It relies on discretizing the vertical plane into a finite number of layers, each being thin with respect to the wavelength, meaning vertical displacements can be assumed to vary linearly across each layer. Regarding the horizontal directions, the analytical wave equation is used to rapidly calculate harmonic displacements without suffering from the element aspect-ratio restriction of the finite element method.

The thin layer formulation is undertaken in the frequency-wavenumber domain, with the response computed for each individual frequency under steady-state harmonic conditions. It allows the soil to be discretized along the z-direction with the infinite and homogeneous property along the horizontal plane, as shown in Figure 3.6, in which n represents the total number of vertically discretised soil layers. To ensure the propagation of stresses/strains inside the soil domain is modelled correctly, three-node quadratic thin-layer elements are used (Figure 3.7). Also, to ensure the thickness of each layer is small with respect to the wavelength, all thin layers meet the criteria outlined in Equation 3.6, where k_{max} is the maximum wavenumber under consideration.

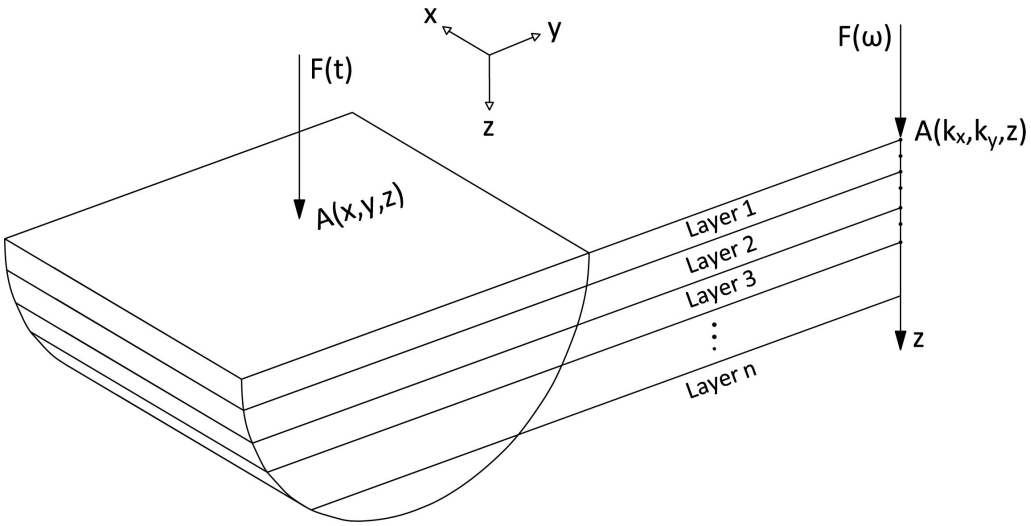

Fig. 3.6 Schematic drawing of the procedure of the vertical discretization and domain transform in the thin-layer method

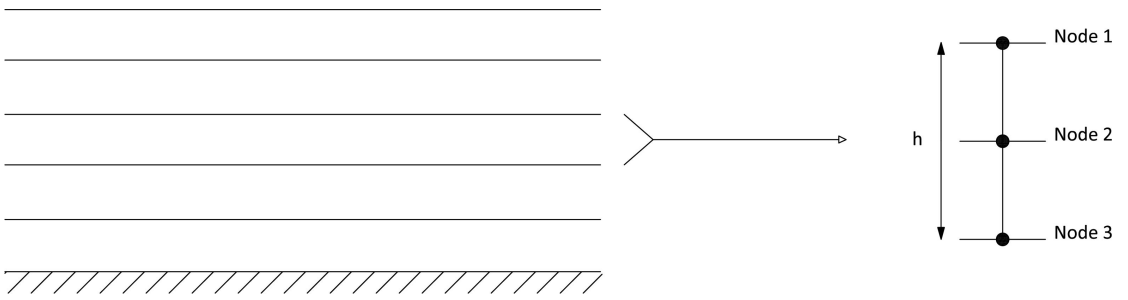

Fig. 3.7 Discretization into thin layers with quadratic interpolation

$$h = \frac{wavelength}{8} = \frac{2\pi}{8k_{max}} \tag{3.6}$$

The displacement field inside each thin layer is approximated by means of the interpolation function (shape function), i.e., $\mathbf{u} = \mathbf{NU}$, where $\mathbf{U}$ is a vector containing the nodal displacements. Also, $\mathbf{N} = \mathbf{N}(\xi)$ is the shape function matrix of the form, $\mathbf{N} = [N_1\mathbf{I}\ N_2\mathbf{I}\ N_3\mathbf{I}]$ where N_a is the shape function and $\mathbf{I}$ the 3×3 identity matrix and ξ represents the local coordinate. For a three noded thin-layer element, the shape functions are:

$$N_1(\xi) = \frac{1}{2}\xi^2 - \frac{1}{2}\xi \tag{3.7}$$

$$N_2(\xi) = 1 - \xi^2 \tag{3.8}$$

$$N_3(\xi) = \frac{1}{2}\xi^2 + \frac{1}{2}\xi \tag{3.9}$$

Next, strains and stresses inside each layer are approximated as [ε] = [**B**][**U**] and [σ] = [**D**][ε] = [**D**][**B**][**U**], where [**B**] is the strain matrix and [**B**] = [$\mathbf{B_1}$ $\mathbf{B_2}$ $\mathbf{B_3}$], in which $\mathbf{B}_a$ (a = 1, 2 and 3) is defined as:

$$[\mathbf{B}_a] = \begin{pmatrix} ik_xN_a & 0 & 0 \\ 0 & ik_yN_a & 0 \\ 0 & 0 & \frac{\partial N_a}{\partial z} \\ ik_yN_a & ik_xN_a & 0 \\ 0 & \frac{\partial N_a}{\partial z} & ik_yN_a \\ \frac{\partial N_a}{\partial z} & 0 & ik_xN_a \end{pmatrix} \tag{3.10}$$

Where k_x and k_y are the Fourier images of the x and y directions respectively.

Then, rewriting $\mathbf{B}_a$ as: $[\mathbf{B}_a] = [\mathbf{B}_a]_1 + ik_x[\mathbf{B}_a]_2 + ik_y[\mathbf{B}_a]_3$, where

$$[\mathbf{B}_a]_1 = \begin{pmatrix} 0 & 0 & 0 \\ 0 & 0 & 0 \\ 0 & 0 & \frac{\partial N_a}{\partial z} \\ 0 & 0 & 0 \\ 0 & \frac{\partial N_a}{\partial z} & 0 \\ \frac{\partial N_a}{\partial z} & 0 & 0 \end{pmatrix} \tag{3.11}$$

$$[\mathbf{B}_a]_2 = \begin{pmatrix} N_a & 0 & 0 \\ 0 & 0 & 0 \\ 0 & 0 & 0 \\ 0 & N_a & 0 \\ 0 & 0 & 0 \\ 0 & 0 & N_a \end{pmatrix} \tag{3.12}$$

$$[\mathbf{B}_a]_3 = \begin{pmatrix} 0 & 0 & 0 \\ 0 & N_a & 0 \\ 0 & 0 & 0 \\ N_a & 0 & 0 \\ 0 & 0 & N_a \\ 0 & 0 & 0 \end{pmatrix} \tag{3.13}$$

The wave equation for the thin-layer system is simplified and expressed in the frequency-wavenumber domain as ($[\mathbf{K}]$ - $\omega^2[\mathbf{M}]$)$\mathbf{U} = \mathbf{P}$, where $\mathbf{U}$ and $\mathbf{P}$ are displacements and tractions, respectively, and $\mathbf{M}$ is the corresponding mass matrix. $[\mathbf{K}]$ is the global stiffness matrix:

$$[\mathbf{K}] = [\mathbf{K_0}] + ik_x[\mathbf{K_1}] + ik_y[\mathbf{K_2}] + k_x^2[\mathbf{K_3}] + k_y^2[\mathbf{K_4}] + k_xk_y[\mathbf{K_5}] \tag{3.14}$$

Where:

$$[\mathbf{K_0}] = \int_0^h [\mathbf{B_1}]^T [\mathbf{D}][\mathbf{B_1}]|J|d\xi \tag{3.15}$$

$$[\mathbf{K_1}] = \int_0^h [\mathbf{B_1}]^T [\mathbf{D}][\mathbf{B_2}]|J|d\xi - \int_0^h [\mathbf{B_2}]^T [\mathbf{D}][\mathbf{B_1}]|J|d\xi \tag{3.16}$$

$$[\mathbf{K_2}] = \int_0^h [\mathbf{B_1}]^T [\mathbf{D}][\mathbf{B_3}]|J|d\xi - \int_0^h [\mathbf{B_3}]^T [\mathbf{D}][\mathbf{B_1}]|J|d\xi \tag{3.17}$$

$$[\mathbf{K_3}] = \int_0^h [\mathbf{B_2}]^T [\mathbf{D}][\mathbf{B_2}]|J|d\xi \tag{3.18}$$

$$[\mathbf{K_4}] = \int_0^h [\mathbf{B_3}]^T [\mathbf{D}][\mathbf{B_3}]|J|d\xi \tag{3.19}$$

$$[\mathbf{K_5}] = \int_0^h [\mathbf{B_2}]^T [\mathbf{D}][\mathbf{B_3}]|J|d\xi + \int_0^h [\mathbf{B_3}]^T [\mathbf{D}][\mathbf{B_2}]|J|d\xi \tag{3.20}$$

Also, $|J|$ is the determinant of the Jacobian matrix and $\mathbf{D}$ is the constitutive matrix of an isotropic material and can be defined as:

$$\mathbf{D} = \begin{pmatrix} (\lambda+2G) & \lambda & \lambda & 0 & 0 & 0 \\ \lambda & (\lambda+2G) & \lambda & 0 & 0 & 0 \\ \lambda & \lambda & (\lambda+2G) & 0 & 0 & 0 \\ 0 & 0 & 0 & G & 0 & 0 \\ 0 & 0 & 0 & 0 & G & 0 \\ 0 & 0 & 0 & 0 & 0 & G \end{pmatrix} \tag{3.21}$$

Where λ and G are the Lame constants in the isotropic plane, i.e., horizontal plane (Bian et al. [23]).

This classic thin-layer formulation gives the response of a medium with a fixed rigid base, however an infinitely deep soil is required for the majority of critical velocity problems. To overcome this, a variety of absorbing boundary formulations have been proposed (Kausel [97], Barbosa et al. [16]). In this work, Thompson-Haskell matrices are formed in a similar manner to the previous derivation and appended to those above. The size of each matrix is $3(n+1) \times 3(n+1)$ to account for the displacements in vertical, horizontal and longitudinal directions at the half-space interface.

Equivalent stiffness formulation

Solving the system of equations (Equation 3.1 and Equation 3.3) returns the displacements of all track components, including the lowermost layer (u_{bb}) due to a vertical unit load on the rail (Alves Costa et al. [5], Dong et al. [53], Dong et al. [47], Dong et al. [50]). These displacements can then be scaled linearly to account for a point load of arbitrary magnitude. However, to compute soil displacements for a load of arbitrary magnitude, the displacement Green's function $R_u(k_x,k_y,\omega)$ for each individual soil thin layer is scaled as:

$$R_u(k_x,k_y,\omega) = (L(k_x,\omega)C_{tg})u^g(k_x,k_y,\omega) \tag{3.22}$$

Where $u^g(k_x,k_y,\omega)$ is the ground displacement Green's function in the wavenumber-frequency domain. Similarly, $u^g(k_x,k_y,\omega)$ can be replaced by the stress and strain Green's functions: $\sigma^g(k_x,k_y,\omega)$ and $\varepsilon^g(k_x,k_y,\omega)$, to obtain the stress/strain response in the soil. This procedure also is indicated in Appendix A. The strain Green's function is required to compute the soil strain levels needed for the equivalent linear formulation. Also, $L(k_x,\omega)C_{tg}$ is the load scale function, where C_{tg} is given in Equation 3.4 and Equation 3.5. $L(k_x,\omega)$ represents the load transmitted by the track to the ground and is computed by multiplication of the equivalent stiffness and lower track displacement:

$$L(k_x,\omega) = k_{eq}(k_x,\omega)u_{bb}(k_x,\omega) \tag{3.23}$$

Finally, the ground response (displacement, stress or strain) for an individual layer in the time-space domain is computed by inverting the scaled Green's function using the inverse Fourier transform:

$$R(x,y,t) = \frac{1}{(2\pi)^3}\int_{-\infty}^{+\infty}\int_{-\infty}^{+\infty}\int_{-\infty}^{+\infty} R_u(k_x,k_y,\omega)e^{i(\omega t-k_x x-k_y y)}\,dk_x\,dk_y\,d\omega \tag{3.24}$$

It is worth noting that because the TLM model is computed in the wavenumber-frequency domain, the moving load effect is taken into account using the shift property of the Fourier transform that allows frequency to be related to wavenumber, i.e., $\omega = \Omega - k_x c$, where Ω is the excitation frequency (set to 0Hz in this work), k_x is the wavenumber in the direction of moving load, and c is the moving load velocity.

3.3 Model validation

The model is validated against three test cases which are a combination of numerical and experimental results. Firstly, its ability to model soil improvement below a railway track is verified. Next its output is compared against numerical results from published literature, and finally it is validated against experimental results from a railway line in Portugal (Alves Costa et al. [2], Santos et al. [149]).

3.3.1 Soil replacement validation

One advantage of using the TLM approach for soil modelling is that it is computationally efficient compared to 3D FE analysis. However, one limitation compared to 3D approaches is that all horizontal layers are infinitely long/wide. This is acceptable for many problems because the soil layers below and near the track can be assumed to be horizontal and infinite. However, when considering soil replacement/improvement, to minimise cost, remediation is typically only performed directly below the track. The TLM cannot capture this localised improvement and instead assumes the improvement is infinite rather than just below the track (Dong et al. [50]).

To determine the effect of this assumption on the ability of the proposed model to simulate soil replacement, 3D FE tests are performed using ABAQUS. The 3D track consists of rail, railpad, slab and sub-ballast components. The track is fully coupled to a 3D soil model with x, y, z dimensions: $50m \times 32m \times 12m$; which utilises infinite element absorbing boundaries in the free-field to reduce artificial reflections. Two soils, with constant density, 2000kg/m^3, are considered in Figure 3.8. It is worth mentioning that the density of soil is influenced by a number of factors including stiffness and Poisson ratio, constant density is chosen in the validation for the simplicity purpose.

1. In real-life, when considering soil replacement, it is likely that due to the practicalities of construction the sides of the replacement zone would be sloped (dashed grey lines in Figure 3.8). However, for validation the improved area is considered to have vertical sides (solid grey lines in Figure 3.8). This is the worst-case scenario and thus most likely to challenge the limitations of the model. The Young's modulus of the improved soil is 150MPa, while the Young's modulus of the non-remediated soil is set to 45MPa. Considering that soil improvement can be undertaken to an arbitrary depth, and that it is the vertical improvement edges likely to introduce errors, the soil improvement is considered for the full model depth.

2. A fully homogeneous soil with properties: 150MPa. This represents the TLM approximation of post-soil improvement where the improvement was performed to the infinite horizontal layers.

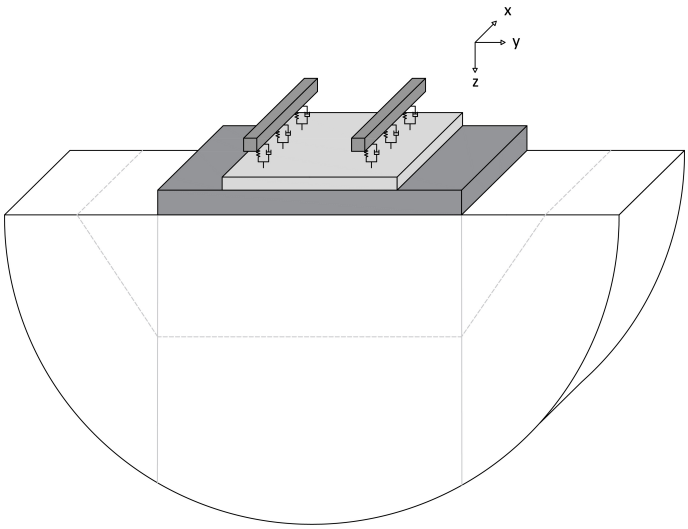

Fig. 3.8 Layout of soil replacement geometry

To compare the results generated by both models, track receptance is considered. Numerically, Figure 3.9a reveals the results for all frequencies are similar. A small discrepancy is seen at low frequency which is governed by the static stiffness of the overall track-ground model, however the difference is negligible. This is because wave energy first propagates from the track into the soil directly below the track (i.e. where remediation is located). Then, when it spreads from this region, for the case of the remediated soil it moves through a stiff to soft soil interface thus not generating significant reflection. Similarly, in the homogenous TLM assumption, it also does not experience a reflection, thus making the approximations similar. Further, Figure 3.9b compares the track displacement time history for a train running close to the critical velocity (550km/h) for both cases. It is seen that again the response is similar, with a small discrepancy in the peak value. Therefore, considering the validation is for the most challenging test case (i.e., case of a vertical replacement barrier) it can be concluded that the proposed model is capable of accurately modelling the effects of soil replacement.

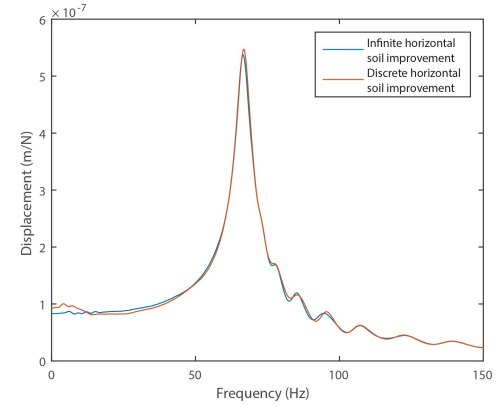

(a)

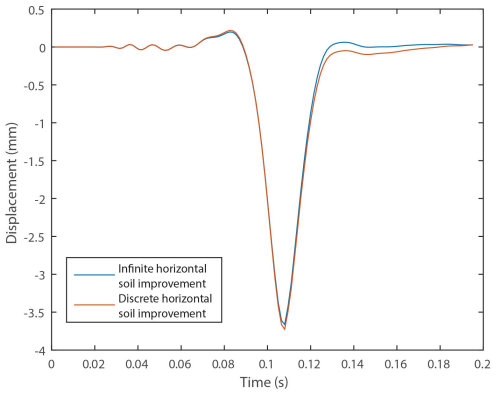

(b)

Fig. 3.9 Comparison between simplified and detailed soil replacement geometry (a) static rail receptance excitation; (b) moving load excitation time history

3.3.2 Numerical validation

A numerical comparison is made against an alternative, peer-reviewed and validated track-ground railway model (Kaynia et al. [100]). Like all models though, the peer-reviewed approach was originally found to have discrepancies between its results and field data (Kaynia et al. [100]). Therefore, it is intended for a qualitative comparison.

Figure 3.10 illustrates the modelling scenario, for which a combined track/embankment structure rests on a multi-layered soil. Also, the soil is composed of 5 layers, with the lowest layer being infinitely deep, as described in Table 3.1. However, it should be noted that to account for non-linear soil behaviour (i.e. stiffness degradation with strain), the soil properties in the previous study are manually changed to account for this (Kaynia et al. [100]). Therefore, to ensure consistency between validations, the same 'degraded' properties are used for comparison (i.e. the track/embankment has a bending rigidity EI of 80 MN/m^2 when the train speed is either 185 km/h or 200 km/h, and 200 MN/m^2 when the train speed is 70 km/h). It is worth

noting that the bending stiffness is updated by changing the Young's modulus E, instead of changing the dimensions of the embankment. Train loading, as shown in Figure 3.11, is chosen to replicate an X2000 train running in two directions (Northbound and Southbound), at speeds of 70, 185 and 200km/h (detailed in Table 3.2).

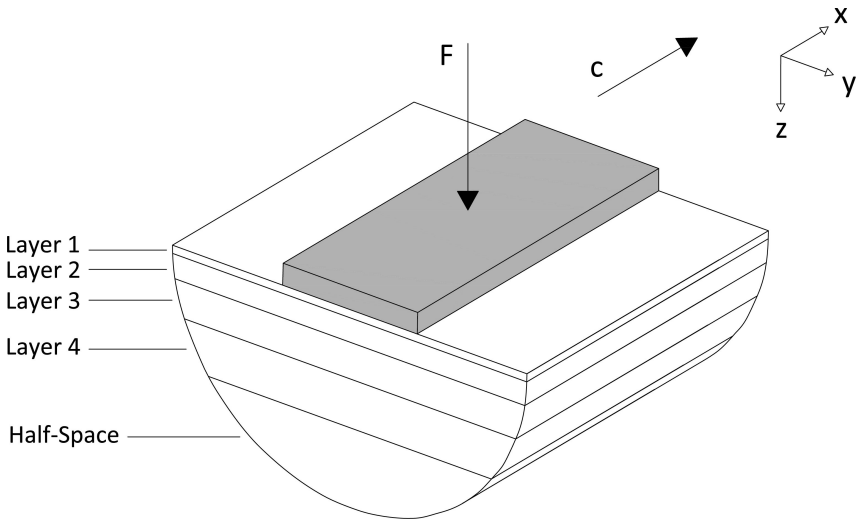

Fig. 3.10 Schematic representation of track-ground interaction model

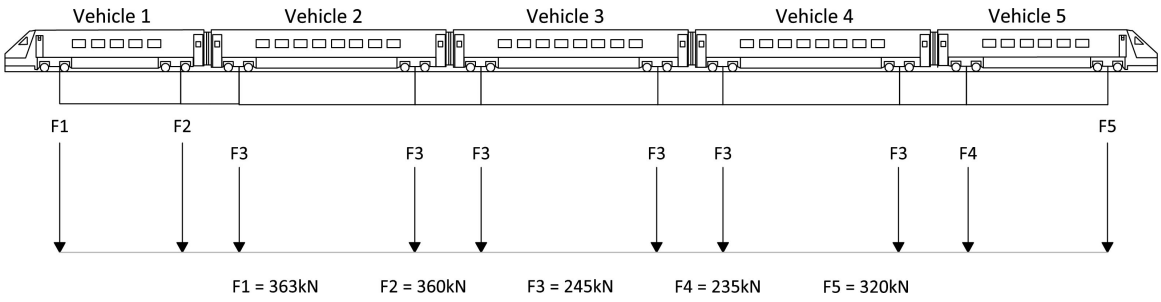

Fig. 3.11 Train boogie loads applied in the numerical simulation

Table 3.1 Soil properties used in the simulation for train velocity of 70km/h and 200km/h (Kaynia et al. [100])

Soil layer	Layer thickness (m)	Density (kg/m^3)	Young's modulus (MPa)		Poisson ratio		Damping	
			c = 70	c ≥ 185	c = 70	c ≥ 185	c = 70	c ≥ 185
Crust	1.1	1500	23	19	0.49	0.49	0.04	0.063
Organic clay	3	1260	6	4	0.5	0.5	0.02	0.058
Clay 1	4.5	1475	19	16	0.5	0.5	0.05	0.098
Clay 2	6	1475	33	32	0.5	0.5	0.05	0.064
Half-space	–	1475	44	44	0.5	0.5	0.05	0.06

Table 3.2 Velocity and direction of the compared simulation cases

	Case 1	Case 2	Case 3
Velocity (km/h)	70 km/h	185 km/h	200 km/h
Direction	Southbound	Northbound	Southbound

Figure 3.12 shows the rail displacement time history comparison between the published result and the solution calculated using the proposed model. In this example, the velocity is lower (70 km/h) than the critical speed, meaning the response is relatively quasi-static. This is representative of a soft-soil site, where although significant wave propagation is not occurring (i.e. the train speed is not close to the critical velocity), track displacements are still high. It is seen that the new model is a strong match to the published data.

Figure 3.13 shows the second validation, at the higher speed of 185km/h in the Northbound direction. On this occasion the train speed is closer to the critical velocity meaning dynamic wave propagation is significantly more prominent than that at 70km/h. This results in amplified displacements, in both the upward and downward directions, particularly for the leading and trailing wheels. Again the model is able to accurately predict track response. The discrepancy at higher frequencies is partly due to having to approximate the published time histories because raw time history data was unavailable.

Finally, Figure 3.14 shows the comparison between the proposed model and the published results at a speed of 200km/h. Again the speed is close to the critical velocity and the dynamic effects are dominant. However, compared to the speed of 185km/h, the displacements associated with the leading and trailing wheels have reduced, while the response due to the central wheels has increased. Again, the model predicted this accurately. Therefore is it concluded that the model is accurate and any discrepancies between models are as likely to be from the published result as from the proposed model. Also, it should be stated that the track-ground coupling in the model presented by Kaynia et al. [100] is slightly different from the presented approach, since hybrid time-frequency domain is adopted in the former model.

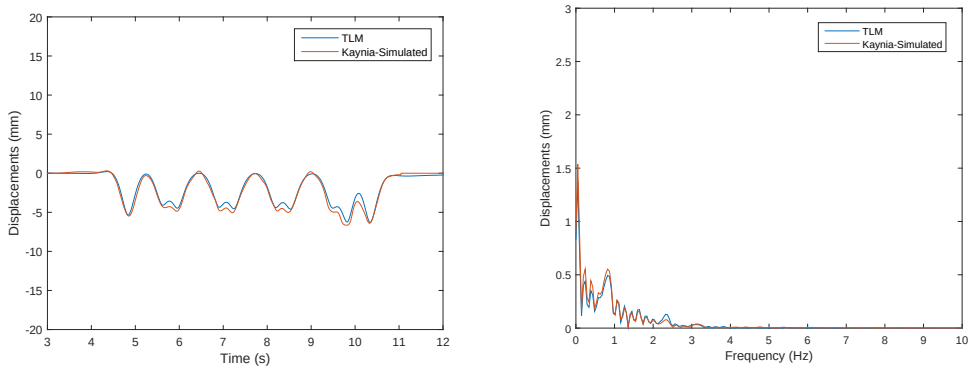

(a) (b)

Fig. 3.12 Track displacement for Southbound train at 70km/h (case 1) in timn domain (a) and frequency domain (b)

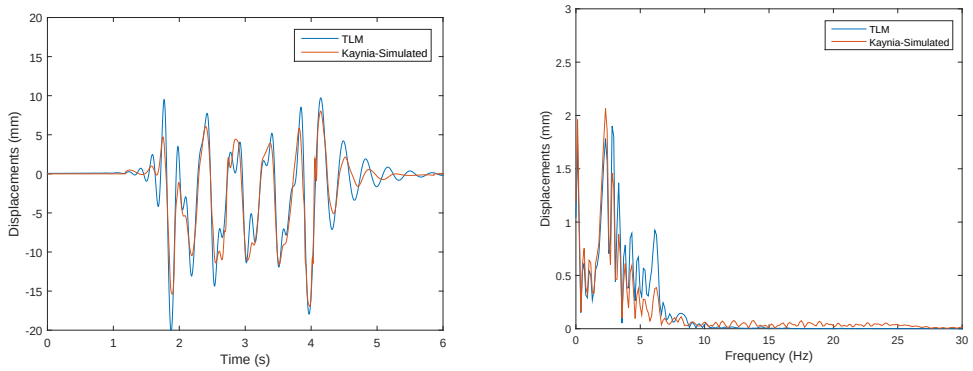

(a) (b)

Fig. 3.13 Track displacement for Northbound train at 185km/h (case 1) in timn domain (a) and frequency domain (b)

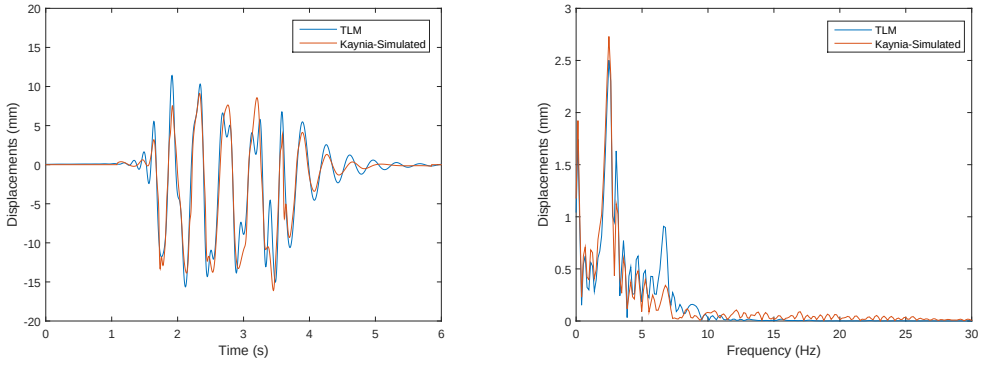

(a) (b)

Fig. 3.14 Track displacement for Southbound train at 200km/h (case 1) in timn domain (a) and frequency domain (b)

3.3.3 Experimental validation

In addition to numerical validation, an experimental validation is performed against data from a railway line in western Portugal, near the town of Carregado. At this site, a comprehensive series of tests were used to assess the soil characteristics, track properties and the system response due to the passage of Alfa-Pendular trains (Alves Costa et al. [2]).

The train is composed of 6 vehicles, with the geometry and axle loads shown in Figure 3.15. Regarding the geometric settings of the model, there are 10 soil layers supported by bedrock, and ballast and sub-ballast lay on top of the uppermost soil layer. The height of the ballast is 0.57m, the Young's modulus 97MPa, the Poisson ratio 0.12 and the density 1590 kg/m^3. The same parameters but for the sub-ballast are 0.55m, 212MPa, 0.2 and 1910 kg/m^3, respectively. One difference between the track described in Equation 3.1 and that at Carregado, is the presence of a sub-ballast layer below the ballast. To account for this change, the analytical track equation is modified as shown in Equation 3.25 and Equation 3.26, where $E_{sb}, C_{psb}, h_{sb}, u_{sb}$ are the Young's modulus, compression wave speed, thickness and displacement of the sub-ballast, respectively.

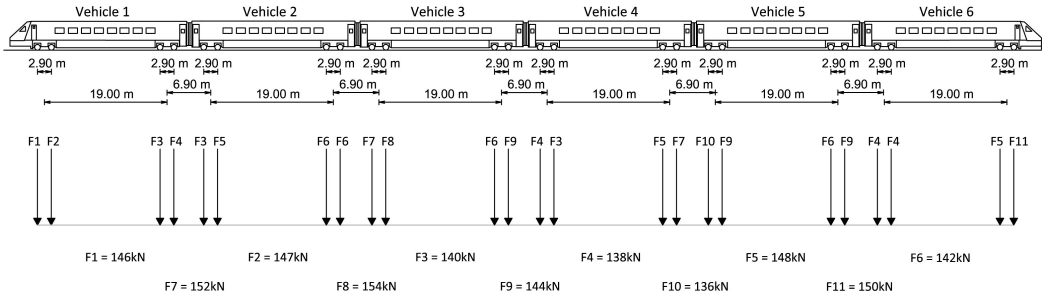

Fig. 3.15 Geometry and mechanical properties of the Alfa-Pendular train

$$A \times \begin{pmatrix} \tilde{u_r}(k_x, \omega) \\ \tilde{u_s}(k_x, \omega) \\ \tilde{u_b}(k_x, \omega) \\ \tilde{u_{sb}}(k_x, \omega) \end{pmatrix} = \begin{pmatrix} \tilde{P}(k_x, \omega) \\ 0 \\ 0 \\ 0 \end{pmatrix} \tag{3.25}$$

$$A = \begin{bmatrix} EI_r k_x^4 + k_p^* - \omega^2 m_r & -k_p^* & 0 & 0 \\ -k_p^* & k_p^* + \frac{2\omega E_b^* b\alpha}{\tan(\frac{\omega h_b}{C_{pb}})C_{pb}} - \omega^2 m_s & -\frac{2\omega E_b^* b\alpha}{\sin(\frac{\omega h_b}{C_{pb}})C_{pb}} & 0 \\ 0 & -\frac{2\omega E_b^* b\alpha}{\sin(\frac{\omega h_b}{C_{pb}})C_{pb}} & \frac{2\omega E_b^* b\alpha}{\tan(\frac{\omega h_b}{C_{pb}})C_{pb}} + \frac{2\omega E_{sb}^* b\alpha}{\tan(\frac{\omega h_{sb}}{C_{psb}})C_{psb}} & -\frac{2\omega E_{sb}^* b\alpha}{\sin(\frac{\omega h_{sb}}{C_{psb}})C_{psb}} \\ 0 & 0 & -\frac{2\omega E_{sb}^* b\alpha}{\sin(\frac{\omega h_{sb}}{C_{psb}})C_{psb}} & \frac{2\omega E_{sb}^* b\alpha}{\tan(\frac{\omega h_{sb}}{C_{psb}})C_{psb}} + k_{eq} \end{bmatrix} \tag{3.26}$$

Figure 3.16a compares the simulated rail displacement and the field measurement in the time domain. Further, Figure 3.16b shows the corresponding frequency content comparison. It is seen that there is a strong match between the predicted and measured values. Regarding the time history, the correlation is strong for both the magnitude and timing of response. Regarding the frequency content, the key dominant frequencies and their harmonics are accurately simulated. Any small discrepancies at high frequencies are likely to have been due to wheel-rail irregularities, or to any other dynamic excitation mechanisms, which were ignored during prediction, since only quasi-static excitation is taken into account.

Figure 3.17a shows the sleeper velocity during train passage and Figure 3.17b shows the corresponding frequency content. Again the agreement is strong for both cases.

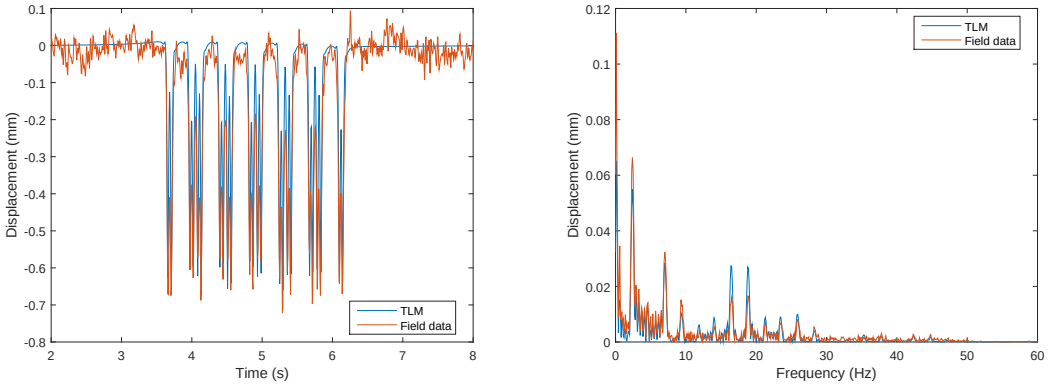

(a) (b)

Fig. 3.16 Rail displacement due to the train passage in both time content (a) and in frequency content (b)

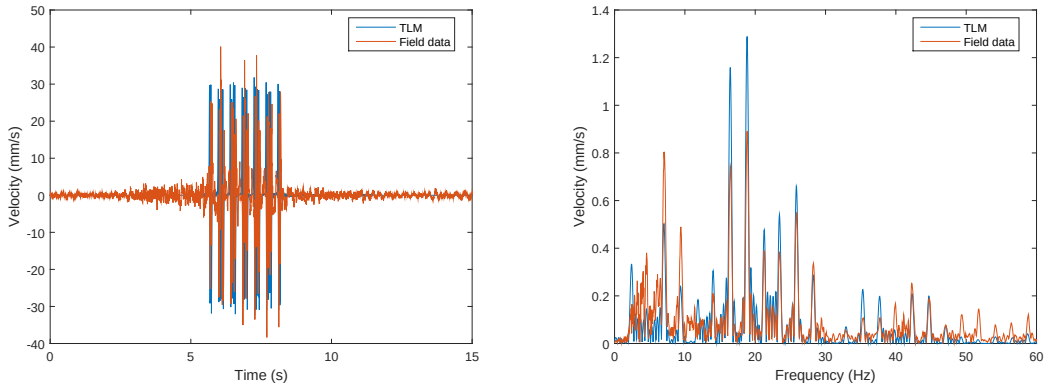

(a) (b)

Fig. 3.17 Vertical sleeper velocity due to the train passage in both time content (a) and in frequency content (b)

3.4 Soil replacement strategies

On railway lines, areas of low stiffness ground can be remediated using a variety of techniques, including soil replacement and soil improvement. These techniques are expensive, particularly as depth of remediation increases, meaning it is desirable to optimise/minimise improvement depth. This is challenging to determine because at high train speeds, the low frequency wave energy generated penetrates deep into the underlying soil. This can be solved using the model because its thin-layer formulation makes it well suited for analysing the effect of soil replacement and soil improvement.

To show the capabilities of the model, three soil test cases are undertaken to determine the effect of improvement depth and stiffness for both ballasted and slab tracks. They are chosen to represent scenarios that could be encountered at soft soil sites and have the properties outlined in Table 3.3:

1. A homogenous low stiffness soil
2. A low stiffness soil overlying a stiffer soil
3. A low stiffness soil sandwiched below a stiff embankment and above a stiffer underlying soil

Regarding soil improvement, for each of the three cases, the soft soil is improved to a maximum depth of 5m, considering the effect of five cumulative 1m thick improvements. All improvements are considered as a homogeneous horizontal layer and the track displacement is analysed for each. Further, for case 1, three different stiffness' of improvement are considered. The train loading is a single 18 tonne axle load moving at

330 km/h, which is considered as the maximum operational speed for new high speed rail lines in UK, for all three study cases. The ballasted and slab track properties are shown in Table 3.4.

Table 3.3 Soil properties

Soil	Layer thickness (m)	Young's modulus (MPa)	Poisson's ratio	Density (kg/m^3)	Damping
1	[∞]	[45]	0.35	1800	0.03
2	[5 ∞]	[45 120]	0.35	1800	0.03
3	[2 5 ∞]	[200 45 120]	0.35	1800	0.03

Table 3.4 Track properties (ballasted track and slab track)

		Ballasted track	Slab track
Rail	EI_r (Nm^2)	1.26×10^7	1.26×10^7
	m_r (kg/m)	120	120
Railpad	k_p (N/m)	5.5×10^8	5.5×10^8
	c_p (Ns/m)	2.5×10^5	2.5×10^5
Sleepers	m_s (kg/m)	490	-
Ballast/Slab	h (m)	0.35	0.35
	E (MPa)	150	30000
	2b(m)	2.5	2.5
	ρ (kg/m^3)	1600	2500

3.4.1 Soil case 1

Soil test case 1 consists of a homogenous, infinitely deep soil with a stiffness of 45MPa. Five different depths of soil improvement from the soil–track interface are considered (1, 2, 3, 4, 5m), and for each, three different magnitudes of stiffness improvement are tested (150, 200, 250MPa).

Figure 3.18 shows the effect on rail displacement due to these changes for both ballasted and slab tracks, with the results further summarised in Table 3.5. As expected, all displacements for the ballasted track are greater than those for the concrete slab. Considering the ballasted track, all depths of improvement result in reduced displacements, however adding additional improvement at large depth below the ground has less of

an effect than at the surface (e.g. adding 1m of improvement to the natural soil provides a greater percentage of reduction compared to adding 1m at a depth of 4m). This is because the Rayleigh wave energy is confined close to the soil surface.

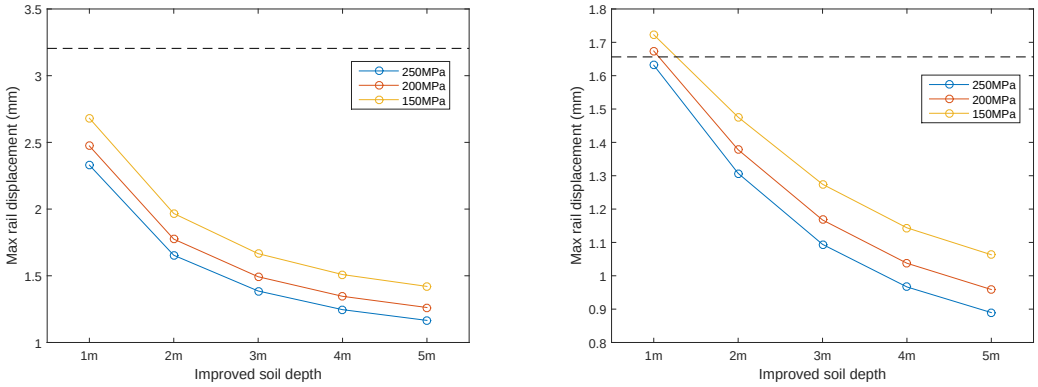

Fig. 3.18 Maximum vertical rail displacement for Soil 1. (a) Ballasted track; (b) Slab track; Dashed black line represents the original value

Table 3.5 Rail displacement improvement in percentage terms for Soil 1 at a train speed of 330km/h

Soil layer	150 MPa		200 MPa		250 MPa	
	Ballasted	Slab	Ballasted	Slab	Ballasted	Slab
1m	16.3%	-4.0%	22.8%	-1.1%	27.3%	1.5%
2m	38.6%	10.9%	44.6%	16.8%	48.3%	21.1%
3m	48.1%	23.1%	53.4%	29.5%	56.7%	33.9%
4m	52.9%	30.9%	58.0%	37.3%	61.1%	41.6%
5m	55.7%	35.8%	60.6%	42.1%	63.6%	46.3%

Considering the slab track, the performance benefits are less clear, with 1m of improvement (at 150 and 200MPa stiffness's) resulting in increased track deflections. This can be explained by analysing the relationship between train speed and rail deflections, (i.e. the dynamic amplification factor). Figure 3.19 shows this relationship for the cases of no soil improvement and 1m of improvement. It is seen that the train speed is marginally past the critical velocity when no improvement is performed. However, improving the ground stiffness shifts the critical velocity to a higher speed meaning that the 1m improvement cases are located closer to the peak, resulting in greater displacement amplification. Other than these cases, track

displacements are lower than the non-improved case for all improvement depths and stiffness's. Again, the relationship between depth of improvement and rail displacements is non-linear.

Regarding the effect of the stiffness of the replacement soil, as expected, stiffer soils result in lower track deflections. For example, for the ballasted 1m replacement case, the rail displacements are 2.71mm and 2.35mm when the replacement stiffness is 150 and 250MPa, respectively. Comparing this to the 2m case, 2m of 150MPa soil has a rail displacement of 1.97mm, meaning the use of 2m of softer fill provides better performance than 1m of stiffer fill. Alternatively though, at greater depths the opposite is true, for example with 4m of stiffer fill providing lower deflections than 5m of softer fill. Also, for the ballasted track, the displacement reduction between 150, 200 and 250MPa is relatively constant for all depths of improvement. However, for the slab track this not true, with the percentage benefit between 150MPa and 250MPa at 1m, lower than that for the 5m case. Therefore, considering the non-linear relationships between improved soil stiffness and improvement depth, soil remediation must be undertaken carefully to ensure displacement tolerances are met and cost is minimised.

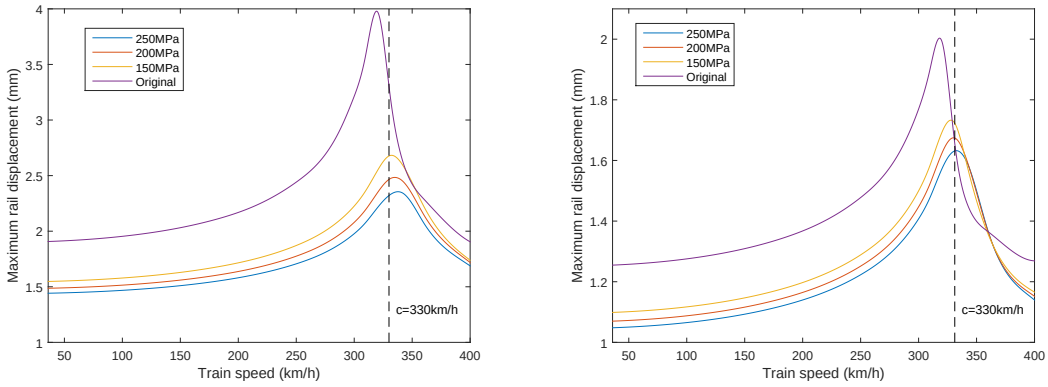

Fig. 3.19 Maximum vertical rail displacement vs train speed, for Soil 1 with 1m of soil replacement. (a) Ballasted track; (b) Slab track; Dashed black line represents train speed

Additionally, Figure 3.20 shows a stress time history comparison at the surface of the soil below the central line of the ballasted track, for speeds 20m/s and 92m/s. It is observed that the shape of the stress time histories for low speed is regular but oscillations occur as it approaches the critical velocity. Comparing the maximum stress values at different speeds, the x and y stress components increase by 423% and 448%, respectively, while the xz shear stress increases by 371%. In comparison, although the maximum z stress component remains the largest, it only increases by 124% due to the speed change. Therefore at low speed

the response is dominated by the vertical response, while at critical speed the entire stress field becomes important.

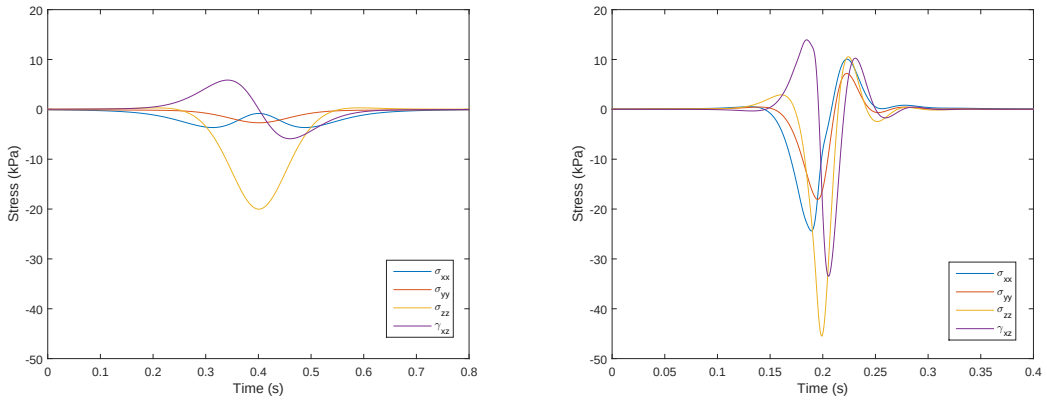

(a) (b)

Fig. 3.20 Stress time history comparison at the surface for ballasted track. (a) c=20m/s (b) c=92m/s

3.4.2 Soil case 2

Soil test case 2 consists of a 5m deep soft layer (45MPa) overlying a stiffer layer (120MPa), which is homogenous, and infinitely deep. Five different depths of soil improvement from the soil–track interface are considered (1, 2, 3, 4, 5m), where 5m means all of the soft 45MPa layer is replaced. For each case, the soft layer is replaced with a soil of stiffness of 250MPa, and the effect on rail displacement is analysed. Figure 3.21 shows the effect of soil replacement for both ballasted and slab track cases, with the percentage terms shown in Table 3.6. Again the concrete slab track has lower deflections due to its elevated bending stiffness, however in contrast to soil case 1, all depths of improvement result in reduced track deflections. For the ballasted track the relationship between improvement depth and rail displacement is highly non-linear. When 1m of improvement is performed, displacements reduce by 49.1%, however the reductions are only 64.4, 69.4, 71.8 and 73.2% for 2, 3, 4, 5m replacements respectively. Therefore for this case, depending upon the desired deflection levels, it may be most cost effective to remediate only the top 1m of soil. For the slab track the relationship is also non-linear, however less pronounced. Again, increasing improvement depth reduces deflections, however the change in performance benefit reduces as the improvement depth approaches 5m.

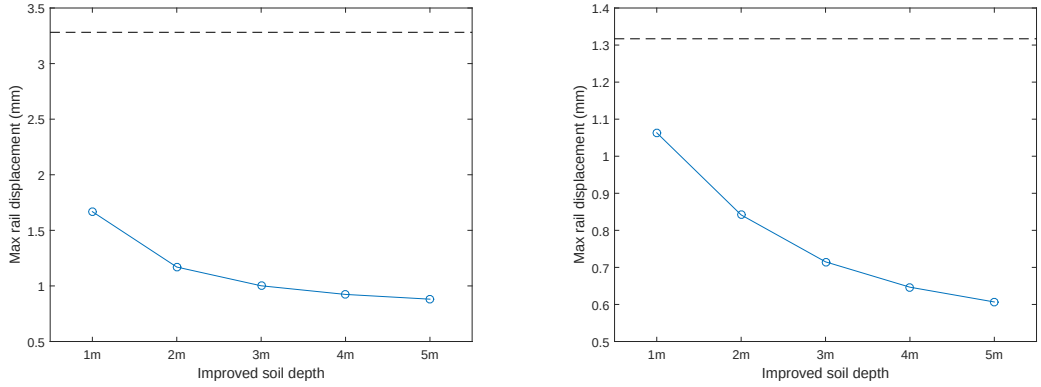

Fig. 3.21 Maximum vertical rail displacement for Soil 2. (a) Ballasted track; (b) Slab track; Dashed black line represents the original value

Table 3.6 Rail displacement improvement in percentage terms for Soil 2 at a train speed of 330km/h

Improvement depth	250 MPa	
	Ballasted	Slab
1m	49.1%	19.3%
2m	64.4%	36.1%
3m	69.4%	45.7%
4m	71.8%	50.9%
5m	73.2%	53.9%

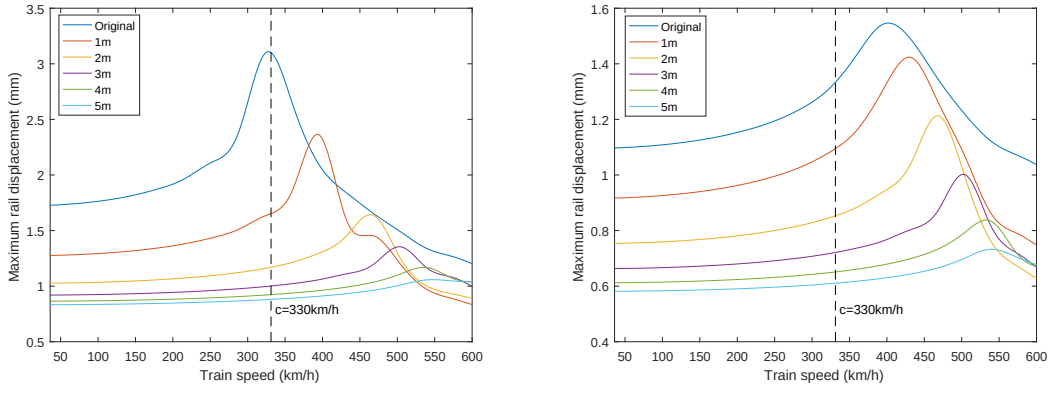

Fig. 3.22 Maximum vertical rail displacement vs train speed, for Soil 2 with different depths of soil replacement strategies. (a) Ballasted track; (b) Slab track

Figure 3.23 shows the effect of soil replacement on displacements. It is seen that the unmodified soil gives rise to significant wave propagation, with 'Mach cone' type contours present. In comparison, for the fully remediated soil stratum, the response is more symmetric in both horizontal directions.

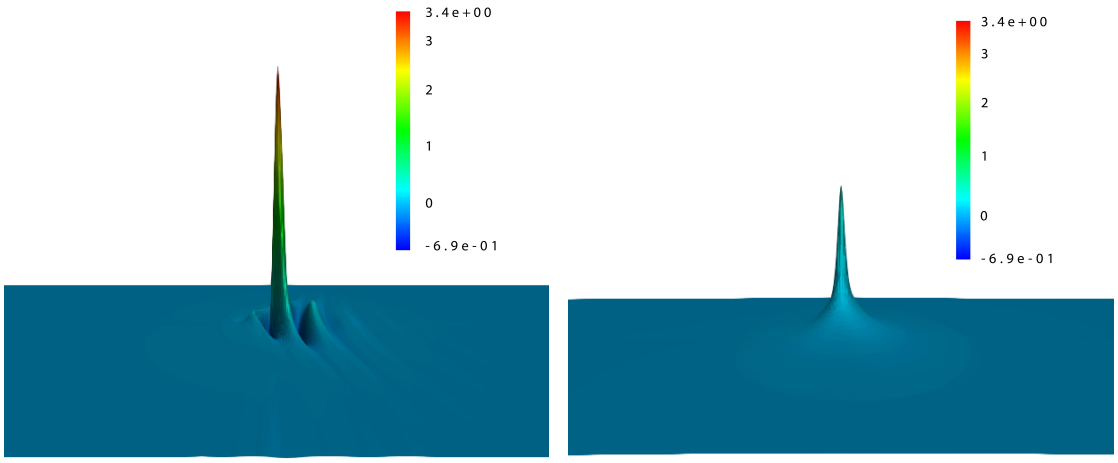

(a) (b)

Fig. 3.23 Rail displacement comparisons for Soil 2. (a) Original soil; (b) 5m depth of improvement

3.4.3 Soil case 3

Soil test case 3 is chosen to determine the effect of an embankment (Kouroussis et al. [105], Olivier et al. [139]) overlying a soft soil site. Therefore it consists of a 2m high embankment overlying the soft-stiff stratum from soil case 2 (Figure 3.24). The embankment is modelled in a simplified manner, i.e., considering it as an additional layer, infinite in the transversal direction. To simulate the presence of an embankment, it is modelled as an additional soil layer, which has been shown to be a reasonable approximation in Alves Costa et al. [4]. This results in a 5m thick soft layer (45MPa) sandwiched between two stiffer layers. The upper embankment layer has a stiffness of 200MPa and the lower ground layer is infinitely deep with a stiffness of 120MPa. Again, improvement depths between 1-5m are considered.

Figure 3.25 shows the relationship between soil replacement depth and track displacement. It is observed that the stiff embankment causes a significant reduction in rail displacement compared to Figure 3.21. This is because the dispersion characteristics are shifted the critical velocity to a higher value, due to the presence of the embankment. Similar to soil case 2, all improvement depths result in reduced track displacements, however the relationship is no longer relatively linear. Instead, only a small reduction is achieved by improving 2m compared to 1m, while improving 3m compared to 2m results in a large reduction. This is

true for both track types, but more pronounced for the ballasted case. Therefore, depending on the desired rail deflection tolerances, it might be most efficient to replace the top 3m rather than either 2 or 4m. It should also be noted that although the rail displacements for this particular track-soil combination may not have required remediation in practice, the finding of non-linearity in soil improvement depth is also applicable to other track-soil stiffness combinations.

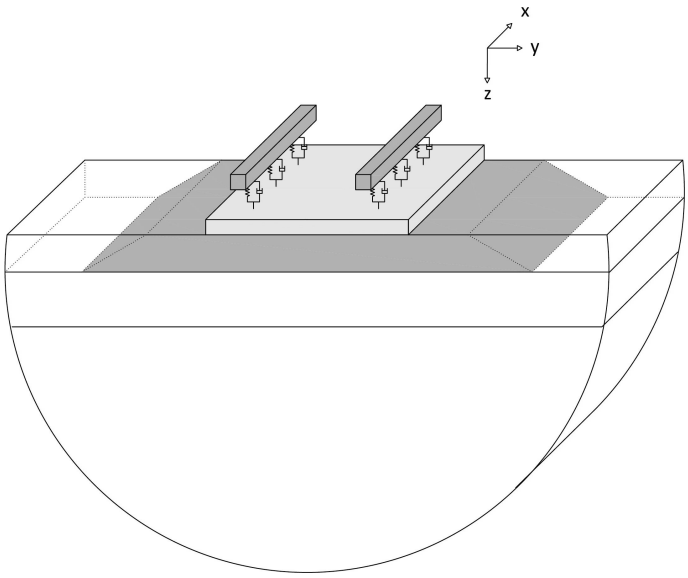

Fig. 3.24 Schematic diagram of the slab track used in the simulation overlaying on the soil

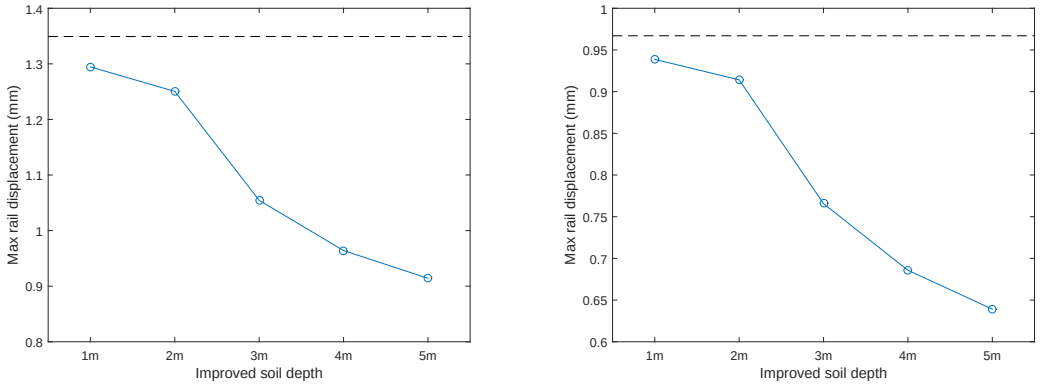

(a) (b)

Fig. 3.25 Maximum vertical rail displacement for Soil 3. (a) Ballasted track; (b) Slab track; Dashed black line represents the original value

In addition to rail displacements, Figure 3.26 shows the resulting maximum vertical stresses within the embankment (2m) and soil to a depth of 5m below the embankment. It is seen that despite the soil replacement having a significant impact on rail deflections, the effect on stress levels is less defined. This is particularly true for the ballasted track, however for the slab track, although the stresses for stiffer soils are

lower at 7m compared to the softer soils, the upper 2m of the stiffer soil experiences slightly higher stress levels.

Table 3.7 Rail displacement improvement in percentage terms for Soil 3 at a train speed of 330km/h

Improvement depth	250 MPa	
	Ballasted	Slab
1m	4.0%	2.9%
2m	7.3%	5.5%
3m	21.8%	20.8%
4m	28.5%	29.1%
5m	32.2%	33.9%

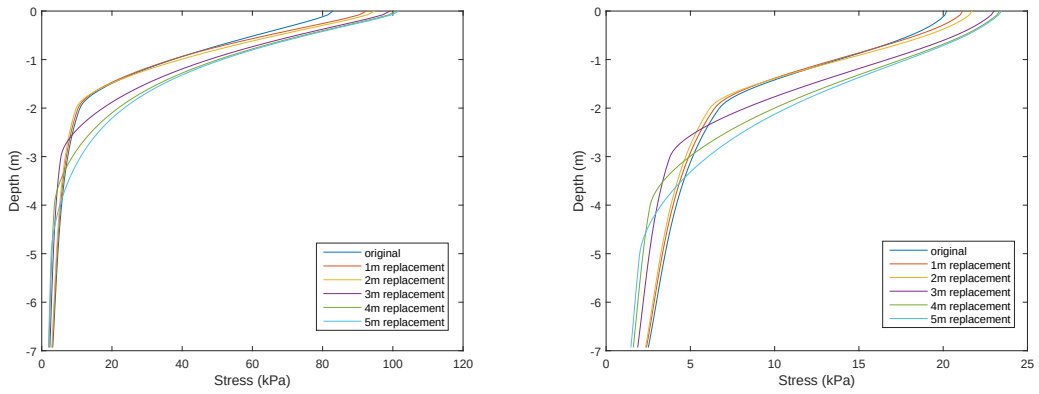

(a) (b)

Fig. 3.26 Vertical stress vs Depth for Soil case 3. (a) Ballasted track; (b) Slab track

3.5 Discussion

When planning, designing and constructing a new railway line it is important to assess the track-soil dynamics along the route. If the operational train speed is greater than 50% of the combined track-soil wave speed then there is the potential for dynamic effects to cause excessive track deflections. To mitigate this risk, at the planning stage, a scoping exercise can be performed to approximate the absolute critical velocity. This can be done for example using dispersion curve analysis based upon historical geotechnical data or surface wave testing data. If the train speed is found to be greater than 50% of the critical velocity then the TLM model can be used to perform a more detailed assessment (i.e. calculation of track-ground DAF curves).

Finally, if soil replacement is deemed necessary then the presented model can be combined with a costing tool to optimise the depth of remediation required, with respect to price.

Lastly, it should be noted that the aforementioned analysis assumes linear soil behaviour. As train speeds approach the critical velocity, strain levels within the soil can move to the high strain range (Alves Costa et al. [4]). This results in a non-linear relationship between strain and stiffness. The thin-layer method approach used within the model is well suited to the simulation of these effects. This is presented in the following chapter.

3.6 Conclusion

Soil replacement or improvement is commonly used on new railway lines to increase track stiffness, however is expensive. Therefore a model is developed for rapidly assessing the effect of different soil improvement depths and stiffness' on track behaviour. The model can therefore be used to optimise soil replacement with respect to construction cost. The modelling methodology is comprised of a thin-layer method ground model, coupled in the wavenumber-frequency domain to an analytical track model. It is capable of simulating the deep wave propagation that occurs when approaching critical velocity. Validation is performed using a combination of field experimental data and published numerical results, and the model is found to have strong accuracy. To show the model capabilities, three earthwork situations are considered: a homogenous soft soil, a soft soil over a stiff soil, and a stiff embankment resting on a soft soil over a stiff soil. It was found that due to the complex nature of the 3D wave propagation and its dependency on multiple variables, the relationship between improvement depth and rail displacement can be highly non-linear. Therefore soil improvement must be designed carefully to achieve the desired track performance.

In the next chapter, a non-linear TLM approach will be proposed to look into the soil non-linearity effect. It is built upon the linear approach described in this chapter and is computed in an iterative 'layer-by-layer' manner to model the non-linearity of soil.

Chapter 4

Non-linear subgrade behaviour

4.1 Introduction

Increases to operational train speed mean that it is more likely vehicles will induce dynamic effects within the supporting track and soil structure. In certain cases the critical velocity has been measured to be as low as 65 m/s (Madshus and Kaynia [128], Kaynia et al. [100]). This is significantly below the operational speed of typical high speed lines/trains (85m/s), and if large track displacements are induced, the track will degrade quickly and hence will require frequent maintenance.

A challenge with the majority of analytical and numerical approaches proposed for railway track modelling is the assumption of linear elastic material behaviour. However, when the train speed is high, large strains are often induced in the soil, thus causing non-linear stiffness and damping behaviour (Shih et al. [157], Alves Costa et al. [3], Kaynia et al. [100]). This results in quite different track behaviour (i.e. deflection) compared to the case in which non-linearity is not accounted for.

This chapter discusses an iterative 'linear equivalent' procedure that uses strain magnitude and degradation curve data to automatically adjust material stiffness and damping based upon strain levels. It accounts for the material (soil) non-linearity by updating the material properties iteratively until the convergence occurs. Similar to the linear thin-layer element model described in Chapter 3, the track is modelled analytically and the soil is modelled semi-discretely using the thin-layer element method in the wavenumber-frequency domain. The track-ground models are coupled and the overall model is computed in an iterative (thin) 'layer-by-layer' manner to include the effects of soil non-linearity. This greatly reduces the computational

time, and due to the very thin nature of elements used in the thin-layer method, stiffness changes due to non-linearity can be simulated with much finer granularity compared to the work of Shih et al. [157]. The illustration for the model is given in Fig 4.1.

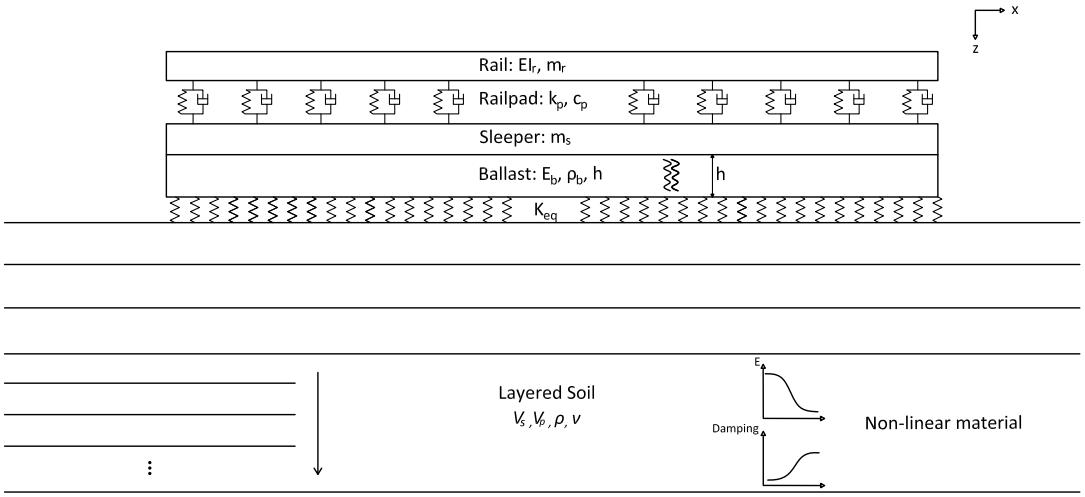

Fig. 4.1 Schematic illustration of the analytical track model coupled with non-linear TLM ground model

This chapter contains six sections. Section 4.2 introduces the concept of the proposed 'linear equivalent' model to include soil non-linearity effect. It is followed by the validations against published dataset and also well-known Ledsgard in-situ field data, detailed in Section 4.3. Subsequently, four case studies are used to investigate the non-linear behaviour, each with contrasting subgrade characteristics. The numerical results and analysis are shown in Section 4.4. A brief discussion on the findings and results is recorded in Section 4.5. In addition, Section 4.6 gives a comparison between linear and non-linear model, which is followed by a conclusion of the work in Section 4.7.

4.2 Equivalent linear model

4.2.1 Brief introduction

The track-ground system is modelled using a sub-structuring approach (Dong et al. [49], Dong et al. [48] and Dong et al. [50]). An analytical model is used to calculate the track response, while the thin-layer element method is used to compute the soil response. They are then coupled taking into account the compatibility of displacements and equilibrium of loads in the vertical direction (thus implying relaxed boundary conditions used by Steenbergen and Metrikine [158]). Non-linearity is adopted in the soil response using an 'equivalent

linear' methodology. Although the model is by definition 'linear equivalent', the term 'non-linear' is also used interchangeably to denote the same meaning.

The track is modelled in the wavenumber-frequency domain as described in the works of Alves Costa [1], Alves Costa et al. [5], Dong et al. [49], Dong et al. [48], Dong et al. [50] and Mezher et al. [133]. The formulations and derivations are detailed in the Chapter 3. For the soil model, the stresses, strains and displacements within the 3D soil stratum are computed using the thin-layer method. To do so, the domain is discretised into a series of thin horizontal layers. Three nodes are used for each element (thin-layer) and the analytical wave equation is used to compute the response in both horizontal directions. The problem is solved in the frequency-wavenumber domain, using eight thin-layers per wavelength to ensure accuracy (Dong et al. [50]). Until this step, the methodology is the same as what has been adopted in the linear Thin-Layer Model, which is explained comprehensively in Chapter 3.

4.2.2 Equivalent linear formulation

When the soil is subject to small strains, the stresses and strains are directly proportional, meaning the soil response can be considered linear and elastic (i.e. G_{max} in Figure 4.2). However, as the strains increase, this relationship becomes non-linear causing soil stiffness to decrease, and damping to increase with strain. Figure 5 shows this typical stress-strain relationship where the stiffness is defined by the gradient of the solid black line and damping by the grey-shaded loop area. Secant and tangent stiffness formulations can be used to describe this behaviour, however the linear equivalent approach requires secant stiffness to be used.

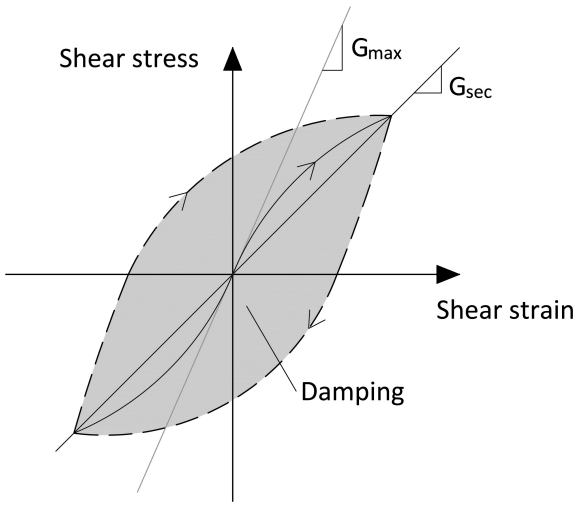

Fig. 4.2 Strain-stress path during cyclic loading

To assess non-linear behaviour, a 'linear equivalent' approach is used. The advantage of using this approach is that it can be used with frequency domain approaches to reduce the computational demand in comparison to constitutive time domain models. By definition, it means that while the analysis remains linear, the soil properties are updated as function of the strain level, thus simulating non-linear type effects. It requires for the linear system of equations to be computed, the strain levels assessed, the stiffness adjusted and the process repeated until convergence. It is implemented element-by-element (i.e. layer-by-layer) with the TLM formulation as follows:

1. Assume low strain properties for all thin-layer elements (i.e. G_{max} or G_0)
2. Compute strain time histories and effective octahedral shear strain within all elements using Equation 4.1
3. Use stiffness-strain relationship curves which are functions of confining stress and plasticity index, to update the stiffness within each element (Figure 4.7a)
4. Use damping-strain relationship curves which are functions of confining stress and plasticity index, to update the damping within each element (Figure 4.7b)
5. If the lower soil layer is unbounded (i.e. infinite depth with no bedrock), update the absorbing layer to have identical properties to the deepest thin-layer element
6. Repeat steps 2 – 5 until the differences between shear modulus and damping of the central node in two consecutive iterations fall below a pre-defined tolerance (i.e. 3% tolerance between iterations, as suggested by Alves Costa et al. [3])

Plasticity index is typically determined using laboratory tests and effective octahedral strain is calculated as:

$$\gamma_{oct} = \alpha \frac{1}{3} \sqrt{(\varepsilon_{xx} - \varepsilon_{yy})^2 + (\varepsilon_{xx} - \varepsilon_{zz})^2 + (\varepsilon_{yy} - \varepsilon_{zz})^2 + 6(\gamma_{xy}^2 + \gamma_{xz}^2 + \gamma_{yz}^2)} \tag{4.1}$$

Where ε_{xx}, ε_{yy} and ε_{zz} are the strains in the three coordinate directions while γ_{xy}, γ_{xz} and γ_{yz} are the shear strains. These are calculated for all layers using Equation 3.22. α is a constant chosen as 0.65 in-line with other linear equivalent formulations (Yoshida et al. [184]).

4.3 Model validation

4.3.1 Soil stress validation

The linear equivalent formulation relies on the accurate calculation of stress and strain levels within the full depth of the soil layer. To show that the model is capable of computing these, results are compared against approximate values from the work of Chen et al. [32]. The benchmark problem consists of an Euler beam resting on a homogenous half-space, traversed by a 160kN moving vertical load at 30m/s (see Figure 4.3). The beam is 4m wide, 0.3m thick and infinite in the direction of vehicle travel. Stresses are monitored at 2m directly below the soil surface, at the central line of the Euler beam. To simulate the problem, the beam is modelled analytically and the soil is modelled using the thin-layer method, with the equivalent stiffness computed as shown in the slab formulation (Equation 3.2). The material properties used for this simulation are shown in Table 4.1.

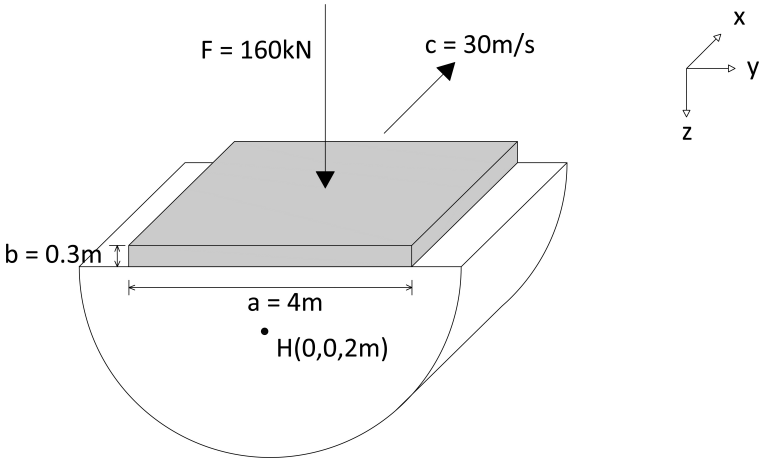

Fig. 4.3 Schematic diagram of Chen's validation model

Table 4.1 Properties of the beam and the ground for Chen's validation

Beam			
Density (kg/m^3)	1900	Young's modulus (MPa)	30000
Width (m)	4	Thickness (m)	0.3
Mass (kg)	2280	Second moment of area (m^4)	0.009
Ground			
Density (kg/m^3)	1800	Young's modulus (MPa)	29
Poisson ratio	0.45	Shear wave speed (m/s)	74.54

Figure 4.4 shows a comparison of stress time histories between the published results and the results of the new TLM model. Four stress components are shown (σ_{xx}, σ_{yy}, σ_{zz} and τ_{xz}) because two of the shear stress components are zero (τ_{xy} and τ_{yz}). Strong agreement is seen between results with respect to both shape and magnitude. It should be noted that although this example validates stresses, the TLM formulation uses strain levels directly to compute stress levels, thus by default, also confirming the accuracy of strain levels. Therefore it can be concluded that the stress-strain computations within the soil model are accurate.

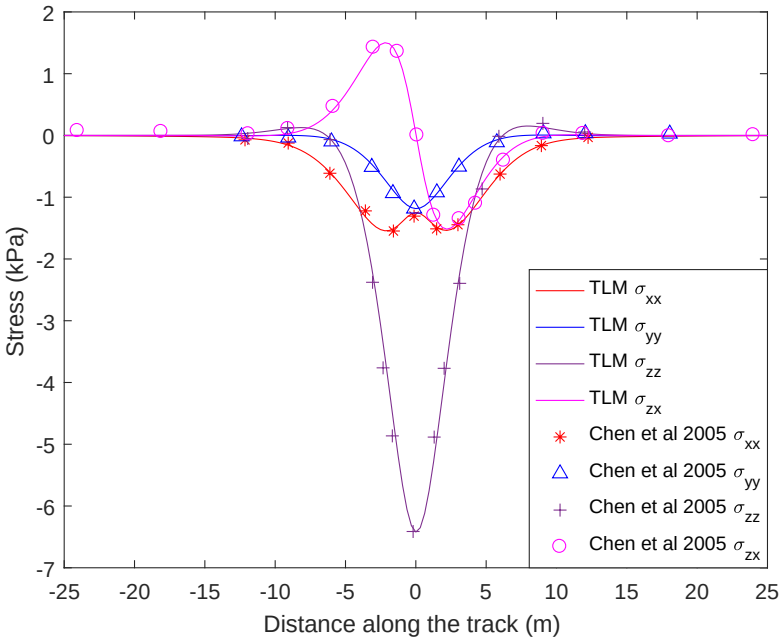

Fig. 4.4 Comparisons of the dynamic stresses of an element at (0, 0, -2m) underneath the moving load

4.3.2 Experimental validation

The second validation is for field data recorded at Ledsgard, Sweden. This site was subject to large rail deflections and suspected high soil non-linearity during the passage of X2000 trains shortly after opening. This occurred because the track was constructed over soft ground, with a sandwiched layer of extremely soft organic clay (Figure 4.5). Therefore it has been used for a variety of numerical model validations (e.g. Madshus and Kaynia [128], Alves Costa et al. [3], Shih et al. [157]).

The track is ballasted with the properties shown in Table 4.2, and rests on a 1.2m high embankment. The train is an X2000 with 5 carriages and 20 axle loads (Figure 4.6). Wheel-rail irregularities are not considered due to their minor influence on low-frequency dynamic track amplification. Also, it should be noted that although for the linear case the response of a single wheel can be used (i.e. via superposition) to compute the

response of an entire train, this is not possible when considering soil non-linearity. Instead, for each run, the unique combination of train wheels is computed.

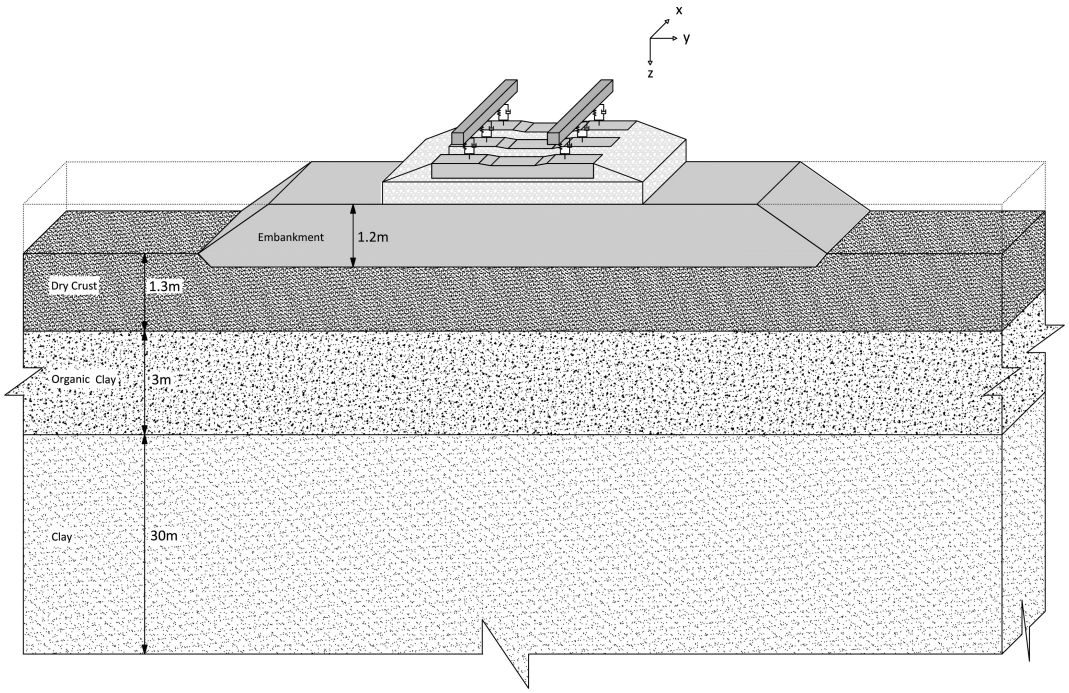

Fig. 4.5 Geometric dimensions at the Ledsgard site

Table 4.2 Track parameters at the Ledsgard site

Rail	
Mass per unit length (kg/m)	120
Young's modulus (MN/m^2)	210×10^3
Second moment of inertia (m^4)	6.11×10^{-5}
Railpad	
Stiffness per unit length (MN/m^2)	350
Damping per unit length (kNs/m^2)	30
Sleeper	
Mass per unit length (kg/m)	490
Ballast	
Density per unit length (kg/m^3)	1200
Thickness (m)	0.35
Young's modulus per unit length (MN/m^2)	315
Compression wave speed in ballast (m/s)	786

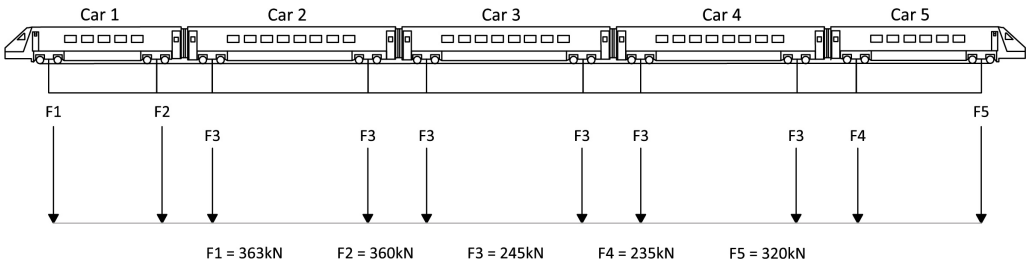

Fig. 4.6 Geometric and mechanical properties of the X2000 train

The soil properties at the site are shown in Table 4.3. All soil layers have a shear wave speed significantly lower than the engineered embankment, and the soil stratum is supported by bedrock at a depth of 30m. To model soil non-linearity, example shear modulus and damping ratio curves are shown in Figure 4.7, based upon triaxial tests performed on Ledsgard soil samples by Alves Costa et al. [3].

The shear modulus reduction curve formulations proposed by Ishibashi and Zhang [87] require cyclic shear strain amplitude (γ_{oct} in this case), Plasticity Index PI (I_p) and effective confining pressure ($\bar{\sigma}_m$) as inputs. The shear modulus reduction is written as:

$$\frac{G}{G_{max}} = K(\gamma_{oct}, I_p)\bar{\sigma}_m^{n(\gamma_{oct},I_p)-n_0} \tag{4.2}$$

When the shear strain is smaller than 10^{-6}, i.e., the soil response can be considered as linear and elastic,

$$K(\gamma_{oct}, I_p) = 1 \tag{4.3}$$

$$n(\gamma_{oct}, I_p) - n_0 = 0 \tag{4.4}$$

For shear strains that are larger than 10^{-6}, i.e., the soil non-linearity shall be taken into acount,

$$K(\gamma_{oct}, I_p) = 0.5\{1 + \tanh[\ln(\frac{0.000102 + q(I_p)}{\gamma_{oct}})^{0.492}]\} \tag{4.5}$$

$$n(\gamma_{oct}, I_p) - n_0 = 0.272\{1 - \tanh[\ln(\frac{0.000556}{\gamma_{oct}})^{0.4}]\}e^{-0.0145I_p^{1.3}} \tag{4.6}$$

Where

$$q(I_p) = \begin{cases} 0.0, & \text{for } I_p = 0 \text{ (sandy soils)} \\ 3.37 \times 10^{-6} I_p^{1.404}, & \text{for } 0 < I_p \leqslant 15 \text{ (low plastic soils)} \\ 7.0 \times 10^{-7} I_p^{1.976}, & \text{for } 15 < I_p \leqslant 70 \text{ (medium plastic soils)} \\ 2.7 \times 10^{-5} I_p^{1.115}, & \text{for } I_p > 70 \text{ (high plastic soils)} \end{cases} \tag{4.7}$$

Similary, the damping ratio can be expressed as a function of G/G_{max} and is accordingly fitted by the Equation 4.8:

$$D = D_{sand} \times A(I_p) \tag{4.8}$$

Where D_{sand} is the damping ratio fit for sands and $A(I_p)$ represents a modification function for damping ratio applied to D_{sand} to satisfy the continuity of material properties from sands to clay. The mathematical formulas for D_{sand} and $A(I_p)$ are shown in the Equation 4.9:

$$\begin{cases} D_{sand} = 0.333\{0.586(\frac{G}{G_{max}})^2 - 1.547(\frac{G}{G_{max}}) + 1\} \\ A(I_p) = \frac{1+e^{-0.0145I_p^{1.3}}}{2} \end{cases} \tag{4.9}$$

Therefore Alves Costa et al. [3] computed $\bar{\sigma}_m$ at the centre of each physical soil layer, however in this work, these values are computed at the centre of each individual thin layer. This results in a much larger number (one per thin-layer element) of individual curves than the 4 examples shown in Figure 4.7.

Table 4.3 Velocity and direction of the compared simulation cases

	Thickness (m)	P-wave speed (m/s)	S-wave speed (m/s)	Density (kg/m^3)	Damping ratio
Embankment	1.2	340	210	1800	0.04
Dry crust	1.1	500	65	1500	0.04
Organic clay	3	500	40	1250	0.02
Clay	30	1500	87	1475	0.05

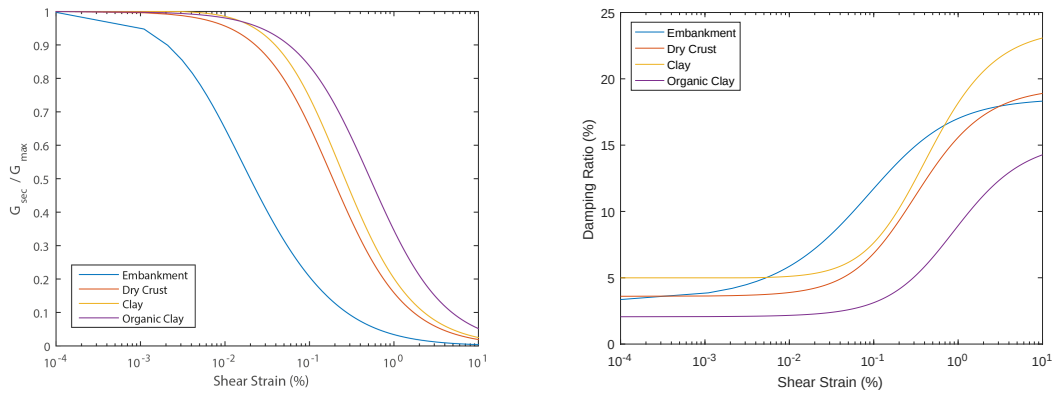

(a) (b)

Fig. 4.7 (a) Shear modulus reduction curves; (b) Damping ratio for different soil layers at Ledsgard (Alves Costa et al. [3])

Figure 4.8a, Figure 4.8b and Figure 4.8c compare the proposed model results with the field data for speeds of 70km/h, 140km/h and 180km/h, respectively. For speeds of 70 km/h and 140 km/h, the TLM model shows a match with the field data. For the higher speed of 180 km/h, there are a few small discrepancies, however overall a strong agreement in terms of shape and magnitude is found.

Figure 4.8d compares the peak upward and downward rail deflections for the equivalent linear and linear simulation results. The positive values designate upward displacements and the negative values represent downward displacements.

At low speed the linear and equivalent linear simulations show a close match to each-other. However, as speed increases, the equivalent linear results show larger deflections because the equivalent linear soil is less stiff in the presence of high strains, thus facilitating higher displacements. When compared to the field data, the equivalent linear results are a closer match, with the linear case significantly underestimating maximum upward and downward deflections. This is particularly true as train speed approaches the critical velocity. For example, the maximum downward displacement at a speed of 180 km/h for the field data is 12.7mm. This is close to the equivalent linear predicted result of 13.3mm, but quite different to the linear value of 9.2mm. Therefore it can be concluded that the use of a non-linear formulation is necessary to accurately compute the track response.

Figure 4.9a shows the degradation of the embankment surface shear modulus during the equivalent linear analysis. It is seen that it reduces by 38% after the 1st iteration, and after the convergence criteria has been met, it is only 46% of the original low-strain value. Further, Figure 4.9b shows the Young's modulus versus depth for speeds of 70km/h and 204km/h. It can be seen that the reduction of embankment stiffness is approximately 50%, which matches with the result shown in Figure 4.9a. Also there is a large change to the Young's modulus in the top 2 soil layers (dry crust and organic clay layer). This indicates that they are undergoing high strains and their stiffness is degrading significantly as train speed increases. In contrast, as depth increases, strain levels decrease and train speed has little effect on Young's modulus.

Figure 4.10 shows the maximum octahedral shear strain versus depth for train speeds of 70km/h and 204km/h. It compares the linear and non-linear formulations, and also shows results published in [38], which were obtained using a comprehensive 3D constitutive model. The strain levels are low in the embankment due to its high stiffness but again the strains are large in the top 2 soil layers. As found previously, the strain levels are larger for the equivalent linear model compared to the linear model, particularly towards the soil surface.

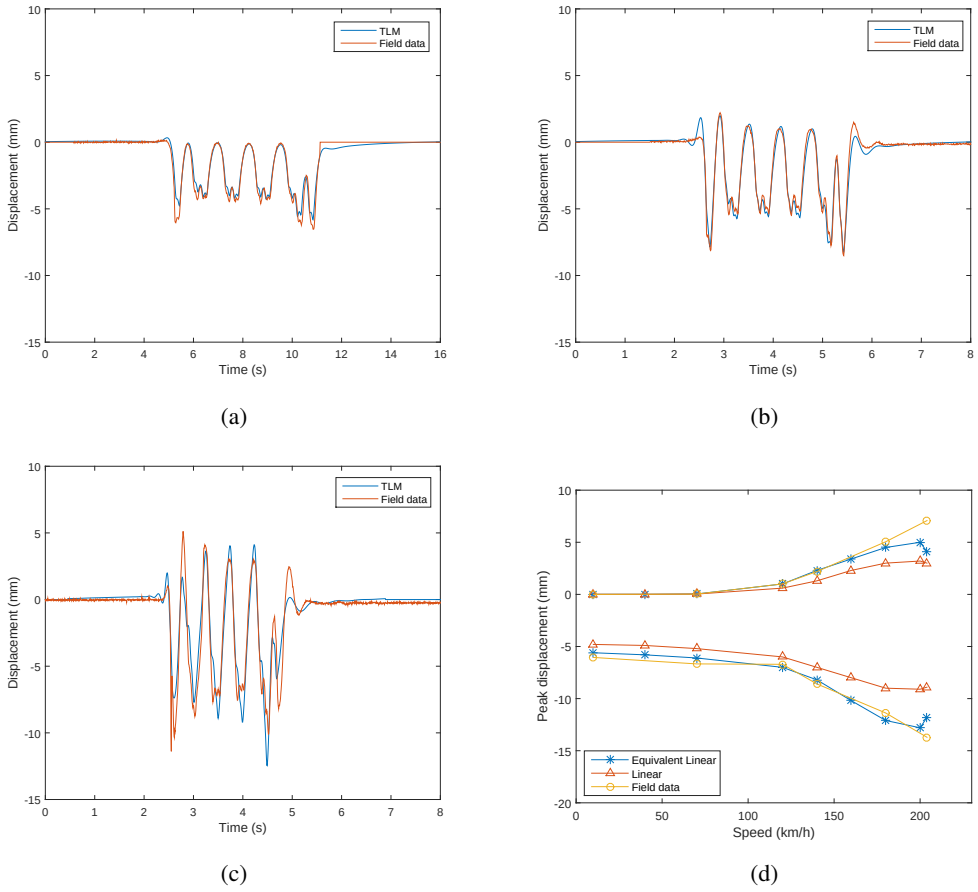

Fig. 4.8 Measured and simulated time histories of track displacements for different train speeds: (a) c=70km/h; (b) c=140km/h; (c) c=180km/h; (d) Peak displacements versus train speeds (Southbound)

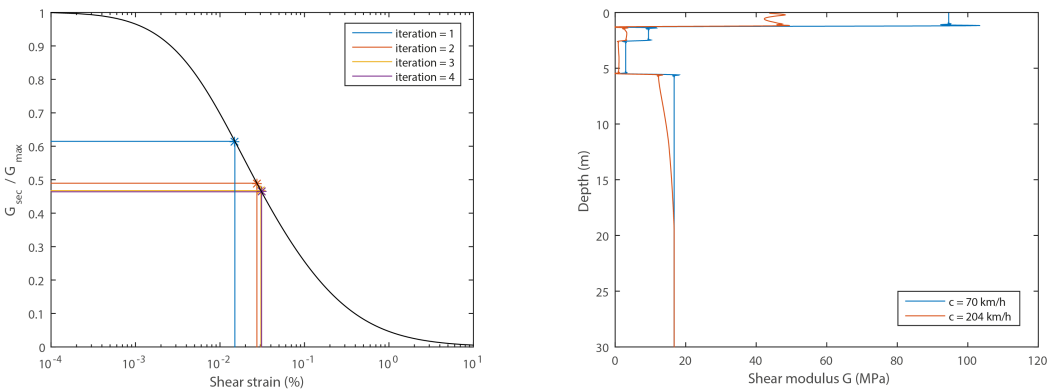

Fig. 4.9 (a) Embankment shear modulus reduction process at each iteration step at speed of 204km/h; (b) Young's modulus comparison over the depth for speeds of 70km/h and 204km/h

Comparing model results against Shih et al. [157], it is seen that strain levels are of similar magnitude. There are some discrepancies in the embankment and also towards the top of the clay layer. The discrepancy in the clay layer shows the strain levels in Shih et al. [157] decreasing more slowly than that in the TLM

model. This may be due to the different element sizes used in the different models – the TLM utilises much thinner elements, thus allowing non-linear effects to be captured more precisely. Furthermore, qualitatively comparing strains with depth against the contours presented in Alves Costa et al. [3], in which an equivalent linear approach is applied on the basis of element-by-element strategy instead, strain levels are shown to decrease rapidly in-line with the TLM results.

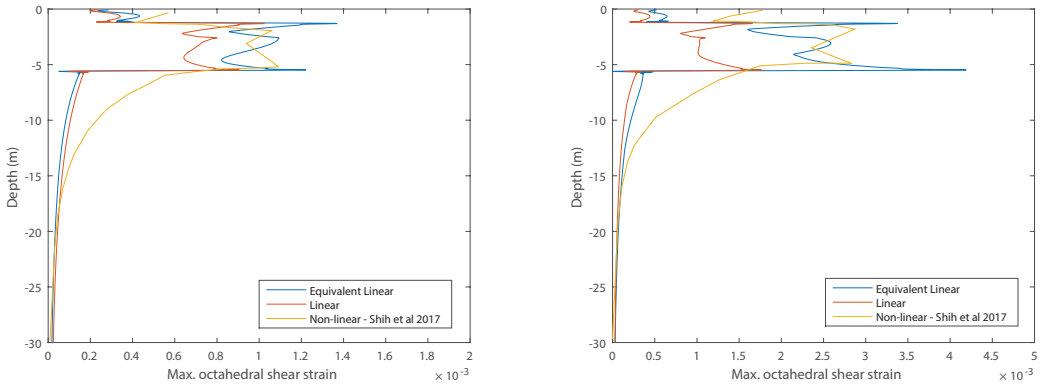

Fig. 4.10 Variation of maximum octahedral shear strain with depth for train speed at (a) 70km/h; (b) 204km/h

4.4 Numerical analysis

As shown via the validation case, at high speed, railway lines can induce elevated subgrade strains which can result in non-linear soil behaviour. Therefore four soil case studies are undertaken, with properties shown in Table 4.4 and Figure 4.11, to investigate the effect of different soil stiffness's and layering combinations on track response. To account for non-linear effect, the shear modulus degradation and damping ratio curves are based on the functions proposed by Ishibashi and Zhang [87]. Effective confining stress and plasticity index are governing factors that affect the non-linearity soil behaviour. In this study, the plasticity index is assumed to be 30 for all soils. In Figure 4.11, the corresponding primary wave speed C_p and secondary wave speed C_s of each soil layer are listed and two points (A and B), indicating upper and lower position of soil, are selected for each soil case for the strain analysis. The cases are:

1. A homogeneous low stiffness soil
2. A low stiffness soil overlying a stiffer soil
3. A high stiffness soil overlaying a softer soil

4. A homogeneous high stiffness soil

For all cases, the train is modelled as a moving 18 tonne axle load. A large number of train speeds are considered, as needed to plot dynamic amplification curves. Regarding the track, it is a ballasted track with properties shown in Table 4.5. The properties used are from the common ballasted railway data used in other researches (Alves Costa et al. [5] and Santos et al. [149]). A variety of output variables are plotted, however for dynamic amplification curves it should be noted that non-linear dynamic amplification is very sensitive to wheel spacing and therefore can change dramatically depending upon vehicle configuration.

Table 4.4 Soil properties used in the case studies

	Layer thickness (m)	Young's modulus (MPa)	Poisson's ratio	Density (kg/m^3)	Damping ratio
Soil 1	∞	45	0.35	1800	0.03
Soil 2	[2; ∞]	[45; 120]	[0.35; 0.35]	[1800; 1800]	[0.03; 0.03]
Soil 3	[2; ∞]	[100; 45]	[0.35; 0.35]	[1800; 1800]	[0.03; 0.03]
Soil 4	∞	200	0.35	1800	0.03

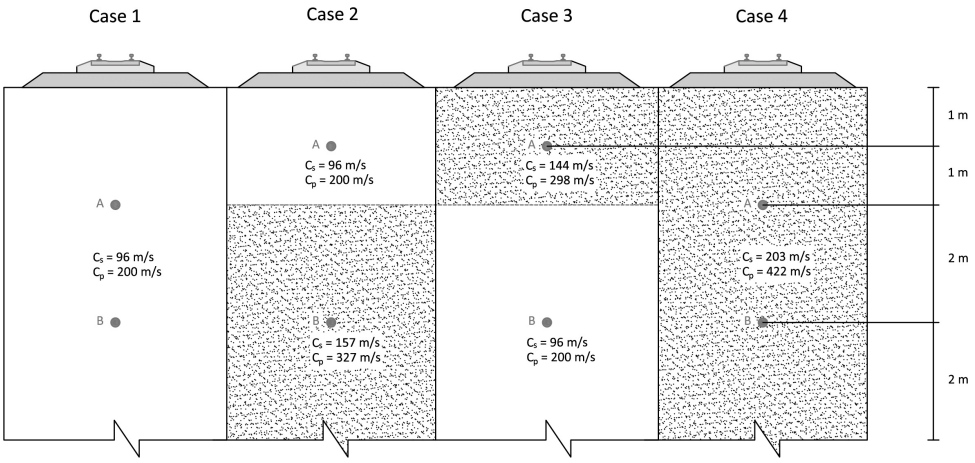

Fig. 4.11 Wave speeds demonstration for different soil conditions

Table 4.5 Ballasted track properties

Ballasted track		
Rail	EI_r (Nm^2)	1.26×10^7
	m_r (kg/m)	120
Railpad	k_p (N/m)	5.5×10^8
	c_p (Ns/m)	2.5×10^5
Sleepers	m_s (kg/m)	490
Ballast	$E_{ballast}$ (MPa)	150
	$h_{ballast}$ (m)	0.35
	2b (m)	2.5
	ρ (kg/m^3)	1600

4.4.1 Soil case 1

Soil 1 is a homogeneous half-space with a Young modulus of 45MPa. Figure 4.12 shows the relationship between train speeds for four variables: a) rail displacement, b) ballast velocity, c) strain at 2m depth (Point A in Figure 4.11), and d) strain at 4m depth (Point B in Figure 4.11). The linear and non-linear results are compared for each, considering the passage of a single wheel. It should however be noted that for the non-linear case, the results are highly sensitive to wheel spacing and should be treated as indicative.

Firstly, considering rail displacements, the non-linear and linear curves have a similar shape. The linear case has lower displacements for the majority of speeds, except around its critical velocity peak at 90m/s. Regarding maximum dynamic amplification, the non-linear case shows 24.6% greater displacements compared to the linear case. Further, the critical velocity reduces from 91 m/s to 80 m/s. These effects occur because the soil stiffness is reduced for the equivalent linear case. This causes the track to deflect more, but also lowers the wave propagation velocities, thus affecting the dispersive characteristics of the soil.

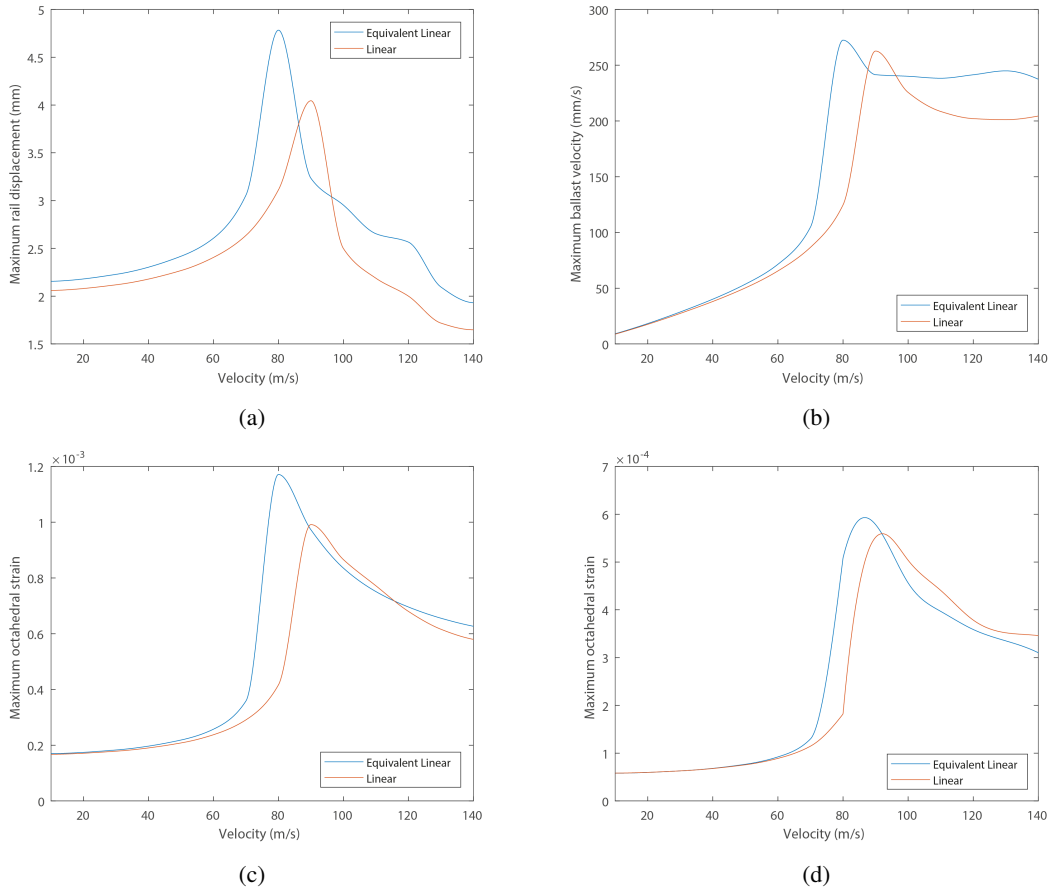

Fig. 4.12 Soil case 1 comparisons of linear and equivalent non-linear DAF curves of (a) rail displacements (b) ballast velocity (c) octahedral strain at Point A (d) octahedral strain at Point B

Analysing the octahedral strains at 2m and 4m below the ground surface shows a maximum at 91m/s, approximately the shear wave speed (and thus the critical velocity) of the linear soil case. However, for the non-linear case at 2m, the peak displacement magnitude increases by 20.8%, and the critical velocity shifts to 80 m/s which is 12.1% lower than the linear case. In comparison, at 4m the peak displacement magnitude increases by 10.1%, and the critical velocity shifts to 85 m/s which is 6.6% lower than the linear case. The effect at 2m is therefore more pronounced than at 4m and due to greater soil non-linearity close to the soil surface. This is further illustrated in Figure 4.13 which shows strain versus depth, for a low speed (10m/s) and the non-linear critical speed (80m/s). At a depth of 2m, strain levels are significantly higher than at 4m (2.4×10^{-4} vs 1.13×10^{-3}). Further, if a depth of 1m is considered, increasing the train speed results in a 387% increase in strain level.

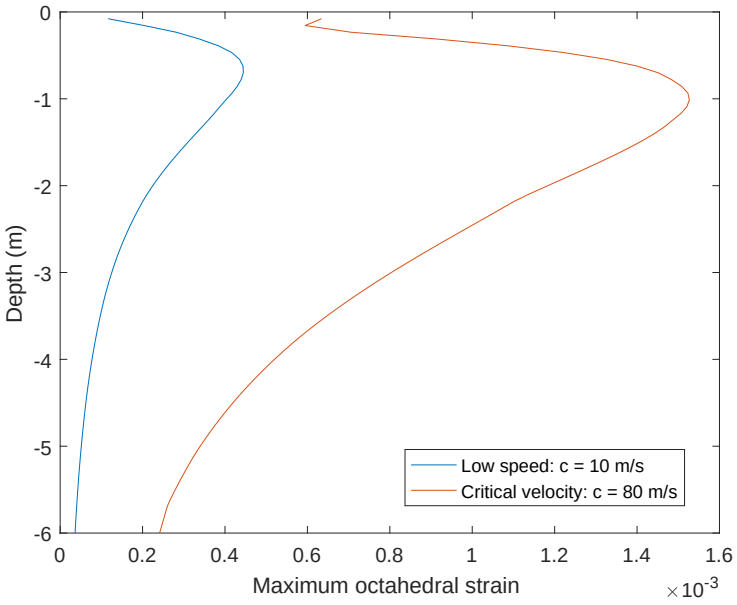

Fig. 4.13 Maximum octahedral strain vs depth for c = 10 m/s and c = 80 m/s for non-linear Soil case 1

Figure 4.14 shows the stress histories of the (non-linear) soil formulation at 2m depth (Point A), directly below the track for 3 speeds. At low speed, the stress history has a symmetrical shape and the magnitude of each stress component is small. However, as train speed increases, this symmetry is lost and all stress component magnitudes increase significantly. The change in magnitude is summarised in Table 4.6, where it is seen that higher speeds cause the horizontal stress component to increase as a proportion of the vertical stress. Therefore, although the vertical stress component increases with speed, when approaching the critical velocity, the horizontal components increase more rapidly. After experiencing a peak at 80m/s, all stress components stabilise and only experience small additional increases. This is also shown in Figure 4.15 which shows the effect of speed on peak-peak stress components when considering soil non-linearity. In this figure it is seen that as train speed increases the discrepancy between vertical and horizontal stresses decreases.

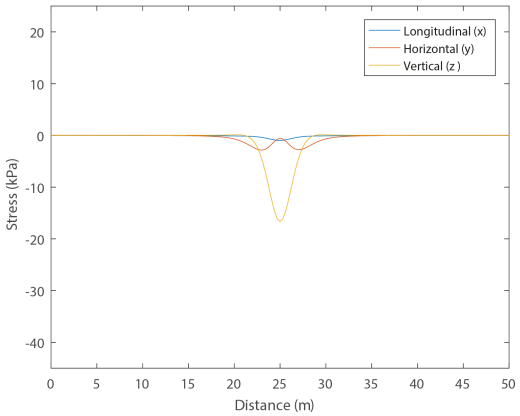

(a)

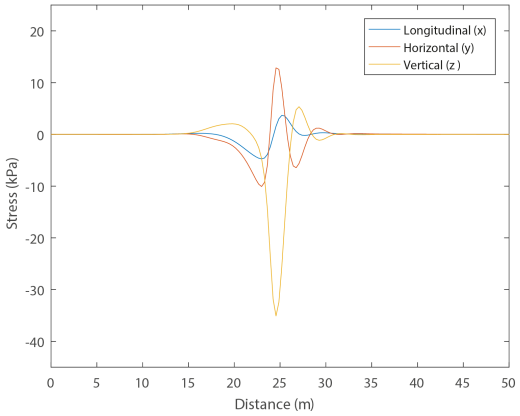

(b)

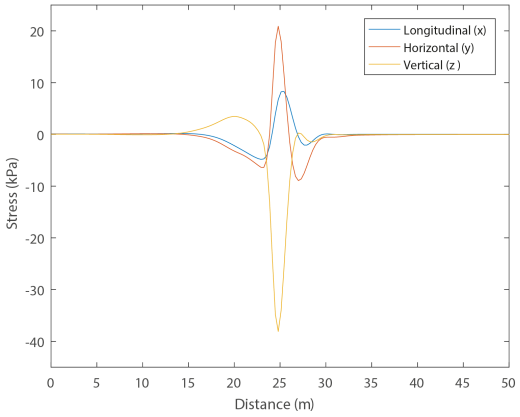

(c)

Fig. 4.14 Stress history of Point A underneath the centre line of the track structure at the speeds of (a) c = 10m/s (b) c = 80m/s (c) c = 130m/s

Table 4.6 The magnitude of maximum stress components (peak-to-peak) at various speeds

	c = 10m/s		c = 80m/s		c = 130m/s	
	Magnitude	Percentage	Magnitude	Percentage	Magnitude	Percentage
Vertical stress (kPa)	16.8	–	40.8	–	41.3	–
Horizontal stress (kPa)	2.8	16.7%	23.4	57.3%	30.1	72.8%
Longitudinal stress (kPa)	1.1	6.5%	9.1	22.3%	13.1	31.7%

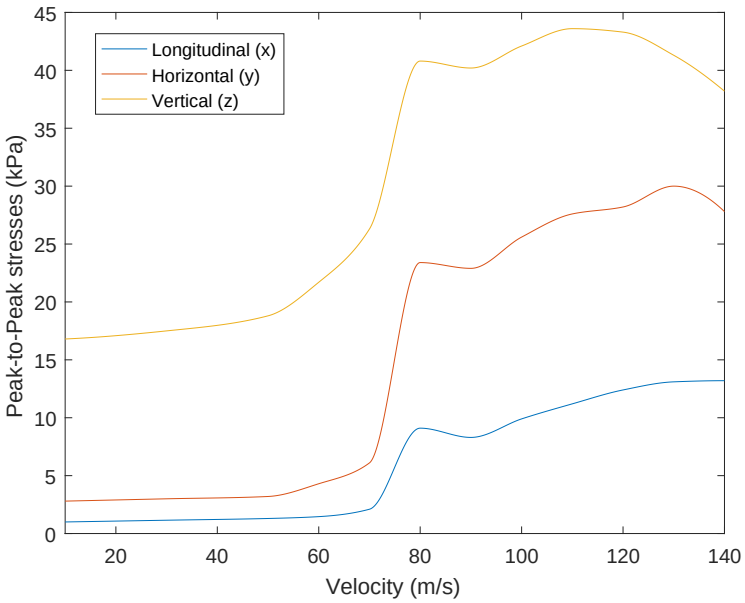

Fig. 4.15 DAF curves for stress components (peak-to-peak) at Point A in Soil case 1

4.4.2 Soil case 2

Soil Case 2 consists of a 2m thick soft layer (45 MPa) overlying a stiffer homogenous half-space (120 MPa). Figure 4.16a shows that the maximum rail displacement increases by 29.5%, from 2.95 mm to 3.82 mm, when considering soil stiffness degradation. In a similar manner to Soil Case 1, this is because the equivalent linear model results in decreased soil stiffness, therefore causing greater track deflections. However, in contrast to Case 1, track deflections are lower for the linear case for most of the train speeds, even at the linear critical speed.

Similarly, the critical speed shifts to 90 m/s, for the non-linear case, which represents a 20.0% decrease. This is due to the reduced wave speeds associated with the degraded soil stiffness. Additionally, the velocity-displacement gradient is very steep for the non-linear case immediately prior to critical velocity. This

indicates that very minor changes to speed can almost double rail deflections. At speeds greater than the critical velocity, displacements reduce rapidly, to magnitudes even lower than the static load case. This is true for both the linear and non-linear case.

Figure 4.16b shows the relationship between strain and soil depth for speeds of 10 m/s and 90 m/s, which represent the quasi-static case and also the non-linear critical velocity case. The black dotted line indicates the soft-stiff soil interface. The higher speed shows significantly larger strains compared to the low speed case, particularly in the top 2m where the softer soil is located. At the interface between the soft and stiff soils, there is a rapid reduction in strain levels for both speeds, however this is particularly pronounced for the higher speed. At the stiffer soil locations the strains remain higher for the non-linear case, however the values are lower than in the soft soil layer, and converge rapidly until a depth of approximately 6m.

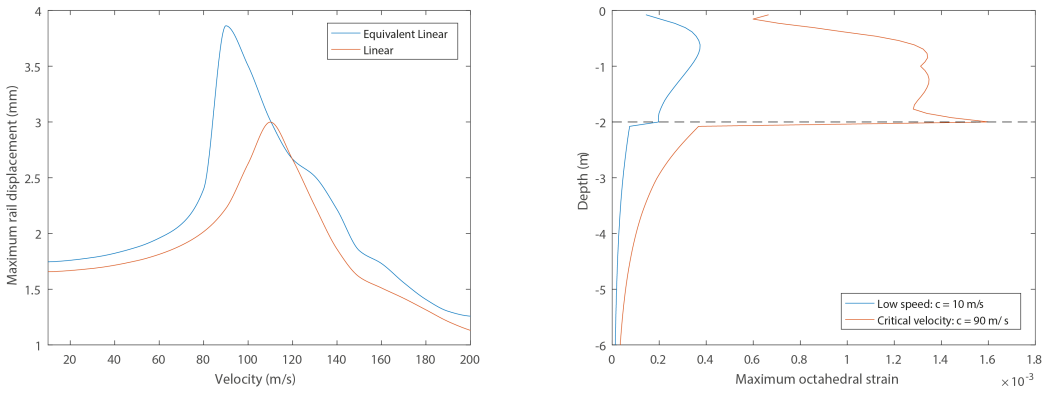

(a) (b)

Fig. 4.16 Soil case 2, (a) comparisons of linear and non-linear DAF rail displacement curves, (b) Maximum (non-linear) shear strain vs depth for c = 10 m/s and c = 90 m/s

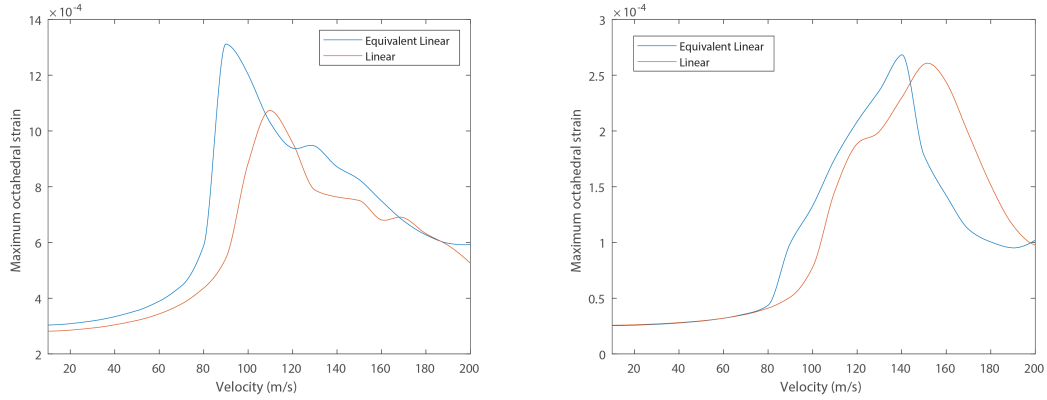

(a) (b)

Fig. 4.17 Soil case 2 comparisons of linear and non-linear DAF curves of maximum octahedral strain (a) at Point A (b) at Point B

Figure 4.17 compares octahedral strain dynamic amplification curves for the linear and non-linear formulations, at depths of both 1m (Point A) and 4m (Point B) below the soil surface. The 1m location represents the centre of the soft layer, while the 4m location represents a depth 2m below the soft-stiff layer interface. Figure 4.17a shows that the peak strain of the linear result at 1m is located at 110 m/s, which is close to the linear track-ground critical velocity. Similarly, for the 4m case, the peak (low-strain) strains are found at 152m/s (shown in Figure 4.17b), corresponding to the shear wave velocity of the lower layer. Therefore the critical velocity is located between the speeds of peak strains in both layers. This is in contrast to Soil Case 1, where the critical velocity at all soil and track locations (in terms of either strain of displacement), is constant. This is because P-SV waves are non-dispersive for Soil Case 1, while in Soil Case 2 P-SV waves experience dispersion due to the presence of two contrasting stiffness soil layers.

Comparing the linear and non-linear cases, the maximum strain levels are elevated by 23.4% and 5.3% when non-linearity is considered, for the 1m and 4m locations, respectively. Further, the critical speeds are shifted by 18.2% and 10.7%, respectively. Interestingly, for the 1m case, for the majority of train speeds, the strains are higher for the non-linear case, however at 4m between speeds of 140-200m/s, the linear case shows higher displacements. Further, at low train speed, there is discrepancy between the linear and non-linear cases at 1m, however at a depth of 4m, below a speed of 70m/s, both formulations result in almost identical strain magnitudes. This is because strains reduce with depth, meaning the deeper soil locations are less susceptible to soil stiffness degradation.

Figure 4.18 shows the p-q stress paths at a depth of 1m below the track centre-line for speeds of 10, 90 and 110 m/s. The stress paths are computed using the mean stress increment (dp) and shear stress increment (dq):

$$dp = \frac{\Delta\sigma_1 + \Delta\sigma_2 + \Delta\sigma_3}{3} \tag{4.10}$$

$$dq = \sqrt{\frac{(\Delta\sigma_1 - \Delta\sigma_2)^2 + (\Delta\sigma_1 - \Delta\sigma_3)^2 + (\Delta\sigma_2 - \Delta\sigma_3)^2}{2}} \tag{4.11}$$

Where σ_1,σ_2 and σ_3 represent the principal stresses. At a speed of 10m/s, there is no sign of dynamic amplification. However, when the speed is 110 m/s, (i.e. close to the critical velocity), the stress state

becomes highly turbulent and the magnitudes increase significantly. This is consistent with the findings of Alves Costa et al. [6].

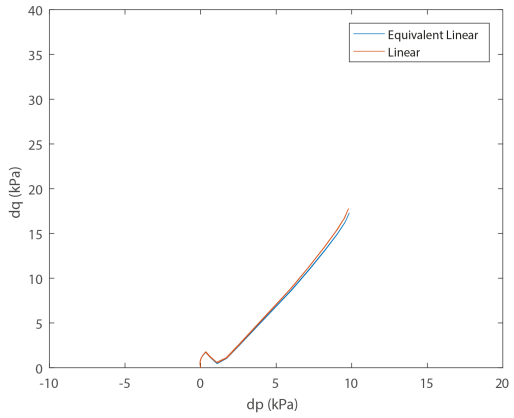

(a)

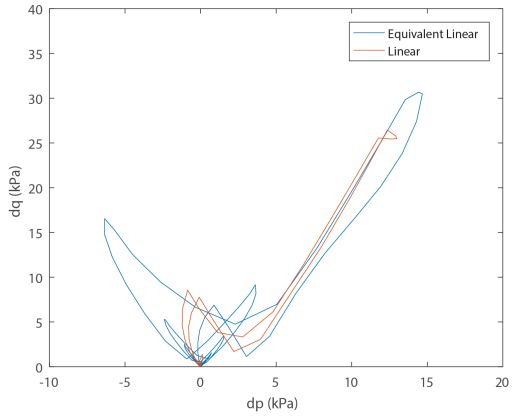

(b)

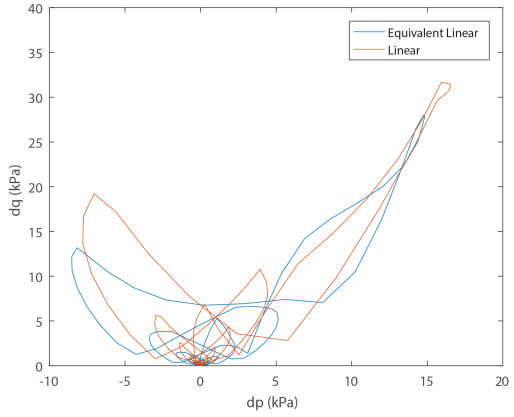

(c)

Fig. 4.18 Stress path followed at point A during the load passage with different speeds (a) c = 10 m/s (b) c = 90m/s (c) c = 110 m/s

4.4.3 Soil case 3

Soil Case 3 consists of a stiffer 2m layer (100MPa) overlying a softer lower layer (45MPa). It is therefore an inversely dispersive scenario, where phase velocities both increase and decrease depending upon frequency.

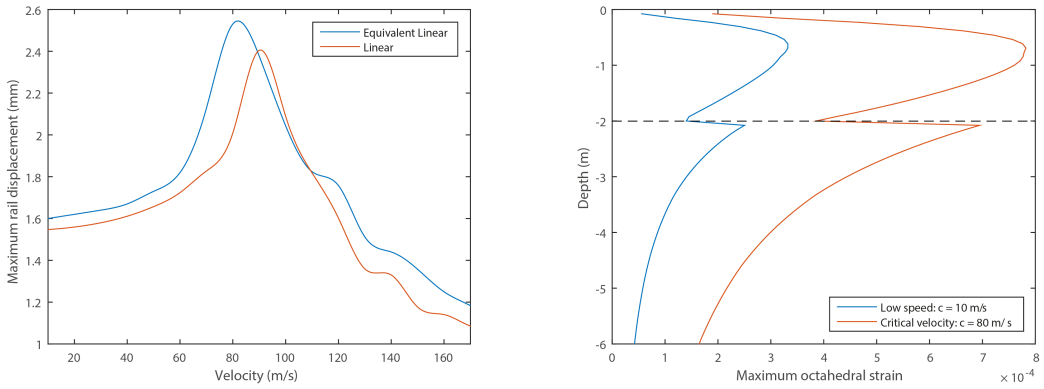

(a) (b)

Fig. 4.19 Soil case 3, (a) comparisons of linear and non-linear DAF rail displacement curves, (b) Maximum (non-linear) shear strain vs depth for c = 10 m/s and c = 80 m/s

Figure 4.19a shows the effect of moving speed on maximum rail displacement. The non-linear formulation results in a 7.2% increase in maximum displacement and 11.3% critical velocity decrease, respectively. These discrepancies are lower in magnitude compared to the previous soil case, and are due to the stiffer soil being located near the surface. This results in lower strain levels near the soil surface, and that decay less rapidly with depth. For example, for Soil Case 2, Figure 4.17 shows a maximum strain in the top 2m of 1.58×10^{-3}, and a maximum of 3.9×10^{-4} in the lower layer (i.e. 325% reduction). In contrast, for Soil Case 3, Figur 4.19b shows that the maximum strains in the upper and lower layers are 7.8×10^{-4} and 6.8×10^{-4} respectively, which is a 14.7% reduction. Therefore the upper soil layer has less influence on overall non-linearity for Case 3 compared to Case 2. Another notable difference between these cases is that for Case 2, strains reduce dramatically when moving across the upper to lower layer interface. In contrast, Case 3 (Figure 4.19) shows that strains increase (but less drastically) when crossing the upper to lower layer interface. This occurs because softer soil layers typically experience higher strain levels.

Figure 4.19a also shows displacement oscillations at speeds greater than the critical velocity for the linear case. The critical speed computed using the linear analysis is located at 90 m/s which is related to the lower layer shear wave speed, while the second peak is at 136 m/s, and thus coincides with the shear wave velocity of the upper soil layer.

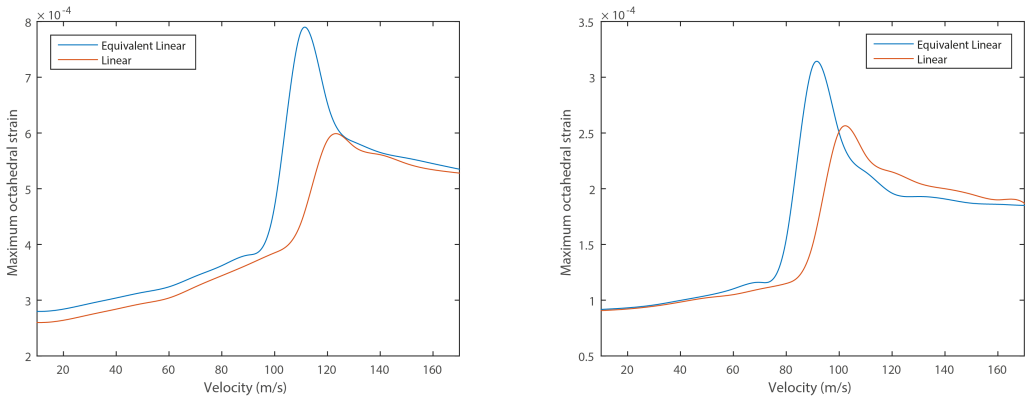

Fig. 4.20 Soil case 3 comparisons of linear and non-linear DAF curves of maximum octahedral strain (a) at Point A (b) at Point B

Figure 4.20 shows the relationship between maximum octahedral strain and train speed, for both soil formulations and at depths of 1m and 4m below the track. For the non-linear case at both depths, there is a more pronounced increase and decrease in strain levels immediately before/after the peak strain values. These peaks are 8.3% and 11.5% lower than the linear case, in terms of critical velocity, respectively, but the magnitudes are 30.7% and 27.8% higher than the linear result. Although, for all cases, strain levels are lower than those for Case 2, at higher speeds, the decrease in strain levels at very high speed is also lower than Case 2. Interestingly, at very low and very high speeds, strain levels are similar for the linear and non-linear cases. The main discrepancy occurs in a localised speed range close to the critical velocity where the amplification effects are more dominant.

Considering the linear cases, the peak values do not correspond to the shear wave speeds of either the upper or lower supporting soil. This difference is caused by the complex dispersion characteristics of the inversely-dispersive profile.

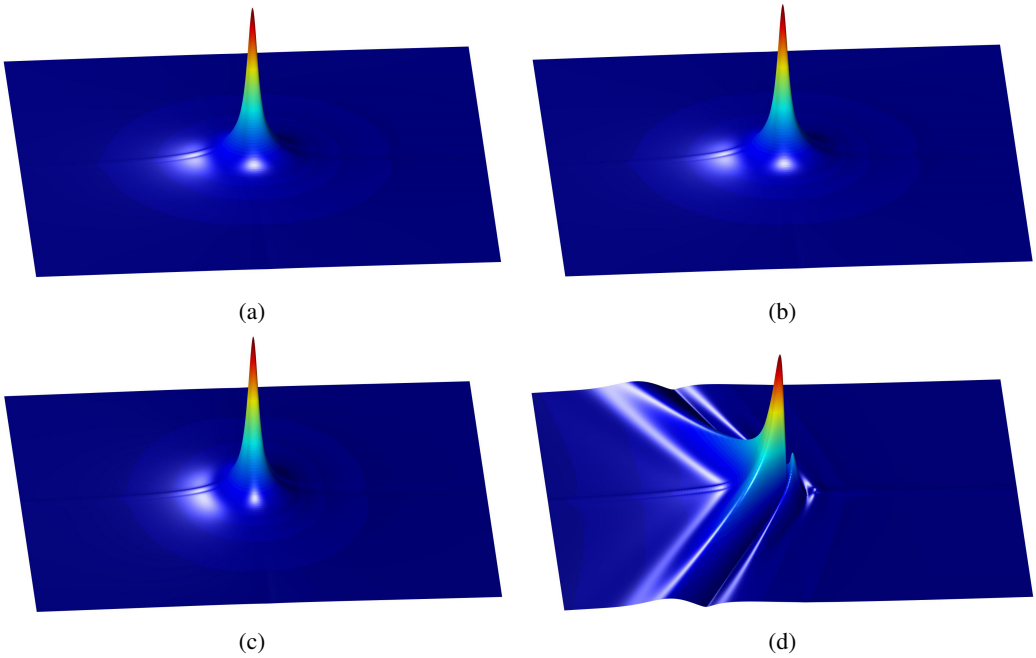

Fig. 4.21 Normalised ground surface contours (a) Linear: c = 10 m/s (b) Non-linear: c = 10 m/s (c) Linear: c = 80 m/s (d) Non-linear: c = 80 m/s

Finally, Figure 4.21 shows ground surface contour plots for high (80m/s) and low (10m/s) speed wheel passages, computed using both linear and non-linear formulations. At low speed, the soil response is uniform and symmetrical, and the contours for the linear and non-linear formulations are similar. However, at high speed, the linear and non-linear responses are markedly different. The linear formulation is relatively uniform and similar to both low speed responses, however, the non-linear result has a significantly pronounced wavefront. This occurs because the moving load speed is at the critical velocity of the non-linear soil (i.e. degraded stiffness soil), while it is below the linear critical velocity. Therefore it can be concluded that track-ground behaviour can be markedly different when considering linear and non-linear soil behaviour.

4.4.4 Soil case 4

Soil Case 4 is a homogeneous half-space, similar to Case 1, however with a greater stiffness (E=200MPa). Figure 4.22a shows the relationship between rail displacement and train speed, where it is seen that the curve shape for both formulations is similar. However, the non-linear formulation shows a 1.3% increase in maximum displacement and 15.8% decrease and critical velocity respectively. Although the change in critical speed is comparable to Case 1, the increase in magnitude is significantly different (20.7% for Case 1). Also, for Case 1, rail displacements at low speed are greater for the non-linear case, however when the soil has a Young modulus of 200 MPa, the displacements are almost identical at speeds below 70m/s. This occurs

because the elevated stiffness results in the generation of lower strains inside the soil stratum. This is seen in Figure 4.22b which compares strain with depth for low speed (10m/s) and at the non-linear critical velocity (150m/s). The high speed case exhibits higher maximum strain levels (4.24×10^{-4} compared to 1.92×10^{-4} for the low speed case). However, these are still relatively low, meaning soil stiffness degradation is also low.

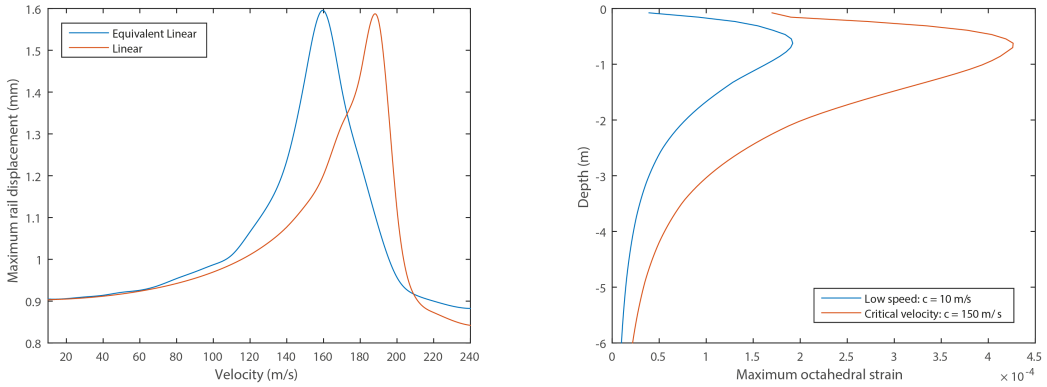

(a) (b)

Fig. 4.22 Soil case 4, (a) comparisons of linear and non-linear DAF rail displacement curves, (b) Maximum (non-linear) shear strain vs depth for c = 10 m/s and c = 150 m/s

4.5 Discussion

The four case studies presented show that train speed has a marked effect on track-ground response during train passage. Table 4.7 summarizes the results and shows that dynamic track deflections increase with speed from their static value by between 58% and 120%.

Further, Table 4.7 quantifies the large discrepancy between track displacements computed using linear and non-linear formulations. This discrepancy is up to 30% for the case of a soft soil overlying a stiffer soil, however is less of a problem when the entire soil layer is stiff. Table 4.7 also shows that the critical speed is influenced when considering non-linearity. For all soil cases, the critical velocity is shifted to a lower value, ranging between 80-89% of the original linear value. Also, at speeds close-to, but below the critical velocity, the non-linear formulation reveals that the gradient of the dynamic amplification curve is much steeper with respect to speed compared to the linear case.

These two findings are important when designing high speed lines because often 70% of the linear critical speed is chosen as the cut-off track-foundation design criteria. Therefore, if the railway track/foundations are designed to have a critical speed $\approx$ 50-70% of the linear value, the track may be of risk of high dynamic

effects. As an example, Case 2 shows a very steep velocity-displacement gradient immediately prior to the critical velocity, indicating small speed changes will radically alter track deflections. Therefore this could be problematic if it is decided to increase train speeds slightly in the future.

It should be noted that the reduction in critical speed is dependent upon the characteristics of the soil, because the non-linear stiffness degradation of cohesive and granular soils is very different. Cohesive soils have plasticity and the sensitivity of their shear stiffness degradation curves to the confining stress is low. Alternatively, granular soils have a low plasticity index and are more greatly affected by confining stress. In practical railway situations, embankments are typically constructed using granular materials while the underlying soil might be cohesive. Therefore, in addition to the train-induced stresses, embankment stiffness degradation will be effected by confining stress, while the supporting soil might be more greatly affected by plasticity index.

It should also be noted that although this research presents dynamic amplification curves considering subgrade non-linearity, the results are for a single wheel passage only. This is acceptable for linear simulations, however for non-linear ones, the results can be greatly affected by vehicle axle configuration (i.e. axle spacing) and, the axle load. Therefore, when investigating the effect of subgrade non-linearity in practise, rolling stock configuration should be considered since it has a strong influence on track-ground behaviour.

Finally, stiffness degradation and consequently the reduction of the critical speed can have a strong impact on the accumulation of permanent strains in the ground. This can be investigated using shakedown limit analysis, such as that presented by Alves Costa et al. [6].

Table 4.7 Summary of effect of non-linearity on rail displacements and critical velocity

	Rail displacement		Critical speed
	Increase from maximum linear displacement	Increase from static displacement	Increase from linear speed
Soil case 1	24.6%	114.5%	12.2%
Soil case 2	29.5%	120.5%	20.0%
Soil case 3	7.2%	58.1%	11.3%
Soil case 4	1.3%	77.4%	15.8%

4.6 Linear and non-linear comparison

In Chapter 3, soil improvement or replacement strategy used on new railway lines to increase track stiffness has been discussed. It is necessary to determine the optimum depth and magnitude of stiffness improvement required, with respect to cost. A semi-analytical model considering linear elastic properties of soil was proposed and used to rapidly assess the effect of different soil improvement depths and stiffness' on track behaviour. This is a challenging analysis because the localised improvement of soil layers results in large stiffness contrasts and increases the likelihood of the presence of sandwiched low stiffness layers which can cause multiple critical velocities.

Therefore, it is very interesting to look into the changes in the dynamic responses from linear and non-linear models. To illustrate this, Figure 4.23 shows the effect of soil replacement/remediation on maximum slab track deflections. The original soil is a homogenous half-space with 45MPa stiffness, with the same non-linear stiffness characteristics as shown earlier in this chapter. The soil is then locally stiffened, considering 5 discrete depths (1, 2, 3, 4, 5m) and 3 magnitudes of stiffness improvement (150, 200, 250MPa). The damping for all soils is set as 0.03. It is clear that the relationship between track deflection and improvement depth, as well as between track deflection and stiffness magnitude are both non-linear relationships. Interestingly, deploying 1m of 250MPa improvement results in minimal change in track deflection, while 1m of 150MPa and 200MPa improvement result in a magnification of displacement (as shown in Figure 4.23b). This is due to the dynamic amplification curve which shows that like the original soil, the 150/200MPa cases are past the critical velocity, but closer to the peak than the original case.

Considering the relationship between track deflection and the stiffness magnitude of replacement soil, other than the 1m depth case discussed above, the stiffer soil results in lower deflections. The relationship is complex though because for some cases an extra 1m of improvement gives lower deflections than increasing the stiffness from 150MPa to 250MPa for the same depth (e.g. 1m of 250MPa fill versus 2m of 150MPa fill). However, in other cases, improving the stiffness from 150MPa to 250MPa while keeping depth constant, results in larger deflection than adding an additional 1m of improvement. Therefore, it is clear that when performing soil remediation, to minimise cost and maximise performance, it is important that both variables are considered.

It can be observed from Figure 4.23a that the linear 150MPa replacement results in larger deflections for 1m and 2m soil replacement strategies, however the linear model gives lower deflections when the soil

stiffening extends to 3m or larger. The reason for this is due to the change of critical velocity. As shown in Figure 4.23b, the linear model returns higher values because the the speed is right at the critical velocity, nonetheless the non-linear cases have past the critical velocity. When increasing the depth for the soil stiffening, the soil behaviour will change too and it leads to the increase of the track deflections as shown in Figure 4.23a.

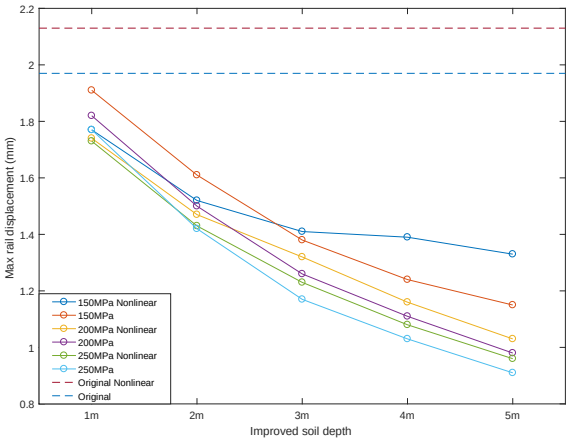

(a)

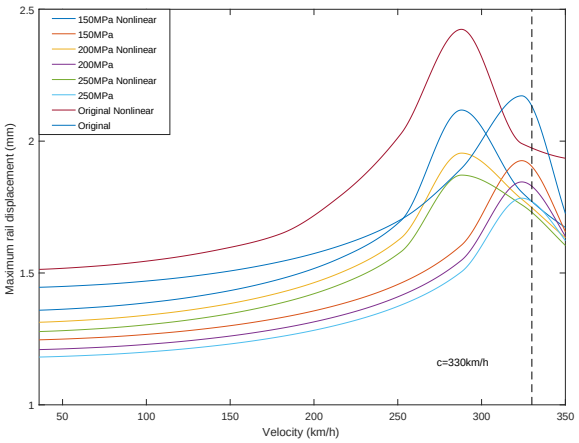

(b)

Fig. 4.23 (a) Non-linear soil improvement quantification, (b) Corresponding DAF curves for 1m improvement

Looking at the changes of the track deflections from linear to non-linear model, it can be indicated that the inclusion of non-linearity and different remediation solutions have an impact on the maximum track deflection magnitude. For original soil, the consideration of soil non-linearity brings 17.2% increase in track displacement magnitude (from 2.05mm to 2.41mm). When applying 1m of 150MPa soil replacement, it rises from 1.87mm to 2.12mm showing 13.4% of increment. However, this increase in magnitude slows down drastically when using 200MPa and 250MPa replacement, with only 7.1% and 5.9% rises, respectively.

This provides an insight when designing a railway line because it is of great importance to avoid critical velocity and diminish the critical velocity effect to the maximum.

It can also be observed from Figure 4.23b that there shows a clear shift of the peak values on the DAF curves, from 326km/h to 275km/h, as well as the corresponding track deflection magnitudes. It reveals the effect of non-linearity on the resulted track dynamics and implies significant importance on the railway line design, especially in the case of relatively soft subgrade (e.g. 45MPa). It also is very interesting to see that the critical speeds of linear and non-linear DAF curves of the corresponding remediation strategies are almost the same (i.e., the critical speeds for linear and non-linear cases fall at 326km/h and 275km/h, respectively). It is mainly owing to the fact that the stiffness of the upper layer (replacement layer) is much higher than the lower layer (original soil) and the critical speed is then dominated by the properties of the lower layer without relevant influence of the track stiffness or replacement soil stiffness. This observation echos with the findings in the work of Alves Costa et al. [5].

4.7 Conclusion

This chapter presents a frequency domain numerical model to investigate the effect of soil non-linearity on the response of high speed railway lines. The model uses analytical expressions to describe the response of the track and a thin-layer element method for the ground. The model is coupled with a 'linear equivalent' formulation to allow the soil stiffness to change depending upon strain level. The linear stress-strain implementation is validated using an independently published dataset and the non-linear response is validated using field data collected on a high-speed railway line. The model is used to investigate four railway case studies, each with highly contrasting subgrade characteristics. It is found that non-linearity has a very significant influence on track-ground response. For example, the critical velocity shifts to as low as 80% of the linear case, while rail deflections are up to 30% higher. Further, at speeds close-to, but below, the non-linear critical velocity, dynamic amplification is highly sensitive to small increases in train speed. These findings depend upon material properties, and are important for high speed rail track-earthwork designers because often 70% of the linear critical velocity is used as a design limit. However, this work shows that designs close to this limit may be still at risk of high dynamic effects, particularly if the line speed is increased slightly at a later stage.

Chapter 5

Fully non-linear track and subgrade behaviour

5.1 Introduction

Following the public demand for the development of more sustainable transport systems, the technical and scientific communities have been exerting a considerable effort to achieve a better understanding of this subject and, simultaneously, to look for different mitigation solutions for the noise and ground vibration problems arising from railway traffic. Among those efforts, the proposal and development of appropriate prediction models play a key role, although this can be a challenging task.

In order to simulate the wave propagation in the longitudinal direction of a track, while saving the computation time, the 2.5D (two point five dimensional) analysis concept was proposed and adopted by Yang and Hung [181] for the railway applications. Under the 2.5D scheme, only the cross section of the problem needs to be discretized as it takes advantage of the Fourier transformation of the spatial variable in the direction of the track. Based on similar ideas, a wavenumber finite/boundary element method (FEM-BEM) was proposed by a number of researchers (Sheng et al. [155], Degrande et al. [43], Gupta and Degrande [72], Müller et al. [134], Galvín et al. [68], Alves Costa [1] and Alves Costa et al. [4]) to predict the vibration spectra for track structures.

Additionally, faster and heavier trains have led to an increase in track degradation on the track structure. The resilient behaviour of track geomaterials (mainly ballast or subballast) is usually assumed to be linear

elastic and elastic modelling can be used to estimate the behaviour of materials within small strain levels, but it is incapable of predicting the material behaviour for stresses that exceed the limit. Therefore, it is necessary to also include the track non-linearity in the modelling.

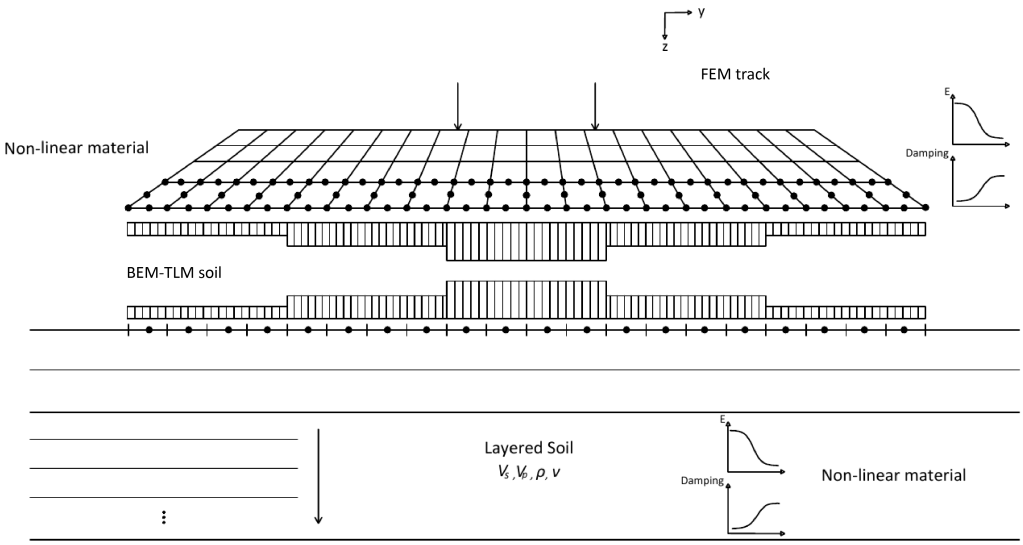

Fig. 5.1 Schematic illustration of the proposed 2.5D FEM-BEM-TLM model

This chapter continues on with the works from Chapter 3 and Chapter 4. The author proposes a novel 2.5D FEM-BEM-TLM model that contains fully non-linear track and subgrade model to study the track-ground response due to the train passsage, as shown in Figure 5.1. Unlike other FEM-BEM models, the proposed FEM-BEM-TLM model takes advantage of thin-layer soil model to assess the soil responses and is able to include the non-linear effect in the model by adopting the equivalent linear approach. The following characteristics have made the 2.5D FEM-BEM-TLM robust and versatile:

- The track structure is fully modelled with the finite element method, which makes it more accurate and capable of calculating the response inside the track structure
- It is able to introduce material non-linearity into both track and soil for more precise predictions of track and soil behaviour under various condititions
- The coupling between track and soil in the previously proposed models uses the relaxed boundary condition, meaning the coupling is achieved only by taking into consideration of the vertical component (i.e., the most dominant component) of the response. However, the proposed 2.5D FEM-BEM-TLM takes into account the coupling in all three directions (i.e, vertical, transversal and longitudinal), hence leading to a more accurate behaviour.

This chapter contains six sections. Section 5.2 introduces the mathematical formulation of 2.5D FE model. Comprenhensive explanation and development of a novel FEM-BEM-TLM model are given in Section 5.3. It is followed by three separate validations against commercial software simulation and published results in Section 5.4. Subsequently, Section 5.5 includes examples of impacts of the full mateiral non-linearity on the induced track-ground responses. In the end, a brief discussion over the findings is given in Section 5.6, followed by the conclusion for the chapter in Section 5.7.

5.2 2.5D FE model

In the formulation of the 2.5D finite element, the three-dimensional problem is solved by taking advantage of the Fourier transform relative to the longitudinal direction of the medium. For this transformed opeartion to be applied, it is necessary that the track structure is invariant in the longitudinal direction and the dynamic response of medium is assumed to be linear.

This thesis will only present and discuss the mathematical formalations that are necessary and critical for the application of this approach in the model. Therefore, general aspects of the finite element method development are omitted here, which can be easily found in the works of Kausel [95], Yang and Hung [181], Alves Costa et al. [4] and Alves Costa [1].

5.2.1 General equilibrium equations

To formulate an elastodynamic problem using the finite element method, the principle of virtual work is commonly applied to obtain the fundamental equations of elastodynamics. As one of the most widely used variational principle, Hamilton's principle serves as the basis for the mathematical development of the method set forth herein. It postulates that for non-conservative systems (meaning damping is included), the work done by external and inertial forces on an allowable virtual displacement field is equal to the work done by internal forces on this virtual displacement field, added by the dissipated energy (Kausel [95]).

Considering that the excitation source has a harmonic character over time with frequency ω (frequency domain analysis), to derive the equations of motion, Hamilton's principle can be expressed as:

$$\int_V \delta\varepsilon^T \sigma dV - \omega^2 \int_V \delta\mathbf{u}^T \rho\mathbf{u} dV = \int_S \delta\mathbf{u}^T p dS \tag{5.1}$$

Where δ is the variational operator, ε, σ and $\mathbf{u}$ represents the field of strains, stresses and displacements, respectively, and ρ is the density of the medium and p accounts for the external forces applied to the surface of the medium.

The formulation of the method considering displacements as base variables requires the establishment of displacement-strain and strain-strain relations. The strain field can be derived from the displacement field by introducing the operator $[\mathbf{L}]$, as shown in Equation 5.2 .

$$\varepsilon = \begin{Bmatrix} \varepsilon_x \\ \varepsilon_y \\ \varepsilon_z \\ \gamma_{xy} \\ \gamma_{yz} \\ \gamma_{xz} \end{Bmatrix} = \begin{Bmatrix} \frac{\partial u_x}{\partial x} \\ \frac{\partial u_y}{\partial y} \\ \frac{\partial u_z}{\partial z} \\ \frac{\partial u_x}{\partial y} + \frac{\partial u_y}{\partial x} \\ \frac{\partial u_y}{\partial z} + \frac{\partial u_z}{\partial y} \\ \frac{\partial u_x}{\partial z} + \frac{\partial u_z}{\partial x} \end{Bmatrix} = [\mathbf{L}]\mathbf{u} \tag{5.2}$$

Where opearator $\mathbf{L}$ has the form:

$$[\mathbf{L}] = \begin{bmatrix} \frac{\partial}{\partial x} & 0 & 0 \\ 0 & \frac{\partial}{\partial y} & 0 \\ 0 & 0 & \frac{\partial}{\partial z} \\ \frac{\partial}{\partial y} & \frac{\partial}{\partial x} & 0 \\ 0 & \frac{\partial}{\partial z} & \frac{\partial}{\partial y} \\ \frac{\partial}{\partial z} & 0 & \frac{\partial}{\partial x} \end{bmatrix} \tag{5.3}$$

In addition to the strain-displacement relationship, it is also necessary to introduce a law of material behaviour in order to establish the relationship between stresses and displacements. For linear elastic materials, the stress-strain law is defined in Equation 5.4 by introducing the matrix $[\mathbf{D}]$:

$$\sigma = [\mathbf{D}]\varepsilon = [\mathbf{D}][\mathbf{L}]\mathbf{u} \tag{5.4}$$

Where σ is the stress vector and $[\mathbf{D}]$ is the constitutive matrix of an isotropic material, with both already been explained in Chapter 3.

Combining Equation 5.1, Equation 5.2 and Equation 5.4, the equilibrium equation can be then established as follows:

$$\int_V \delta\varepsilon^T \mathbf{L}^T \mathbf{D}\mathbf{L}\mathbf{u} dV - \omega^2 \int_V \delta\mathbf{u}^T \rho \mathbf{u} dV = \int_S \delta\mathbf{u}^T p dS \tag{5.5}$$

After obtaining the equilibrium equation, the next step is to discretize the medium into small elements and then apply the equilibrium relationship defined by Equation 5.5 to each individual element and eventually assemble all the individual elements to form the global equation.

5.2.2 Element formulation

For each finite element, only its cross-section needs to be discretized due to the fact that the structure is considered as longitudinally invariant. Therefore, the field of displacements can be approximated by Equation 5.6.

$$[\mathbf{u}] = [\mathbf{N}][\mathbf{U}] \tag{5.6}$$

Where **U** represents the vector covering the displacements corresponding to the three degrees of freedom (DoFs) of the cross-section nodes of the element and **N** is the matrix of the shape functions that are used for the interpolation of displacements inside a finite element. The configuration of this matrix is similar to the one adopted in a three-dimensional finite element formulation, namely:

$$[\mathbf{N}] = \begin{bmatrix} N_1 & 0 & 0 & N_2 & 0 & 0 & \cdots & N_n & 0 & 0 \\ 0 & N_1 & 0 & 0 & N_2 & 0 & \cdots & 0 & N_n & 0 \\ 0 & 0 & N_1 & 0 & 0 & N_2 & \cdots & 0 & 0 & N_n \end{bmatrix} \tag{5.7}$$

Where n is the total number of nodes inside an element. In the presented numerical model, quadratic isoparametric finite elements (8 nodes) are adopted for better accuracy. The diagram of quadratic elements and their representation in the local coordinate system are shown in Figure 5.2. As for any other models based on the finite element method, the functions and variables within each element are expressed explicitly by local coordinates and are then transformed from the local reference to the global reference. The shape functions of

quadratic finite elements are given in the Table 5.1, where ξ_a and η_a are values of local coordinates ξ and η at nodes.

Table 5.1 Shape functions of 8-node elements

Shape functions N_a	Node number a
$N_a = \frac{1}{2}(1+\xi\xi_a)(1-\eta^2)$	$a = 4,8$
$N_a = \frac{1}{2}(1+\eta\eta_a)(1-\xi^2)$	$a = 2,6$
$N_a = \frac{1}{4}(1+\xi\xi_a)(1+\eta\eta_a)(\xi\xi_a+\eta\eta_a-1)$	$a = 1,3,5,7$

Substituting Equation 5.6 into Equation 5.2, the direct relationship between deformations and nodal displacements can be established.

$$\varepsilon = [\mathbf{L}]\mathbf{u} = [\mathbf{L}][\mathbf{N}][\mathbf{U}] = [\mathbf{B}][\mathbf{U}] = ([\mathbf{B}_1] + \frac{\partial}{\partial x}[\mathbf{B}_2])[\mathbf{U}] \tag{5.8}$$

Where $\mathbf{B}$ is the strain matrix that can be decomposed into the sub-matrices $\mathbf{B}_1$ and $\mathbf{B}_2$ ($\mathbf{B} = \mathbf{B}_1 + \frac{\partial}{\partial x}\mathbf{B}_2$). Since $\mathbf{B} = [\mathbf{B_1}, \mathbf{B_2}, \cdots, \mathbf{B_n}]$, where n represents the total number of nodes in the element, hence the contents of the sub-matrices can be defined in Equation 5.9 and Equation 5.10.

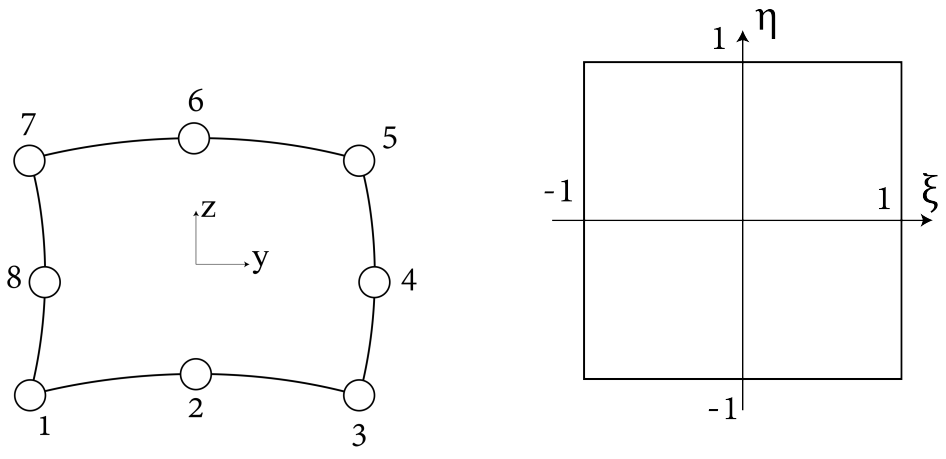

(a) (b)

Fig. 5.2 Schematic plot of an 8-node quadratic element (a) and its representation in the local coordinate system (b)

$$[\mathbf{B}_a]_1 = \begin{bmatrix} 0 & 0 & 0 \\ 0 & \frac{\partial N_a}{\partial y} & 0 \\ 0 & 0 & \frac{\partial N_a}{\partial z} \\ \frac{\partial N_a}{\partial y} & 0 & 0 \\ 0 & \frac{\partial N_a}{\partial z} & \frac{\partial N_a}{\partial y} \\ \frac{\partial N_a}{\partial z} & 0 & 0 \end{bmatrix} \tag{5.9}$$

$$[\mathbf{B}_a]_2 = \begin{bmatrix} N_a & 0 & 0 \\ 0 & 0 & 0 \\ 0 & 0 & 0 \\ 0 & N_a & 0 \\ 0 & 0 & 0 \\ 0 & 0 & N_a \end{bmatrix} \tag{5.10}$$

As can be observed from Equation 5.9, the derivatives present in the matrix $[\mathbf{B}_a]_1$ refer to the global coordinate system but the shape functions are built in the local coordinate system. Therefore, it is necessary to establish a relation that allows the derivatives to pass from the local coordinate system (ξ, η) to the global coordinate system (y, z). This can be achieved by the introduction of Jacobian matrix as indicated in the Equation 5.11. The components of the Jacobian matrix are calculated using derivatives of shape functions N_a in respect to the local coordinates ξ, η and global coordinates of element nodes y_a, z_a.

$$\begin{bmatrix} \frac{\partial N_a}{\partial \xi} \\ \frac{\partial N_a}{\partial \eta} \end{bmatrix} = \begin{bmatrix} J \end{bmatrix} \begin{bmatrix} \frac{\partial N_a}{\partial y} \\ \frac{\partial N_a}{\partial z} \end{bmatrix} \tag{5.11}$$

Where

$$\begin{bmatrix} J \end{bmatrix} = \sum_{a=1}^{n} \begin{bmatrix} \frac{\partial N_a}{\partial \xi} y_a & \frac{\partial N_a}{\partial \xi} z_a \\ \frac{\partial N_a}{\partial \eta} y_a & \frac{\partial N_a}{\partial \eta} z_a \end{bmatrix} \tag{5.12}$$

The system of equations governing the dynamic equilibrium of the finite element can be defined in a similar way as described in Chapter 3. In the frequency-wavenumber domain, this equation can be mathematically written as:

$$([\mathbf{K_1}] + ik_x[\mathbf{K_2}] + k_x^2[\mathbf{K_3}] - \omega^2[\mathbf{M}])\mathbf{U} = \mathbf{P} \tag{5.13}$$

Where the three stiffness matrices are given by:

$$[\mathbf{K_1}] = \int_{-1}^{1}\int_{-1}^{1}[\mathbf{B_1}]^T[\mathbf{D}][\mathbf{B_1}]|J|d\eta d\xi \tag{5.14}$$

$$[\mathbf{K_2}] = \int_{-1}^{1}\int_{-1}^{1}[\mathbf{B_1}]^T[\mathbf{D}][\mathbf{B_2}]|J|d\eta d\xi - \int_{-1}^{1}\int_{-1}^{1}[\mathbf{B_2}]^T[\mathbf{D}][\mathbf{B_1}]|J|d\eta d\xi \tag{5.15}$$

$$[\mathbf{K_3}] = \int_{-1}^{1}\int_{-1}^{1}[\mathbf{B_2}]^T[\mathbf{D}][\mathbf{B_2}]|J|d\eta d\xi \tag{5.16}$$

And the corresponding mass matrix is determined as follows:

$$[\mathbf{M}] = \int_{-1}^{1}\int_{-1}^{1}[\mathbf{N}]^T\rho[\mathbf{N}]|J|d\eta d\xi \tag{5.17}$$

The intergrals presented in the equations above are evaluated numerically using the classical Gauss integration rule. As can be seen, the equations are given in the local coordinate system, however the integration can be performed similarly in the global coordinate system by taking into account the relationship between the local and global references (i.e., $dydz = |J|d\eta d\xi$). Then the stiffness and mass matrices of each element are assembled to form the overall global system of equations.

Since the system of equations is formulated in the frequency-wavenumber domain, obtaining the result in the untransformed three-dimensional domain requires the application of an inverse Fourier transform with regard to k_x. As with the methods outlined in Chapter 3, the introduction of constant or harmonic moving loads is facilitated by the translation property of the Fourier transform. It requires neither the adoption of any complex computational scheme, nor the increased computational effort, which makes it handy and efficient.

5.3 2.5D FEM-BEM-TLM model

The track–ground dynamic response induced by the train passage is computed by a numerical procedure based on the coupling between the finite elements and boundary elements methods, both formulated in the

2.5D domain. Since it is assumed that the dynamic problem is linear, the formulation can be developed in the wavenumber–frequency domain, employing Fourier transforamtion for space (only in the track development direction). This procedure, called 2.5D, allows obtaining 3D solutions without the need of numerical discretization of the space along the direction of the track.

Domain decomposition is used to solve the dynamic problem, with the track being modelled by the 2.5D FEM and the layered ground simulated through 2.5D BEM with the Green's functions computed by the thin-layer approach (TLM). 2.5D FEM has been described in Section 5.2 and the computation for the Green's functions and the use of TLM have been extensively studied in Chapter 3 and Chapter 4. In this section, the formulation and development of the combined FEM-BEM-TLM model will be presented. A schematic representation of the method can be viewed in Figure 5.3, in which the interaction between the two corresponding domains is made along a horizontal plane on the free surface of the subgrade.

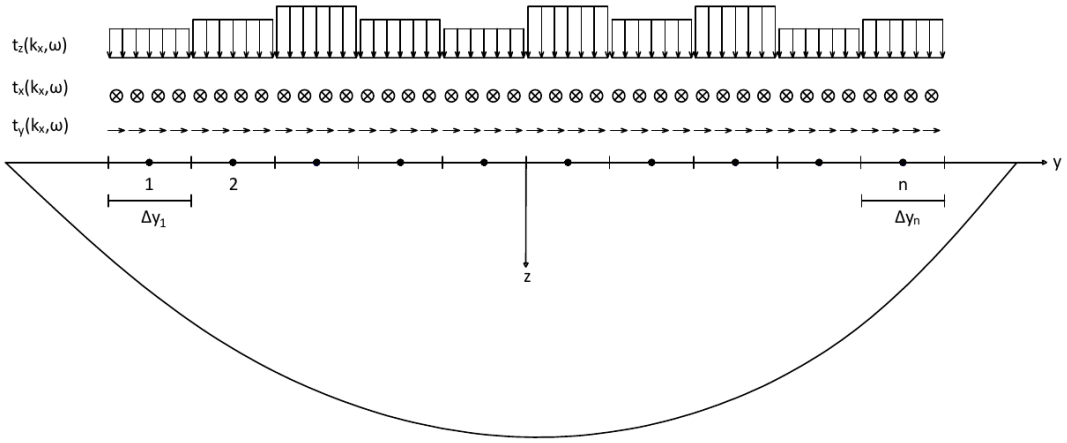

Fig. 5.3 Schematic diagram of the coupling between FEM and BEM-TLM domain

5.3.1 Generalities

As mentioned above, The proposed method uses the Green's functions (detailed in Chapter 3) to describe the dynamic response of the homogeneous or layered subgrade. The coupling between FEM domain and BEM domain is performed by a finite element formulation, which comprises the transformation of the flexibility matrix that governs the dynamic behaviour of the BEM domain into a dynamic stiffness matrix. The formulation allows a significant reduction of the boundary element mesh because only the interface that connects to the finite element domain needs to be taken into account.

The dynamic equilibrium equations of the medium can then be expanded from Equation 5.13 by adding the behaviour of the BEM domain. After introducing the discretization of the cross-section into 2.5D finite elements and applying the Fourier transform regarding the x coordinate, the dynamic equilibrium is described by the following system of equations:

$$([\mathbf{K_1}] + ik_x[\mathbf{K_2}] + k_x^2[\mathbf{K_3}] + k_x^4[\mathbf{K_4}] - \omega^2[\mathbf{M}] + [\mathbf{K_5}])\mathbf{U} = \mathbf{P} \tag{5.18}$$

Where global stiffness matrices $\mathbf{K_1}$ to $\mathbf{K_4}$ and mass matrix $\mathbf{M}$ are already explained in the last section, k_x is the Fourier image of the coordinate x, $\mathbf{U}$ is the vector of the nodal displacements, and $\mathbf{P}$ is the vector of the external forces, and finally $\mathbf{K_5}$ represents the matrix that collects the impedance terms of the layered subgrade. Solving this system of equations, the displacements on the transformed domain are obtained, which can be changed to the time-space domain through the inverse Fourier transform process.

5.3.2 2.5D BEM-TLM formulation

In Equation 5.18, all the matrices are independent of the frequency and wavenumber except for the matrix $\mathbf{K_5}$. This is due to the fact that the stiffness matrix $\mathbf{K_5}$ represents the ground impedance and it is calculated from the flexibility matrix that governs the dynamic behaviour of the domain described by 2.5D BEM.

The fundamental basis for defining all boundary integral equations in an elastodynamic problem is the dynamic reciprocity theorem (Andersen [8]). It specifies a relationship between displacements and stresses in two elastodynamic states. Several 2.5D boundary integral equations have been proposed by a number of researchers. Sheng et al. [154] adopted a 2.5D boundary integral equation based on the reciprocity theorem. François et al. [64] used a new methodology based on a regularized version of the boundary integral equation in order to avoid the analytical integration of singular terms. But the approach presented here is simpler, since the coupling between the FEM and BEM domains occurs along the ground surface, not allowing the embedment of the finite element mesh inside the BEM domain. Similar approach is also used and described in the works of Alves Costa [1] and Alves Costa et al. [2]. In this case, taking the reciprocity theorem and the Somigliana's identity into account, the boundary integral equation assumes the following configuration:

$$u_j(\mathbf{x}, \omega) = \int_\Sigma u_{ji}^G(\mathbf{x}, \mathbf{y}, \omega) p_i(\mathbf{y}, \omega) d\Sigma \tag{5.19}$$

Where u_j corresponds to the displacement of the point with coordinates x when a pressure, p_i, is applied along the surface Σ (belonging to the ground surface, as shown in Figure 5.4). u_{ji}^G is the tensor of Green's functions of the displacements. The derivation of Equation 5.19 is beyond the scope of the thesis and the details can be found in the works of Andersen [8] and Alves Costa [1].

For the computation of Green's functions of the displacements, several methodologies can be followed. Since the objective is to find the BEM matrices in the 2.5D domain, it is only natural and efficient to opt for the 2.5D Green's function for a homogeneous half-space proposed by Tadeu and Kausel [160]. However, despite the analytical elegance of that approach, if the geometry involves a layered half-space, the use of the homogeneous half-space solution has the main disadvantage that the layer interfaces of the half-space have to be discretized with boundary elements. In order to avoid this scenario, foundamental Green's functions computed in the wavenumber-frequency domain using a hybrid formulation of the thin-layer method (TLM) are adopted, as proposed by Kausel [98]. This approach has the advantage of making boundary elements discretization only necessary along the surface that establishes the connection between the layered ground and finite element domain. More importantly, the inclusion of TLM can eventually help study the dynamic responses inside the layered soil and also introduce the non-linearity to the model, making it more robust and versatile.

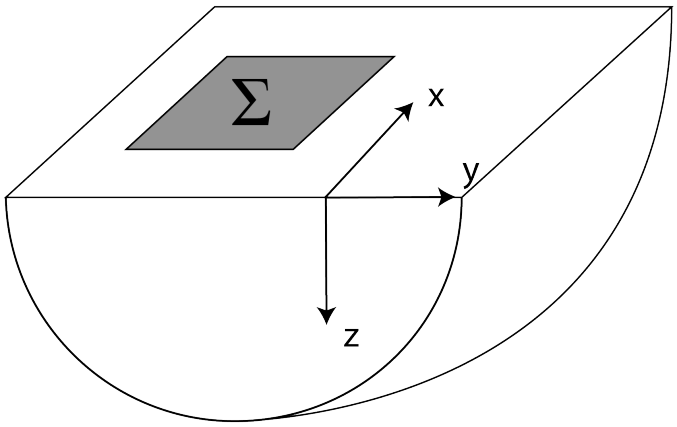

Fig. 5.4 Ground under pressure applied to an area inscribed on the free surface

When applying the pressure distributed in area Σ, Equation 5.19 reflects that it is capable of determining the displacement vector at any point in the domain by computing the tensor of Green's function of the displacements. As presented in Chapter 3, Green's functions can be calculated in the transformed domain using thin-layer method (TLM).

The introduction of the ground surface discretization is preceded by some simplifications that must be mentioned and clarified. In the approach followed in the present work, only linear boundary elements are used, with one collocation point (in the middle of the element) and with its dimension defined by the length of the edge of the neighbouring finite element. It should be noted that the neighbour finite element only presents two nodes along the side of connection FEM-BEM, which means that some error of approximation is allowed between the displacements computed by both methods along the connection surface.

Considering the 2.5D discretization and the schematic representation shown in Figure 5.1, the BEM equilibrium equation can be described as:

$$u_n(k_x,\omega) = [\mathbf{G}(k_x, y_j - y_i, 0, \omega)]\mathbf{t}(k_x,\omega) \tag{5.20}$$

Where u_n is the vector that collects the displacements of the collocation points; $\mathbf{t}$ is the vector of the applied pressure along each boundary element (shown in Figure 5.3) and $\mathbf{G}$ corresponds to the flexibility matrix of the domain. The terms of the matrix $\mathbf{G}$ can be obtained using the following equation:

$$G_{ji}(k_x, y_j - y_i, 0, \omega) = \int_{-\infty}^{\infty} 2u_{ji}^{G}(k_x, k_y, 0, \omega)\frac{\sin(k_y \Delta y_i/2)}{k_y} e^{ik_y(y_j - y_i)} dk_y \tag{5.21}$$

Where k_y is the Fourier image of the coordinate y; u_{ji}^{G} is the Green's function of displacements computed by TLM on the frequency-wavenumber domain; Δy_i is the dimension of the boundary element i, and y_i and y_j are the coordinates (along y direction) of the collocation points of the boundary elements i and j, respectively. In the model proposed in this research, the elements along the boundary are set to the same size, which means Δy_i will remain a constant in the calculation. It turns out to be convenient and efficient in the coding procedure.

Moreover, in Equation 5.21, u_{ji}^{G} is a tensor with 3×3 dimension, the matrix $\mathbf{G}$ has a $3n \times 3n$ dimension, where n represents the total number of elements along the interface. The computation of the flexibility matrix $\mathbf{G}$ can then take advantage of the dynamic reciprocity relations of the Green's functions and allow a substantial reduction in computational efforts.

The FEM-BEM coupling in this study is made into finite element sense, with the flexibility matrix $\mathbf{G}$ being transformed into the dynamic stiffness matrix $\mathbf{K_5}$ (as shown in Equation 5.18), through the following relationship:

$$[\mathbf{K_5}(k_x,\omega)] = [\mathbf{T_q}][\mathbf{G}(k_x,\omega)]^{-1}[\mathbf{T}] \tag{5.22}$$

Where $\mathbf{T}$ is a matrix that relates nodal displacements with the homologous evaluated in the collocation points and its dimension is $3n \times 3m$, where n and m represent the total number of elements and nodes along the interface respectively. Since 8-node elements are used in the formation of finite element structure, the relationship $m = 2n+1$ always stands, which means $\mathbf{T}$ is not a square matrix. Its formation can be depicted in Figure 5.5.

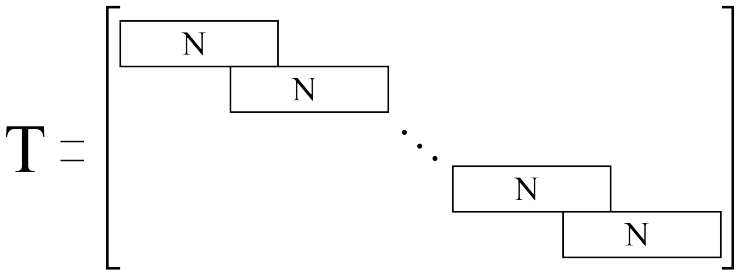

Fig. 5.5 Schematic diagram of the layout of the matrix [T]

Where $[\mathbf{N}]$ is defined as:

$$[\mathbf{N}] = \begin{bmatrix} 0 & 0 & 0 & 1 & 0 & 0 & 0 & 0 & 0 \\ 0 & 0 & 0 & 0 & 1 & 0 & 0 & 0 & 0 \\ 0 & 0 & 0 & 0 & 0 & 1 & 0 & 0 & 0 \end{bmatrix} \tag{5.23}$$

The matrix $\mathbf{T_q}$ results from the integration of the shape functions of the nodes on the finite elements that defines the interface between the finite elements and boundary elements. It is noted that the dimension of $\mathbf{T_q}$ is $3m \times 3n$ and the terms in $\mathbf{T_q}$ are determined by Equation 5.24:

$$[\mathbf{T_q}] = |\Delta y|[\mathbf{N_{int}}] \tag{5.24}$$

Where $|\Delta y|$ is the width of the bottom edge of the finite elements on the interface and $\mathbf{N_{int}}$ can be defined as follows:

$$[\mathbf{N_{int}}] = \begin{bmatrix} \frac{1}{6} & 0 & 0 \\ 0 & \frac{1}{6} & 0 \\ 0 & 0 & \frac{1}{6} \\ \frac{2}{3} & 0 & 0 \\ 0 & \frac{2}{3} & 0 \\ 0 & 0 & \frac{2}{3} \\ \frac{1}{6} & 0 & 0 \\ 0 & \frac{1}{6} & 0 \\ 0 & 0 & \frac{1}{6} \end{bmatrix} \tag{5.25}$$

Similar methodology was previously adopted by Alves Costa [1], from which a more comprehensive description of deduction of those matrices can be found. This thesis will not concentrate on the development of the mathematical theory behind it.

Since the motion and equilibrium of the domain are formulated by a 2.5D approach, where Fourier transforms are applied on the x coordinate and time, the simulation of moving loads is easy, and can be found in several papers related with this matter (Lombaert et al. [123], Sheng et al. [155], Auersch [12] and Alves Costa et al. [2]). This is one of the great advantages of using 2.5D formulations for the analysis of problems that deal with moving loads. As a matter of fact, the operations at the wavenumber-frequency domain allow including the moving load effect without the need of any complex procedure, simply taking into account the shift property of the Fourier transform. This property leads to a direct relationship (shown in Equation 5.26) between wavenumber, k_x, and the frequency, ω, through the knowledge of the speed of the moving load.

$$\omega = \Omega - k_x c \tag{5.26}$$

Where Ω is the driven frequency of the load and c is the moving load speed. This procedure avoids any change of the system of equations presented in Equation 5.18 and has been adopted extensively in the train-induced vibration analysis and also in this research work.

Solving the system of equations presented previously (i.e., Equation 5.18), the nodal displacements in the transformed domain are obtained, as well as the tractions along the coupling boundary. Combining the

Green's functions of the displacements, which are obtained from thin-layer model (TLM), the computation of the free-field response is a trivial step. Therefore, for a generic point of the ground surface with coordinate $y = y_0$, the free-field response is given by Equation 5.27 in the wavenumber-frequency domain:

$$u(k_x, y_0, 0, \omega) = \frac{1}{2\pi} \sum_{i=1}^{n} \int_{-\infty}^{\infty} 2u^G(k_x, k_y, 0, \omega) t_i \frac{\sin(k_y \Delta y_i/2)}{k_y} e^{ik_y(y_0 - y_i)} dk_y \tag{5.27}$$

Where n is the total number of boundary elements and all the other variables have the meanings explained previously in the thesis. The result demonstrates the overlapping contribution of the impact introduced by the pressures applied to each of the boundary elements. The computed responses are in the transformed domain, and a double inverse Fourier transformation with regard to frequency ω and wavenumber k_x is required to convert the outcome to the time-space domain.

5.3.3 Equivalent linear track model

When the track structure (mainly ballast/subballast) is subject to small strains, the stresses and strains are directly proportional, meaning the soil response can be considered linear and elastic. However, as the strains increase, this relationship becomes non-linear causing ballast/subballast stiffness to decrease, and damping to increase with strain. Consequently, the use of linear elastic geomaterials might not be appropriate and it is of great importance to take into consideration of material non-linearity.

Track non-linearity can be introduced by the 'equivalent linear' approach in a similar way as the soil model detailed in Chapter 4. By definition, it means that while the analysis remains linear, the track properties are updated as function of the strain level recorded in the track structure, thus simulating non-linear type effects. The iterative updating procedure is similar to what has been described in Chapter 4. This approach is implemented element-by-element with the FE formulation as follows:

1. Assume low strain (linear elastic) properties for all FE elements
2. Compute strain time histories and effective octahedral shear strain within all elements using Equation 4.1
3. Use stiffness-strain relationship curves which are functions of confining stress and plasticity index, to update the stiffness within each element (Figure 5.6a)

4. Use damping-strain relationship curves which are functions of confining stress and plasticity index, to update the damping within each element (Figure 5.6b)

5. Repeat steps 2 – 4 until the differences between shear modulus and damping of each element in two consecutive iterations fall below a pre-defined tolerance (i.e. 3% tolerance between iterations, as suggested by Alves Costa et al. [3])

While the soil stiffness and damping curves are obtained analytically, the elastic properties of large-grain material such as ballast and subballast are mainly obtained from laboratory tests. In this research, the experimental result from Dyvik and Kaynia [54] is used to determine the stiffness degradation and damping elevation curves for the proposed fully non-linear model. In the work of Dyvik and Kaynia [54], a number of large-scaled triaxial tests were completed on the railway ballast and subballast material and then a best fit curve is applied to capture its material behaviour. Figure 5.6 shows the testing results for shear modulus and damping ratio, together with the optimized best fit line.

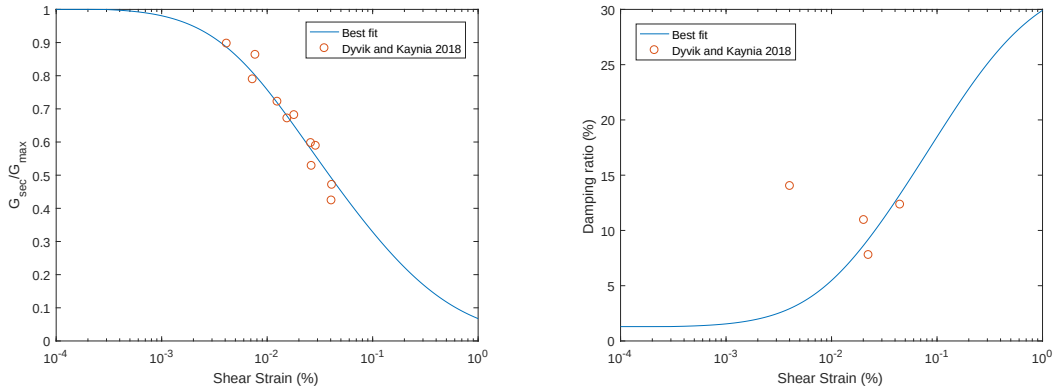

(a) (b)

Fig. 5.6 (a) Shear modulus reduction curve; (b) Damping ratio elevation curve obtained from large-scale triaxial tests (Dyvik and Kaynia [54])

The best fit lines for the shear modulus and damping ratio fit quite well with the data collected from the laboratory. However, due to strain measurement resolution inaccuracies with very small cyclic strains, there shows an 'outlier' in the testing result (Dyvik and Kaynia [54]) and it is negelected when finding the best fit line. The results have been found to have a good agreement with the outcome from previous studies (Indraratna et al. [82] and Lackenby et al. [114]). Therefore, Figure 5.6 will serve as the updating basis for the non-linear material studies carried out by the author in this research work.

5.4 Model validation

The proposed model contains a track structure represented by finite elements and more advanced coupling technique between the track and the subgrade. In order to validate the model, three different validation tasks completed in this section are outlined below:

- **Model validation 1 - FE model with static loads coupled with rigid base**: The finite element track structure is used in the model and it is important to validate the accuracy of FE track. An embankment is designed laying over the rigid bottom with two static point loads applied on top of it. The nodal displacements inside the embankment are used to compare against the result obtained from FE analysis software ABAQUS.

- **Model validation 2 - FE model with static loads coupled with subgrade**: The validation aims to test the coupling between the FE track and subgrade. A slab is laying on top of a homogeneous half-space in the model and two static point loads will be exerted on the slab surface. The nodal displacement inside the slab will again be compared against the result obtained from ABAQUS.

- **Model validation 3 - Full FEM-BEM-TLM model with moving load**: The full track-subgrade model will be validated against Chen's model (detailed in Chapter 3). The stress components in the subgrade are compared against both the published result from Chen et al. [32] and the semi-analytical model proposed by the author. It will demonstrate the robustness and accuracy of the model under the moving loads.

5.4.1 Model validation 1

To test the FE track model, an embankment is designed laying on the rigid base, which implies that the displacements of the bottom nodes are zero. The model representation is shown in Figure 5.7 and the properties of the embankment are given in Table 5.2. The upper width and the lower width of the embankment are 4m and 10m, respectively, and the thickness is 2m. Two static unit point loads are applied vertically on the two sides of the top surface of the embankment, located at $1m$ away from the central gauge line.

In order to validate the result, FE tests are performed using ABAQUS. The cross section of the FE track also has an upper width of 4m and lower width of 10m. The track is discretized into 20×4 meshes

(or elements) and each mesh is represented by an 8-node quadratic finite element. The encastre boudary condition is applied to the bottom of the track to ensure the rigidity of the soil. Also the infinite element is utilised to prevent wave reflections in the free-field. The mechanical properties are set the same as shown in Table 5.2.

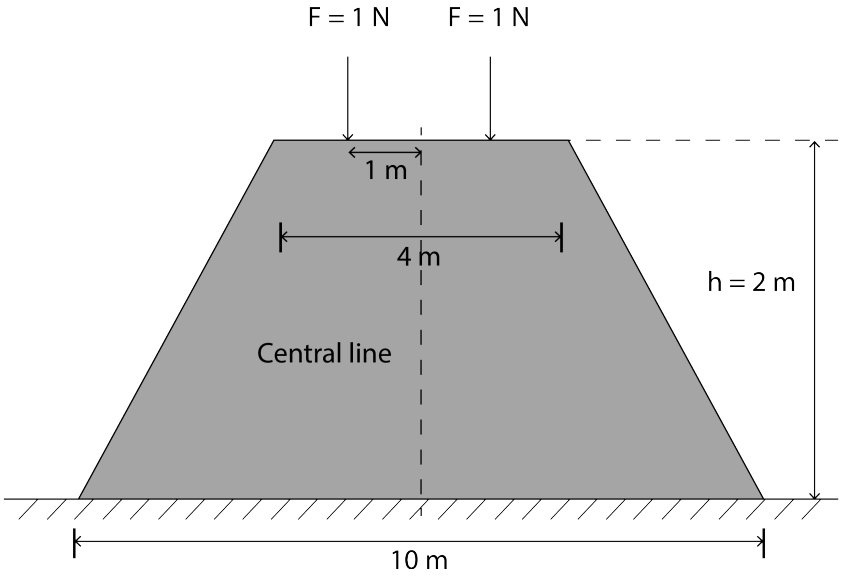

Fig. 5.7 Schematic diagram of the embankment structure

Table 5.2 Properties of the embankment for model 1

Embankment			
Density (kg/m^3)	2000	Young's modulus (MPa)	54
Damping ratio	0.03	Poisson's ratio	0.35
Upper width (m)	4	Lower width (m)	10
Thickness (m)	2		

In the validation, two different driven frequencies of the loads are used, i.e., f = 5Hz and 30Hz, to show the capability of the model under a variety of excitation frequency schemes. The nodal displacements inside the embankment are compared against the results obtained from ABAQUS to test the accuracy of the model. The comparisons, including both real and imaginary parts of the results under excitation frequency f = 5Hz and 30Hz, are given in Figure 5.8. The horizontal axis represents the node number and the vertical axis is the displacement of the corresponding node. The node count starts from the left bottom corner and moves to the right bottom, and then shifts to the next layer and continues to record its displacement until it reaches the last node in the finite element domain. By recording the nodal displacements in this way, it is more convenient to

compare against the corresponding displacements extracted from ABAQUS output. It can be observed that for both frequencies, the real and imaginary parts of the displacements are shown to be very close to the simulations from ABAQUS and a great match has been achieved from the FE model. It also can be seen that the magnitudes of the responses from 30Hz load are larger than those of 5Hz. This is because 30Hz is closer to the natural frequency of the embankment and hence the responses are more pronounced (Thompson [166]).

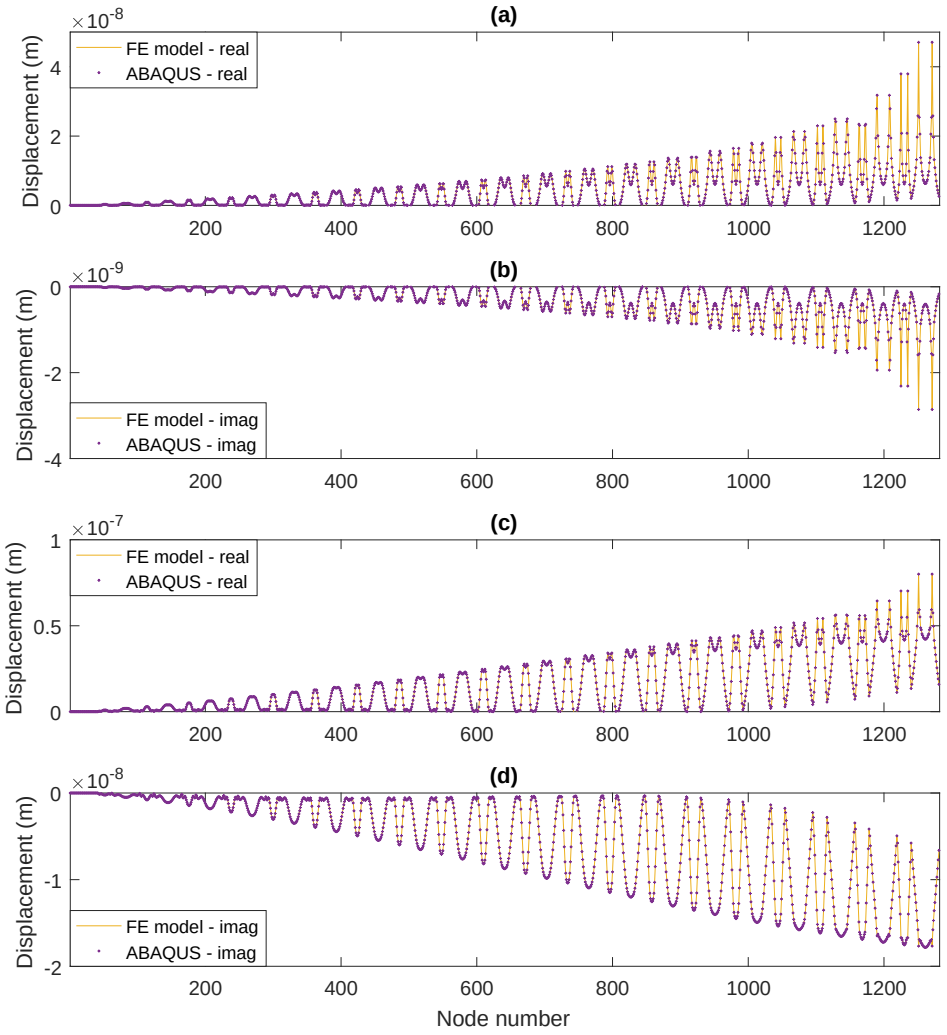

Fig. 5.8 Embankment nodal displacements comparison between FE and ABAQUS model for frequencies (a) *real*(u) at f = 5Hz; (b) *imag*(u) at f = 5Hz; (c) *real*(u) at f = 30Hz; (d) *imag*(u) at f = 30Hz

5.4.2 Model validation 2

Following the validation of the FE track model, the next step is to couple the track model with the subgrade using the methodology proposed and presented in the aforementioned section. To show the verification of the coupling between FE model and BE-TLM model, nodal dispalcements are computed and compared against the ABAQUS model. Once the displacements are known, it is only a trivial step to obtain corrresponding strains and stresses. The problem consists of a slab track resting on a homogenous half-space, with two static point loads vertically applied on the surface (see Figure 5.9). The slab is 2m wide, 0.3m thick and the two point loads are applied at 0.2m away from either edge. The mechanical properties of slab and subgrade can be found in Table 5.3.

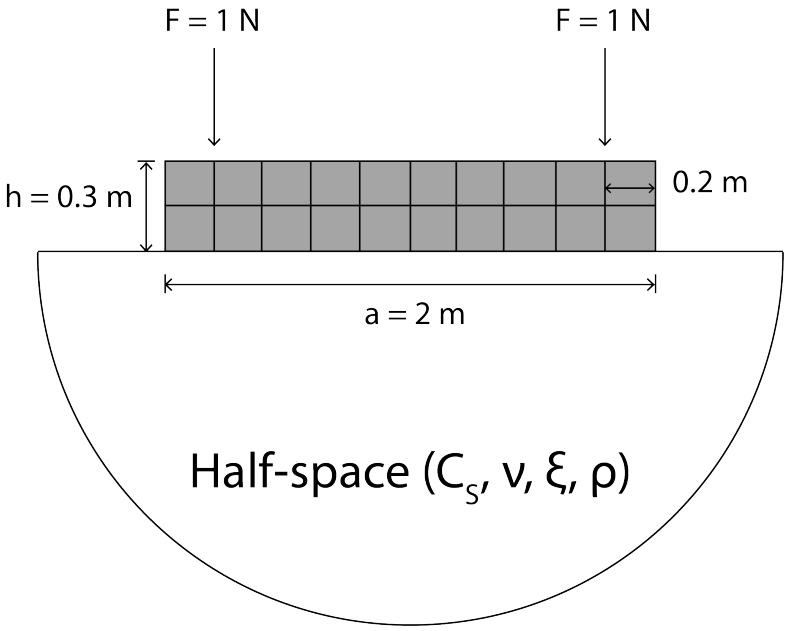

Fig. 5.9 Schematic representation of the slab-subgrade model

Table 5.3 Properties of the slab and subgrade for model 2

Slab			
Density (kg/m^3)	2400	Young's modulus (MPa)	20000
Poisson's ratio	0.2	Damping ratio	0.01
Width (m)	2	Thickness (m)	0.3
Subgrade			
Density (kg/m^3)	2000	Poisson's ratio	0.35
Damping ratio	0.03	Young's modulus (MPa)	64

The slab is modelled by 10 (horizontal) $\times$ 2 (vertical) 8-node quadratic finite elements with the same size. Interface nodes on the bottom of the slab are used for the coupling with BEM-TLM ground model. The homogeneous half-space is represented by the thin-layer model. Again, in order to check the performance of the coupled model, FE tests are conducted by ABAQUS. The slab is fully coupled to a 3D soil model with x,y,z dimensions: 40m $\times$ 20m $\times$ 10m, which uses infinite element absorbing boundaries to reduce wave reflections. The parameters of the soil and slab are the same as in Table 5.3.

To show the 2.5D FEM-BEM-TLM model is capable of accurately computing the track response, nodal displacements of the slab are compared against values obtained from ABAQUS under two different excitation frequencies, i.e., f = 5Hz and 30Hz. The nodal displacements of the FE domain are recorded in the same way as described in the last section. The comparisons for both real and imaginary parts are displayed in Figure 5.10 and Figure 5.11. It can be seen that the computed displacements match well with the corresponding ABAQUS results for both frequencies.

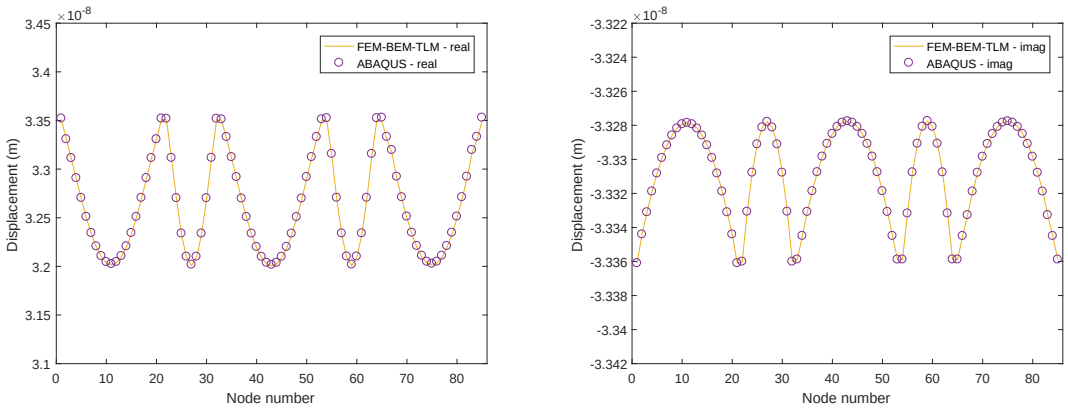

(a) (b)

Fig. 5.10 Slab nodal displacements comparison between 2.5D FEM-BEM-TLM and ABAQUS model at f = 5Hz (a) *real*(u) (b) *imag*(u)

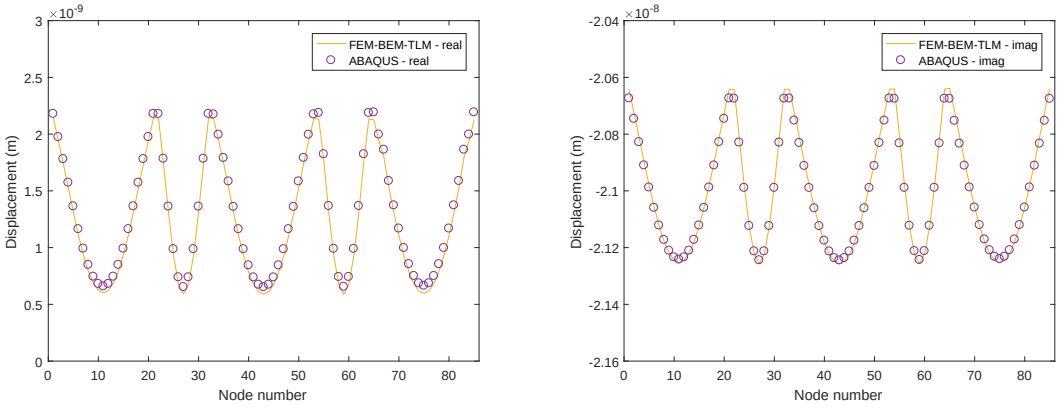

(a) (b)

Fig. 5.11 Slab nodal displacements comparison between 2.5D FEM-BEM-TLM and ABAQUS model at f = 30Hz (a) *real*(u) (b) *imag*(u)

5.4.3 Model validation 3

In the previous two sections, nodal displacements induced by the static unit load are validated respectively against ABAQUS results. To validate the coupled 2.5D FEM-BEM-TLM model under the moving load, the results from the work of Chen et al. [32] are used and the stress components inside the soil layer are calculated and compared. The benchmark problem consists of an Euler beam resting on a homogenous half-space, traversed by a 160kN moving vertical load at 30m/s (see Figure 4.3). The beam is 4m wide, 0.3m thick and infinite in the direction of vehicle travel. Stresses are monitored at 2m directly below the soil surface, at the central line of the Euler beam. It is the same validation used in Chapter 4, hence the schematic illustration of the problem and the material properties of the beam and soil can be found in Figure 4.3 and Table 4.1, respectively.

The stress time histories obtained from both TLM and 2.5D FEM-BEM-TLM models are compared against the published data from Chen et al. [32]. The differences between TLM and 2.5D FEM-BEM-TLM lay in the modelling technique of the beam and the coupling between track and soil. In the TLM model, the beam is modelled analytically and the coupling is achieved by the use of equivalent stiffness, whereas the beam is modelled by finite elements and the coupling is completed by boundary element method in the proposed FEM-BEM-TLM model.

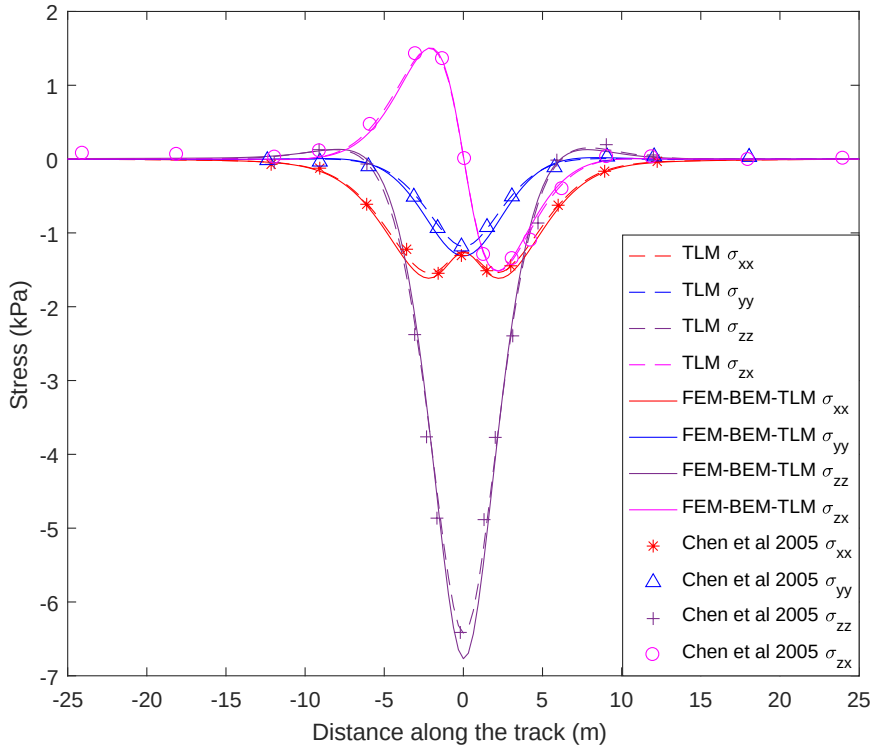

Fig. 5.12 Schematic representation of the slab-subgrade model

The comparison is shown in Figure 5.12 and strong agreement is seen between results with respect to both shape and magnitude. It is worth mentioning that small discrepancies are observed between the 2.5D FEM-BEM-TLM model and TLM/Chen et al. models' result. The reason is that the coupling used for 2.5D FEM-BEM-TLM model is strong as it takes into account the responses from all directions, however both TLM and Chen et al.'s model apply relaxed coupling condition to the interface, meaning only the vertical response (the most dominant) is considered. Even though the dynamic responses are well predicted by applying the relaxed coupling technique (Kaynia et al. [100], Madshus and Kaynia [128], Chen et al. [32], Bian and Chen [18], Thompson [166], Alves Costa et al. [5] and Mezher et al. [133]), a strong coupling will make the model more accurate and robust for more sophisticated tasks.

5.5 Numerical analysis

Increasing demand from commuters and industry has witnessed faster and heavier trains been introduced. Meanwhile, it also requires extra scrutiny over the track structure and supporting subgrade to ensure the operation safety. For instance, adding freight train services to tracks that have previously only been used for

passenger services is an effective way to add additional capacity to exisiting railway lines. However, freight trains subject railway tracks to heavy axle loads which result in elevated strains within the supporting track and subgrade. High-speed trains can also lead to upraised strains. Large strains cause non-linear material behavior, resulting in reduced stiffness (Dong et al. [52]).

In the previous chapters, linear track and subgrade model and non-linear subgrade model have been extensively studied. In order to also investigate the effect of fully non-linear material behaviour on the track responses, two case studies, i.e., freight train and high-speed train, are undertaken with the use of 2.5D FEM-BEM-TLM model. To account for non-linear material effect, the shear modulus degradation and damping ratio curves are used for both track and subgrade. The updating curves for soil are based on the functions proposed by Ishibashi and Zhang [87], where plasticity index (PI) is assumed to be 30 for all soils in this case. A thorough explanation is given in Chapter 4. The stiffness and damping updating curves for track are adopted from the recent laboratory test from Dyvik and Kaynia [54], with details been explained in Section 5.3.

The aim of this section is to shed light upon the effect of adding track material (ballast/subballast) non-linearity on the induced track responses. Therefore, only an embankment is used in the case studies to represent the ballast/subballast and the effect of different soil stiffness's and layering combinations will not be discussed here. As depicted in Figure 5.13, the train-embankment-ground model contains an embankment resting on top of the homogeneous/layered half-space with concentrated moving forces acting on the embankment. Assuming the load is at the centre of the embankment at the beginning, then it will move along the central line with a certain speed.

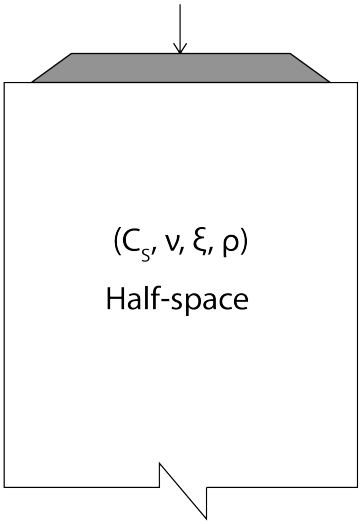

Fig. 5.13 Schematic representation of the train-embankment-ground model

Key embankment and ground properties related to the case studies are listed in Table 5.4, while the load information for freight train and high-speed train is given in Table 5.5.It should be noted that an adjusted load is used in the case study because the load applied on the ballast is not the same as the axle load on the rail due to the reduced pressure on the foundation. The pressure distribution at the ballast-sleeper interface of railroad track plays a key role in overall track support. According to a number of experiments and research work conducted in the past (Tzanakakis [168], McHenry [131], and Watts [175]), the ballast on which the wheel is standing usually takes up to 40% of the wheel load. For instance, the typical axle loads for freight trains in US are between 26 and 30 tonnes (Dong et al. [52]), hence 28 tonnes load is adopted for the load in this research, meaning the actual load acting on the ballast is 11.2 tonnes. Similarly, the adjusted load for high-speed train is 7.2 tonnes.

Table 5.4 Properties of the embankment

Embankment			
Density (kg/m^3)	1900	Young's modulus (MPa)	200
Poisson's ratio	0.35	Damping ratio	0.03
Upper width (m)	3	Lower width (m)	5
Thickness (m)	0.3		
Subgrade			
Density (kg/m^3)	1800	Young's modulus (MPa)	65
Poisson's ratio	0.35	Damping ratio	0.03
Thickness (m)	∞		

Table 5.5 Load information for the case study

Indicative vehicle	Axle load (tonnes)	Speed (km/h)	Alxe spacing (m)
Freight train (US)	11.2	85	4
TGV/Eurostar	7.2	310	3

A variety of output variables are plotted against the non-linear subgrade model to look into the effect of full material non-linearity on the track and soil responses. The non-linear subgrade model is obtained by only updating the ground of the proposed 2.5D FEM-BEM-TLM model.

5.5.1 Case study 1 - Freight train

Figure 5.14a shows the variation of strain versus depth within the soil from both models. It is observed that the maximum strain level is found approximately 1m below the ground surface and decays rapidly with depth. However, for the non-linear track and soil model, the maximum octahedral strain (8.1×10^{-4}) is 18.1% higher than that of non-linear soil model (6.8×10^{-4}). It indicates the effect of non-linear track structure on the soil response, i.e., the reduced track stiffness results in larger soil response. Correspondingly, the resulting reduction in stiffness (Young's modulus) with depth is shown in Figure 5.14b. When considering only linear relationship, stiffness is constant with depth, however after strain updating, the subsequent non-linear model

shows large variations with depth, all of which are lower than the starting value, particularly near the soil surface. It matches with the variation of strains within the soil.

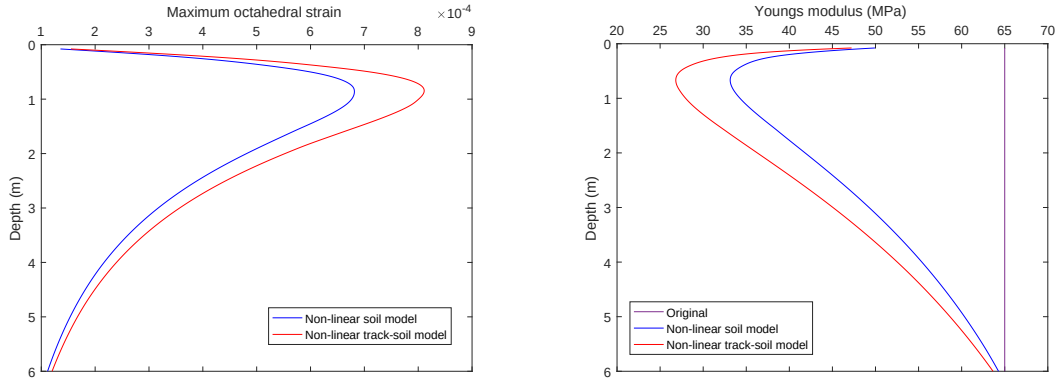

(a) (b)

Fig. 5.14 Comparisons between non-linear subgrade and non-linear track-subgrade model (a) Octahedral strain vs depth (b) Young's modulus reduction with depth

Figure 5.15 displays the ballast deflections during the passage of freight train in both time and frequency domains. It should be noted that the track response in the presented case studies is recorded at the surface of the ballast. For the non-linear subgrade model, the resulting maximum displacement in the time domain is 6.9mm, however for the non-linear track and subgrade model, the corresponding displacement is 7.7mm. Therefore, it can be seen that the use of non-linear subgrade model might underestimate track structure deflections. Similar conclusions can be drawn on the ballast velocity from Figure 5.16. In addition, it is interesting to note that as the material stiffness decreases, dynamic effects become more prevalent, with ballast displacements appearing less symmetric.

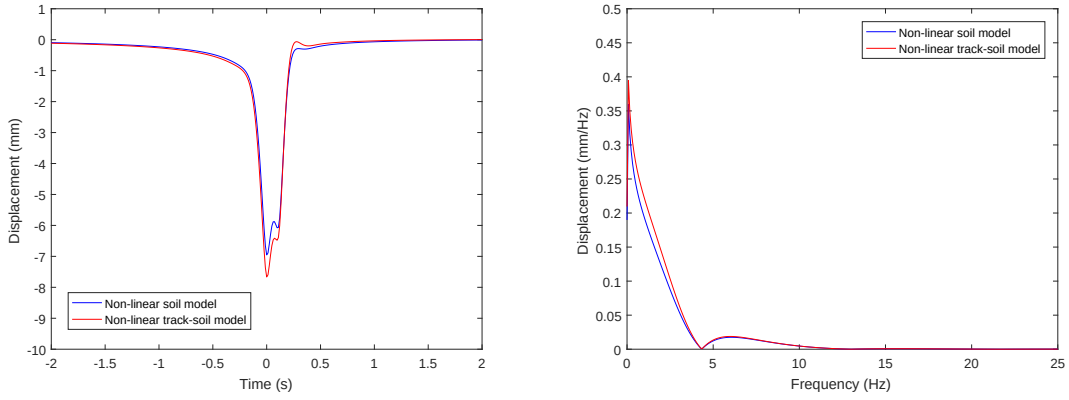

(a) (b)

Fig. 5.15 Track displacements due to the passage of freight train in (a) time domain (b) frequency domain

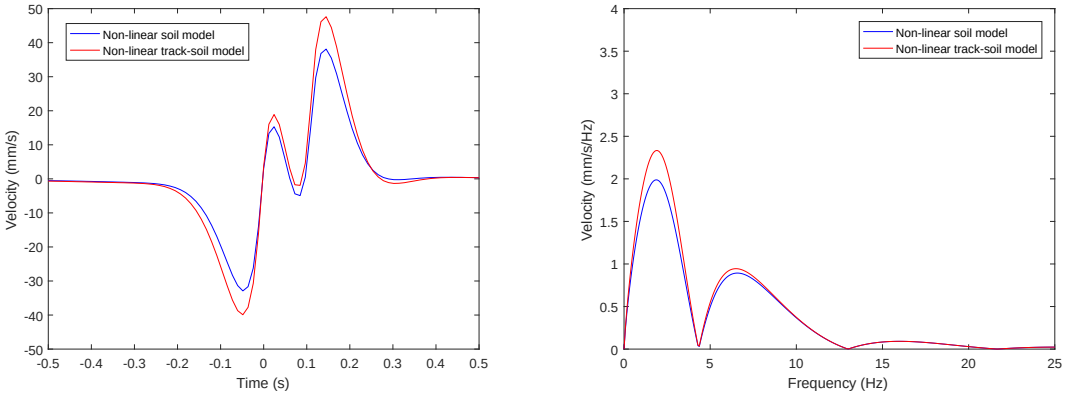

(a) (b)

Fig. 5.16 Track velocities due to the passage of freight train in (a) time domain (b) frequency domain

In the end, it is of interest to take a look at the strain variations inside the track structure because it directly relates to shear modulus degradation levels. Figure 5.17 shows the strain variations inside the ballast when considering material non-linearity. Clearly, the strain levels are higher when non-linear material is considered and it also shows an expansion to a more global area in the track structure after iterative material property upating. It is of great importance because elevated strain levels lead to greater track degradation.

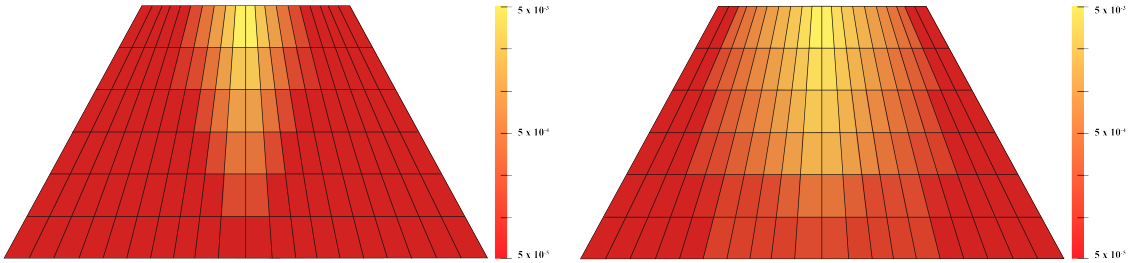

(a) (b)

Fig. 5.17 (a) Linear track strain variations (b) Non-linear track strain variations

5.5.2 Case study 2 - High-speed train

In comparison to freight trains, the alxe loads for high-speed trains are much lower. But elevated track and subgrade strains can be induced as the train speed increases, hence resulting in non-linear material behaviour.

Figure 5.18a shows the variation of strain versus depth within the soil from both models. When considering full material non-linearity (both track and soil), the maximum octahedral strain reaches 10.4×10^{-4} at 1m depth. The corresponding result for taking into consideration the soil non-linearity is 8.0×10^{-4}. Correspondingly, the resulting reduction in stiffness (Young's modulus) with depth is shown in Figure 5.18b. Similar to the previous case, both non-linear models show large stiffness variations with depth, particularly

close to the soil surface. Comparing to the original soil stiffness, the lowest stiffness values for non-linear track-soil and non-linear soil models are 23.6MPa and 31.2MPa, respectively, indicating a decrease of 64.5% and 52.3% in the result from the original value.

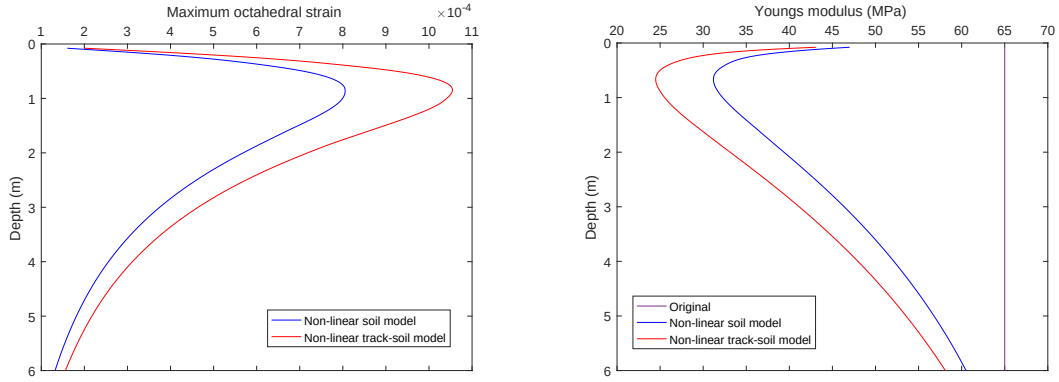

(a) (b)

Fig. 5.18 Comparisons between non-linear subgrade and non-linear track-subgrade model (a) Octahedral strain vs depth (b) Young's modulus reduction with depth

Figure 5.19 displays the ballast deflections during the passage of high-speed train in both time and frequency domains. The resulting maximum displacement in time domain is 5.8mm for non-linear track-soil model. However if applying only non-linear soil model, the corresponding displacement is 5.0mm, which is 16% lower than that of non-linear track-soil model. Similarly, the resulting maximum velocity from non-linear track-soil model (as shown in Figure 5.20) is 27% higher than the corresponding result from the non-linear soil model. It indicates that the track material non-linearity can make a difference when suffering elevated strains inside the structure.

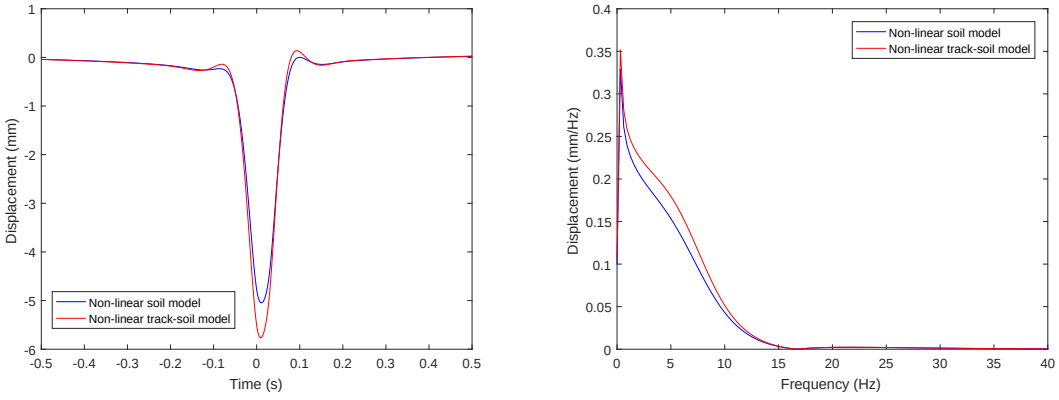

(a) (b)

Fig. 5.19 Track displacements due to the passage of high-speed train in (a) time domain (b) frequency domain

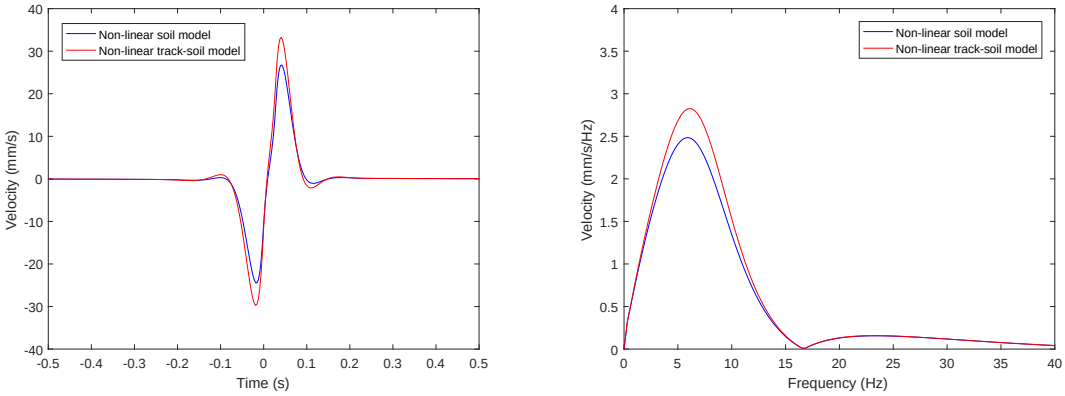

(a) (b)

Fig. 5.20 Track velocities due to the passage of high-speed train in (a) time domain (b) frequency domain

5.6 Discussion

The two case studies presented show that full material non-linearity has a noticeable effect on track-ground response during train passage. Table 5.6 summarizes the results and shows that the track deflections can increase when applying full material non-linearity.

Table 5.6 quantifies the differences between track-ground responses computed using non-linear soil model and fully non-linear track-soil model. It reveals that the inclusion of the track non-linearity when large strains occur will lead to increased strains and correspondingly decreased stiffness in the soil. The discrepancies between soil strains computed by partly non-linear and fully non-linear models can be up to 29.5% and the corresponding track displacement discrepancy reaches 16.0%. The findings show the importance of utilising full material non-linearity to study the track-ground response subject to large induced strains.

It also should be mentioned that this research presents a numerical model to deepen the understanding of the material non-linearity effect on the track response. The results are obtained from a basic track-embankment-ground model and are for two single wheels passage with adjusted load values. As explained in Chapter 4, the track-ground behaviour can be affected by the properties and layings of ground and vehicle axle configuration. Therefore, in the future, these factors should be included when investigating the full material non-linearity in practice.

Table 5.6 Summary of effect of full material non-linearity on track-ground responses

	Young's modulus		Soil strain	track deflection
	Percentage decrease from NSM	Percentage decrease from original value	Percentage increase from NSM	Percentage increase from NSM
Case 1	23.6%	60.5%	18.1%	11.6%
Case 2	25.2%	64.5%	29.5%	16.0%

Note: NSM - Non-linear soil model

5.7 Conclusion

This chapter presents a novel frequency domain 2.5D FEM-BEM-TLM model to include the effect of full material non-linearity on the track response from passage of vehicles. The model combines FEM track structure and BEM-TLM soil model, where the Green's functions are computed by the thin-layer approach. The model is coupled with a 'linear equivalent' formulation to allow both the track and soil stiffness to change depending upon strain level. The model is validated against the results from the commercial FE software ABAQUS and an embankment-ground case is validated using an independently published dataset. The purpose of this work is to use the 2.5D FEM-BEM-TLM model to look into the track-ground response variations when considering full material non-linearity. The model is used to investigate two cases, i.e., freight train and high-speed train. It is found that the inclusion of ballast non-linearity has a noticeable influence on the track-ground response. For example, the ballast displacements can be up to 16.0% of the case in which only soil non-linearity is considered. The results vary with different material properties, however, this work provides a novel way to gain insights on the effects of full material non-linearity in railway simulation.

Chapter 6

Conclusions and recommendations for future work

6.1 Conclusions

The main objective of this work is to develop numerical tools that allow analysing track behaviour efficiently, investigating material non-linearity effect on the track dynamics and also assessing the soil remediation strategies. Three different models are proposed in Chapter 3, Chapter 4 and Chapter 5 to address the objectives of this research and provide reliable predictions for the track and soil behaviour.

Fully linear track and subgrade model

First of all, a semi-analytical approach that combines the analytical track model and linear TLM soil model is developed to simulate the track response over a range of speeds efficiently and accurately. The subgrade is discretized into a finite number of thin layers along the vertical direction with the infinite and homogeneous properties along the horizontal plane. In the track solution, the discrete elements (such as sleepers and railpads) are modelled through an equivalent continuous formulation. This simplification has a huge advantage in terms of mathematical formulation because the model becomes invariant in the direction of rail road. Both sub-models are developed in the wavenumber-frequency domain and the coupling is also performed in the wavenumber-frequency domain, using the complex equivalent stiffness and relaxed boundary conditions between the track and soil.

Validation was performed using a combination of field experimental data and published numerical results, and the model found to provide high accuracy. To address the soil mitigation strategies used in the design and construction of new railway lines, three different earthwork situations are considered and assessed for both ballasted and slab tracks. It is found that the relationship between improvement depth and rail displacement can be highly non-linear and hence soil improvement must be designed carefully to achieve the desired track performance.

Non-linear subgrade model

Subsequently, an equivalent linear TLM soil model is then proposed to couple with the exisitng analytical track solution to account for non-linear stiffness and damping behaviour caused by the large strains induced in the soil. An iterative 'equivalent linear' procedure that uses strain magnitude and degradation curve data to automatically adjust material stiffness and damping based upon strain levels is introduced. It accounts for the material (soil) non-linearity by updating the material properties iteratively until the convergence is reached. Similar to the linear model described previously, the track is modelled analytically and the soil is modelled by the thin-layer element method in the wavenumber-frequency domain.

The linear stress-strain implementation is validated using an independently published dataset and the non-linear response is validated using field data collected on a high-speed railway line. Good matches have been achieved from both validations. The model is used to investigate four railway case studies, each with highly contrasting subgrade characteristics. It is found that non-linearity has a significant influence on track-ground response, especially when the soil layer is soft. The critical velocity tends to shift towards a lower value and the dynamic amplification is more obvious when taking into account of the soil non-linearity. It is of great importance for new railway line design.

Fully non-linear track and subgrade model

In the end, a fully non-linear track and subgrade model is proposed to assess the material non-linearity effect. It capitalises on the 2.5D FEM-BEM model and then incorprates the TLM model for the computation of the soil response. 2.5D FEM is used to build track structure and 2.5D BEM-TLM is formulated to represent the soil response, where the coupling between the track and soil occurs on the interface of two domains. The strong coupling technique is applied in the model, meaning the coupling takes into consideration of the response from all directions. The proposed 'equivalent linear' approach is used for both track and soil to automatically adjust material stiffness and damping based upon strain levels.

The model is validated with the results from FE commercial software ABAQUS and published work. In order to gain an insight on the effect of track non-linearity, an embankment is designed to lay on top of a homogeneous half-space and two types of loads (i.e., freight train and high-speed train) are used to complete the case studies. It shows that the track experiences a noticeable non-linear behvaiour when large strains occur in the track structure.

It needs to be stressed that the above-mentioned models are developed based on the following assumptions:

1. **Linear elastic behaviour of the material** - it should be noted that the proposed non-linear model is based on equivalent linear approach and it still assumes the linear elastic material properties.

2. **Constant speed of the vehicle** - all the simulations are completed with the loads moving at constant speed.

3. **Horizontally stratified soil** - this assumption is commonly used in the literature, and allows the soil to be simulated with the thin-layer method and also the boundary element method.

6.2 Recommendations for future work

Some suggestions for future work are proposed in this section in terms of improvements to the model and other applications.

Fully non-linear track and subgrade model with complete track structure

In Chapter 5, a novel 2.5D FEM-BEM-TLM is proposed, validated and used to investigate an embankment/beam overlaying on top of homogeneous and layered half-space. It is used to shed lights on the track non-linearity effect on the dynamic response induced by the train passage. However, the model will be more powerful if a complete track structure (i.e., rail, railpad, sleeper, ballast/subballast etc) can be also included and validated. It will allow for a better understanding of the material non-linearity effect in practice.

Dynamic load contribution inclusion

All the proposed models consider quasi-static contribution from the moving loads in this research work. It has shown to be effective when studying the track response or the soil response close to the track structure. However, to investigate the vibrations induced in the near-field region (away from the track), dynamic load

contribution needs to be applied. Therefore, a further improvement of the model can be achieved by adding the dynamic contribution of the loads.

Asphalt track analysis

Asphalt track is considered as an effective and cost-friendly way to reduce the vibrations induced by the train passage. Comparing to the conventional ballasted track, asphalt track has an extra asphalt layer inserted above or under the ballast layer. The asphalt possesses similar characteristics to slab track. More importantly, the asphalt is more consistent in terms of properties and it suits well with the proposed thin-layer method. It will be interesting to investigate the mitigation effect of the asphalt by adding it to the existing models and analyse the effects of different parameters of asphalt for the best mitigation strategy.

Slab track data collection and validation

Most of the on-site data is collected for ballasted rail tracks, however, there is lack of data for the slab track. Nowadays, the benefits of slab track have made it a popular choice for the construction of new railway lines. It would be ideal if some on-site data can be collected from slab tracks and then used to validate the proposed model. In this work, slab track was modelled through an analytical approach and also the 2.5D FEM-BEM-TLM model can also be used for the slab track modelling. It would be interesting to compare the numerical results against experimental testing.

References

[1] Alves Costa, P. (2011). Vibrações do sistema via-maciço induzidas por tráfego ferroviário. Modelação numérica e validação experimental. University of Porto, Faculty of Engineering.

[2] Alves Costa, P., Calçada, R., and Cardoso, A. (2012). Track–ground vibrations induced by railway traffic: In-situ measurements and validation of a 2.5D FEM-BEM model. *Soil Dynamics and Earthquake Engineering*, 32:111–128.

[3] Alves Costa, P., Calçada, R., Cardoso, A., and Bodare, A. (2010a). Influence of soil non-linearity on the dynamic response of high-speed railway tracks. *Soil Dynamics and Earthquake Engineering*, 30:221–235.

[4] Alves Costa, P., Calçada, R., Marques, J., and Cardoso, A. (2010b). A 2.5D finite element model for simulation of unbounded domains under dynamic loading. *Numerical Methods in Geotechnical Engineering*, pages 397–404.

[5] Alves Costa, P., Colaço, A., Calçada, R., and Cardoso, A. (2014). Critical speed of railway tracks. detailed and simplified approaches. *Transportation Geotechnics*, 2:30–46.

[6] Alves Costa, P., Lopes, P., and Cardoso, A. (2018). Soil shakedown analysis of slab railway tracks: Numerical approach and parametric study. *Transportation Geotechnics*, 16:85–96.

[7] Anastasopoulos, I., Alfi, S., Gazetas, G., Bruni, S., and Van Leuven A, a. (2009). Numerical and experimental assessment of advanced concepts to reduce noise and vibration on urban railway turnouts. *Journal of Transportation Engineering*, 135:279–287.

[8] Andersen, L. (2007). Linear elastodynamic analysis. *Aalborg: Aalborg University*.

[9] Anderson, W. and Fair, P. (2008). Behavior of railroad ballast under monotonic and cyclic loading. *Journal of Geotechnical and Geoenvironmental Engineering*, 134:316–327.

[10] Arlaud, E., Costa D'aguiar, S., and Balmes, E. (2014). Validation of a reduced model of railway track allowing long 3D dynamic calculation of train-track interaction. pages 1193–1198.

[11] Arlaud, E., Costa D'Aguiar, S., and Balmes, E. (2016). Receptance of railway tracks at low frequency: Numerical and experimental approaches. *Transportation Geotechnics*, 9:1–16.

[12] Auersch, L. (2005). The excitation of ground vibration by rail traffic: Theory of vehicle-track-soil interaction and measurements on high-speed lines. *Journal of Sound and Vibration*, 284:103–132.

[13] Auersch, L. (2006). Ground vibration due to railway traffic - The calculation of the effects of moving static loads and their experimental verification. *Journal of Sound and Vibration*, 293:599–610.

[14] Aursudkij, B., R. McDowell, G., and Collop, A. (2009). Cyclic loading of railway ballast under triaxial conditions and in a railway test facility. *Granular Matter*, 11:391–401.

[15] Banimahd, M., Woodward, P., Kennedy, J., and Medero, G. (2011). Behavior of train-track interaction in stiffness transitions. *Proceedings of the ICE - Transport*, 165:205–214.

[16] Barbosa, J., Park, J., and A. Kausel, E. (2012). Perfectly matched layers in the thin layer method. *Computer Methods in Applied Mechanics and Engineering*, s 217–220:262–274.

[17] Barkan, D. (1962). Dynamics of bases and foundations. *New York: McGraw-Hill Book Company, Inc*.

[18] Bian, X. and Chen, Y. (2006). An explicit time domain solution for ground stratum response to harmonic moving load. *Acta Mechanica Sinica*, 22:469–478.

[19] Bian, X., Chen, Y., and Hu, T. (2008). Numerical simulation of high-speed train induced ground vibrations using 2.5D finite element approach. *Science in China Series G Physics Mechanics and Astronomy*, 51:632–650.

[20] Bian, X., Cheng, C., Jiang, J., Chen, R., and Chen, Y. (2014). Numerical analysis of soil vibrations due to trains moving at critical speed. *Acta Geotechnica*, 11:281–294.

[21] Bian, X. and Hu, T. (2007). Parametric study on embankment-ground vibrations generated by train moving loads. *Chinese Journal of Rock Mechanics and Engineering*, 26:4353–4361.

[22] Bian, X., Jiang, H., and Chen, Y. (2010). Accumulative deformation in railway track induced by high-speed traffic loading of the trains (in Chinese). *Earthquake Engineering and Engineering Vibration*, 9:319–326.

[23] Bian, X. C., Chao, C., Jin, W. F., and Chen, Y. M. (2011). A 2.5D finite element approach for predicting ground vibrations generated by vertical track irregularities. *Journal of Zhejiang University SCIENCE A*, 12:885–894.

[24] Bierer, T. and Bode, C. (2007). A semi-analytical model in time domain for moving loads. *Soil Dynamics and Earthquake Engineering*, 27:1073–1081.

[25] Bode, C., Hirschauer, R., and A. Savidis, S. (2002). Soil–structure interaction in the time domain using halfspace Green's functions. *Soil Dynamics and Earthquake Engineering*, 22:283–295.

[26] Bogacz, R., Krzyýski, T., and Popp, K. (1989). On the generalization of mathews' problem of the vibrations of a beam on elastic foundation. *Zamm-zeitschrift Fur Angewandte Mathematik Und Mechanik*, 69:243–252.

[27] Bose, T., Choudhury, D., Julian Sprengel, J., and Ziegler, M. (2018). Efficiency of open and infill trenches in mitigating ground-borne vibrations. *Journal of Geotechnical and Geoenvironmental Engineering*, 144:1–13.

[28] Cai, Z. and Raymond, G. (1992). Theoretical model for dynamic wheel/rail and track interaction. In *10th International Wheelset Congress: Sharing the latest wheelset technology in order to reduce costs and improve railway productivity*, pages 127–131.

[29] Carne, M. (2018). Network Rail Limited annual report and accounts 2018. *Government Publications*.

[30] Chebli, H., Clouteau, D., and Schmitt, L. (2008a). Dynamic response of high-speed ballasted railway tracks: 3D periodic model and in situ measurements. *Soil Dynamics and Earthquake Engineering*, 28:118–131.

[31] Chebli, H., Othman, R., Clouteau, D., Arnst, M., and Degrande, G. (2008b). 3D periodic BE–FE model for various transportation structures interacting with soil. *Computers & Geotechnics*, 35:22–32.

[32] Chen, Y., Wang, C., Chen, Y., and Zhu, B. (2005). Characteristics of stresses and settlement of ground induced by train. *Environmental vibrations: Prediction, monitoring, mitigation and evaluation: Proceedings of the International symposium on environmental Vibrations*, pages 33–42.

[33] Cheng, H., Nakata, Y., and Bolton, M. (2003). Discrete element simulation of crushable soil. *Géotechnique*, 53:633–641.

[34] Chua, D., W. Lo, K., and Balendra, T. (1995). Building response due to subway train traffic. *Journal of Geotechnical Engineering*, 121:740–747.

[35] Connolly, D., Giannopoulos, A., Fan, W., Woodward, P., and Forde, M. (2013a). Optimising low acoustic impedance back-fill material wave barrier dimensions to shield structures from ground borne high speed rail vibrations. *Construction and Building Materials*, 44:557–564.

[36] Connolly, D., Giannopoulos, A., and Forde, M. (2013b). Numerical modelling of ground borne vibrations from high speed rail lines on embankments. *Soil Dynamics and Earthquake Engineering*, 46:13–19.

[37] Correia, A. and Cunha, J. (2014). Analysis of nonlinear soil modelling in the subgrade and rail track responses under HST. *Transportation Geotechnics*, 1:147–156.

[38] Correia, A., Hornych, P., and Akou, Y. (1999). Review of models and modelling of unbound granular materials. *Workshop on Modelling and Advanced Testing for Unbound Granular Materials, IST, Lisbon, Portugal, 1999*, pages 3–15.

[39] Cunha, J. and Correia, A. (2014). Importance of non-linear soil behaviour on modelling rail track response. *Civil-Comp Proceedings*, 104:1–10.

[40] Datoussaid, S., De Saedeleer, B., Verlinden, O., and Conti, C. (2000). Vehicle-track interaction and ground propagation of vibrations for urban railway vehicles. *European Journal of Mechanical and Environmental Engineering*, 45:87–93.

[41] De Barros, F. and Luco, J. (1995). Stresses and displacements in a layered half-space for a moving line load. *Applied Mathematics and Computation*, 67:103–134.

[42] Degrande, G. and Lombaert, G. (2001). An efficient formulation of Krylov's prediction model for train induced vibrations based on the dynamic reciprocity theorem. *The Journal of the Acoustical Society of America*, 110:1379–90.

[43] Degrande, G., Schevenels, M., Chatterjee, P., Velde, W., Hölscher, P., Hopman, V., Wang, A., and Dadkah, N. (2006). Vibrations due to a test train at variable speeds in a deep bored tunnel embedded in London clay. *Journal of Sound and Vibration*, pages 626–644.

[44] Dieterman, H. and Metrikine, A. (1996). Equivalent stiffness of a half-space interacting with a beam: Critical velocities of a moving load along the beam. *European Journal of Mechanics. A. Solids*, 15:67–90.

[45] Dieterman, H. and Metrikine, A. (1997). Steady-state displacements of a beam on an elastic half-space due to a uniformly moving constant load. *European Journal of Mechanics, A/Solids*, 16:295–306.

[46] Dimitrovová, Z. and Varandas, J. (2009). Critical velocity of a load moving on a beam with a sudden change of foundation stiffness: Applications to high-speed trains. *Computers & Structures*, 87:1224 – 1232.

[47] Dong, K., Connolly, D., Laghrouche, O., Woodward, P., and Alves Costa, P. (2017a). Earthwork strategies to reduce dynamic amplification on new high-speed rail lines. In *International Railway Conference, Edinburgh*.

[48] Dong, K., Connolly, D., Laghrouche, O., Woodward, P., and Alves Costa, P. (2018a). The effect of non-linear soil behavior on mixed traffic railway lines. In *Numerical Methods in Geotechnical Engineering IX*, volume 2, pages 1445–1449.

[49] Dong, K., Connolly, D., Laghrouche, O., Woodward, P., and Alves Costa, P. (2018b). Non-linear soil behavior on freight and passenger lines. In *WIT Transactions on the Built Environment*, pages 507–516.

[50] Dong, K., Connolly, D., Laghrouche, O., Woodward, P., and Alves Costa, P. (2018c). The stiffening of soft soils on railway lines. *Transportation Geotechnics*, 17:178–191.

[51] Dong, K., Connolly, D., Laghrouche, O., Woodward, P., and Alves Costa, P. (2019). Non-linear soil behaviour on high speed rail lines. *Computers & Geotechnics*, 112:302–318.

[52] Dong, K., Connolly, D., Laghrouche, O., Woodward, P., Ho, C., and Alves Costa, P. (2018d). The effect of soil non-linearity on mixed traffic railway lines: Passenger vs Freight loads. In *Proceedings of*

GeoShanghai 2018 International Conference: Transportation Geotechnics and Pavement Engineering, pages 227–236.

[53] Dong, K., Connolly, D., Laghrouche, O., Woodward, P., Pombo, J., and Alves Costa, P. (2017b). Optimising ground improvement on new high speed rail lines. In *Stephenson Conference, London*.

[54] Dyvik, R. and Kaynia, A. (2018). Large-scale triaxial tests on railway embankment material. *Railroad Ballast Testing and Properties*, pages 173–190.

[55] Eason, G. (1965). The stresses produced in a semi-infinite solid by a moving surface force. *International Journal of Engineering Science*, 2:581–609.

[56] Ekanayake, S., Liyanapathirana, D., and Leo, C. (2014). Attenuation of ground vibrations using in-filled wave barriers. *Soil Dynamics and Earthquake Engineering*, 67:290–300.

[57] Ekevid, T. and Wiberg, N.-E. (2002). Wave propagation related to high-speed train: A scaled boundary FE approach for unbounded domains. *Computer Methods in Applied Mechanics and Engineering*, pages 3947–3964.

[58] El Kacimi, A., Woodward, P., Laghrouche, O., and Medero, G. (2013). Time domain 3D finite element modelling of train-induced vibration at high speed. *Computers & Structures*, 118:66–73.

[59] Çelebi, E. and Goktepe, F. (2012). Non-linear 2D FE analysis for the assessment of isolation performance of wave impeding barrier in reduction of railway-induced surface waves. *Construction and Building Materials*, 36:1–13.

[60] Çelebi, E. and Kırtel, O. (2013). Non-linear 2D FE modeling for prediction of screening performance of thin-walled trench barriers in mitigation of train-induced ground vibrations. *Construction and Building Materials*, 42:122–131.

[61] Feng, S., Li, Y., Chen, Z., and Chen, H.-X. (2017a). Response of railway track coupled with a stratified ground consisting of saturated interlayer to high-speed moving train load. *Soil Dynamics and Earthquake Engineering*, 102:25–40.

[62] Feng, S., Zhang, X., Zheng, Q.-T., and Wang, L. (2017b). Simulation and mitigation analysis of ground vibrations induced by high-speed train with three dimensional FEM. *Soil Dynamics and Earthquake Engineering*, 94:204–214.

[63] Ferreira, P. and Pita, A. (2015). Numerical modelling of high speed train/track system for the reduction of vibration levels and maintenance needs of railway tracks. *Construction and Building Materials*, 79:14–21.

[64] François, S., Schevenels, M., Galvín, P., Lombaert, G., and Degrande, G. (2010). A 2.5D coupled FE–BE methodology for the dynamic interaction between longitudinally invariant structures and a layered halfspace. *Computer Methods in Applied Mechanics and Engineering*, pages 1536–1548.

[65] Fryba, L. (1972). Vibration of solids and structures under moving loads. *Nethelands: Springer*.

[66] Fujii, K. and Takei, Y. (2005). Propagation properties of train-induced vibration from tunnels. *Quart Report of RURI*, 46:194–199.

[67] Galvín, P. and Dominguez, J. (2007). Analysis of ground motion due to moving surface loads induced by high-speed trains. *Engineering Analysis with Boundary Elements*, 31:931–941.

[68] Galvín, P., François, S., Schevenels, M., Bongini, E., Degrande, G., and Lombaert, G. (2010). A 2.5D coupled FE-BE model for the prediction of railway induced vibrations. *Soil Dynamics and Earthquake Engineering*, pages 1500–1512.

[69] Godinho, L., Mendes, P., Pereira, A., and Soares Jr, D. (2013). A coupled MFS–FEM model for 2D dynamic soil–structure interaction in the frequency domain. *Computers & Structures*, 129:74–85.

[70] Godinho, L. and Soares Jr, D. (2013). Frequency domain analysis of interacting acoustic–elastodynamic models taking into account optimized iterative coupling of different numerical methods. *Engineering Analysis with Boundary Elements*, 37:1074–1088.

[71] Grundmann, H. and Lenz, S. (2003). Nonlinear interaction between a moving SDOF system and a Timoshenko beam/halfspace support. *Archive of Applied Mechanics*, 72:830–842.

[72] Gupta, S. and Degrande, G. (2010). Modelling of continuous and discontinuous floating slab tracks in a tunnel using a periodic approach. *Journal of Sound and Vibration*, 329:1101–1125.

[73] Gutowski, T. and Dym, C. (1976). Propagation of ground vibration: A review. *Journal of Sound and Vibration*, 49:179–193.

[74] Hall, L. (2003). Simulations and analyses of train-induced ground vibrations in finite element models. *Soil Dynamics and Earthquake Engineering*, 23:403–413.

[75] Haskell, N. (1953). The dispersion of surface waves in multilayered media. *Bulletin of the Seismological Society of America*, 73:17–43.

[76] Herraiz, J., Morales Ivorra, S., Martin, C., and Basauri, V. (2015). Analysis of vibrations generated by the presence of corrugation in a modeled tram track. *Mathematical Problems in Engineering*, 2015:1–8.

[77] Hicks, R. and Monismith, C. (1971). Factors influencing the resilient response of granular materials. *Transportation Research Record*, 345:14–31.

[78] Hu, J., Bian, X., and Jiang, J. (2016). Critical velocity of high-speed train running on soft soil and induced dynamic soil response. *Procedia Engineering*, 143:1034–1042.

[79] Hung, H. H. and Yang, Y. (2001). Elastic waves in visco-elastic half-space generated by various vehicle loads. *Soil Dynamics and Earthquake Engineering*, 21:1–17.

[80] Hung, H. H. and Yang, Y. (2010). Analysis of ground vibrations due to underground trains by 2.5D finite/infinite element approach. *Earthquake Engineering and Engineering Vibration*, 9:327–335.

[81] Hunt, G. A. (1994). Analysis of requirements for railway construction on soft ground. *Technical Report LR TM 031*.

[82] Indraratna, B., Ionescu, D., and Christie, D. (1998). Shear behavior of railway ballast based on large-scale triaxial tests. *Journal of Geotechnical and Geoenvironmental Engineering*, 124:439–449.

[83] Indraratna, B., Kumar Thakur, P., Vinod, J. S., and Salim, W. (2012). Semiempirical cyclic densification model for ballast incorporating particle breakage. *International Journal of Geomechanics*, 12:260–271.

[84] Indraratna, B., Lackenby, J., and Christie, D. (2005). Effect of confining pressure on the degradation of ballast under cyclic loading. *Géotechnique*, 55:325–328.

[85] Indraratna, B. and Nimbalkar, S. (2013). Stress-strain degradation response of railway ballast stabilized with geosynthetics. *Journal of Geotechnical and Geoenvironmental Engineering*, 139:684–700.

[86] Indraratna, B., Thakur, P., and Vinod, J. S. (2010). Experimental and numerical study of railway ballast behavior under cyclic loading. *International Journal of Geomechanics*, 10:136–144.

[87] Ishibashi, I. and Zhang, X. (1993). Unified dynamic shear moduli and damping ratios of sand and clay. *Soils and foundations*, 33:182–191.

[88] Iwasaki, T., Tatsuoka, F., and Takagi, Y. (1978). Shear moduli of sands under cyclic torsional shear loading. *Soils and foundations*, 18(1):39–56.

[89] Jones, C., Sheng, X., and Petyt, M. (2000). Simulations of ground vibration from a moving harmonic load on a railway track. *Journal of Sound and Vibration*, 231:739–751.

[90] Jones, D. and Petyt, M. (1992). Ground vibration in the vicinity of a strip load: An elastic layer on a rigid foundation. *Journal of Sound and Vibration*, 161:1–18.

[91] Ju, S. and Lin, H.-T. (2004). Analysis of train-induced vibrations and vibration reduction schemes above and below critical Rayleigh speeds by finite element method. *Soil Dynamics and Earthquake Engineering*, 24:993–1002.

[92] Ju, S. H. (2013). 3D analysis of high-speed trains moving on bridges with foundation settlements. *Archive of Applied Mechanics*, 83(2):281–291.

[93] Kalliainen, A., Kolisoja, P., and Nurmikolu, A. (2016). 3D Finite Element model as a tool for analyzing the structural behavior of a railway track. *Procedia Engineering*, 143:820–827.

[94] Karlstroem, A. and Boström, A. (2006). An analytical model for train-induced ground vibrations from railways. *Journal of Sound and Vibration*, 292:221–241.

[95] Kausel, E. (1974). Forced vibrations of circular foundations on layered media. *MIT Report*, R74-11.

[96] Kausel, E. (1981). An explicit solution for the Green Functions for dynamic loads in layered media. *NASA STI/Recon Technical Report N*, 82:1–86.

[97] Kausel, E. (1986). Wave propagation in anisotropic layered media. *International Journal for Numerical Methods in Engineering*, 23:1567 – 1578.

[98] Kausel, E. (1994). Thin-layer method: Formulation in the time domain. *International Journal for Numerical Methods in Engineering*, 37:927 – 941.

[99] Kausel, E. and Roesset, J. M. (1981). Stiffness matrices for layered soils. *Bulletin of the Seismological Society of America*, 71:1743–1761.

[100] Kaynia, A., Madshus, C., and Zackrisson, P. (2000). Ground vibration from high-speed trains: Prediction and countermeasure. *Journal of Geotechnical and Geoenvironmental Engineering - J GEOTECH GEOENVIRON ENG*, 126:531–537.

[101] Kenney, J. (1954). Steady-state vibrations of beam on elastic foundation for moving load. *Journal of Applied Mechanics*, 21:359–364.

[102] Knothe, K. and Grassie, S. (1993). Modelling of railway track and vehicle/track interaction at high frequencies. *Vehicle System Dynamics*, 22:209–262.

[103] Knothe, K. and Wu, Y. (1998). Receptance behaviour of railway track and subgrade. *Archive of Applied Mechanics*, 68:457–470.

[104] Koroma, S., Thompson, D., Hussein, M., and Ntotsios, E. (2017). A mixed space-time and wavenumber-frequency domain procedure for modelling ground vibration from surface railway tracks. *Journal of Sound and Vibration*, 400:508–532.

[105] Kouroussis, G., Connolly, D., Olivier, B., Laghrouche, O., and Alves Costa, P. (2016). Railway cuttings and embankments: Experimental and numerical studies of ground vibration. *Science of The Total Environment*, 557-558:110–122.

[106] Kouroussis, G., Connolly, D., and Verlinden, O. (2014). Railway induced ground vibrations - A review of vehicle effects. *International Journal of Rail Transportation*, 2:69–110.

[107] Kouroussis, G., Connolly, D., Vogiatzis, K., and Verlinden, O. (2015). Modelling the environmental effects of railway vibrations from different types of rolling stock: A numerical study. *Shock and Vibration*, vol. 2015:1–15.

[108] Kouroussis, G., Gazetas, G., Anastasopoulos, I., Verlinden, O., and Conti, C. (2011). Discrete modeling of vertical track–soil coupling for vehicle–track dynamics. *Soil Dynamics and Earthquake Engineering*, 31:1711–1723.

[109] Kramer, S. (1996). Geotechnical earthquake engineering. *Prentice-Hall, Inc*.

[110] Krylov, V. (1994). On the theory of railway-induced ground vibrations. *Journal de Physique IV (Proceedings)*, 04:769–772.

[111] Krylov, V. (1995). Generation of ground vibrations by superfast trains. *Applied Acoustics*, 44:149–164.

[112] Krylov, V. (1996). Vibrational impact of high-speed trains: Effect of track dynamics. *Journal of The Acoustical Society of America*, 100:3121–3134.

[113] Krylov, V. (1998). Effect of track properties on ground vibrations generated by high-speed trains. *Acta Acustica united with Acustica*, 84:78–90.

[114] Lackenby, J., Indraratna, B., McDowell, G., and Christie, D. (2007). Effect of confining pressure on ballast degradation and deformation under cyclic triaxial loading. *Géotechnique*, 57:527–536.

[115] Lai, C., Callerio, A., Faccioli, E., and Martino, A. (2000). Mathematical modelling of railway-induced ground vibrations. In *Proceedings of the International Workshop Wave 2000*, pages 99–110.

[116] Lai, Z., Jiang, L., and Zhou, W. (2018). An analytical study on dynamic response of multiple simply supported beam system subjected to moving loads. *Shock and Vibration*, 2018:1–14.

[117] Lamb, H. (1904). On the propagation of tremors over the surface of an elastic soild. *Philosophical Transactions of the Royal Society of London. Series A, Containing Papers of a Mathematical or Physical Character*, 203:1–42.

[118] Lefeuve-Mesgouez, G., LE HOUÉDEC, D., and Peplow, A. (2000). Ground vibration in the vicinity of a high-speed moving harmonic strip load. *Journal of Sound and Vibration*, 231:1289–1309.

[119] Lefeuve-Mesgouez, G., Peplow, A., and Le Houédec, D. (2002). Surface vibration due to a sequence of high speed moving harmonic rectangular loads. *Soil Dynamics and Earthquake Engineering*, 22:459–473.

[120] Liao, W.-I., Teng, T.-J., and Yeh, C.-S. (2005). A method for the response of an elastic half-space to moving sub-Rayleigh point loads. *Journal of Sound and Vibration*, 284:173–188.

[121] Lin, M.-L. and Huang, T.-H. (1996). The effects of frequency on damping properties of sand. *Soil dynamics and earthquake engineering*, 15:269–278.

[122] Lombaert, G. and Degrande, G. (2009). Ground-borne vibration due to static and dynamic axle loads of InterCity and high-speed trains. *Journal of Sound and Vibration*, 319:1036–1066.

[123] Lombaert, G., Degrande, G., Kogut, J., and François, S. (2006). The experimental validation of a numerical model for the prediction of railway induced vibrations. *Journal of Sound and Vibration*, 297:512–535.

[124] Loubinoux, J. (2018). High speed lines in the world. *International Union of Railways, UIC*.

[125] Lu, M. and McDowell, G. (2006). The importance of modeling ballast particle shape in the discrete element method. *Granular Matter*, 1:69–80.

[126] Lu, M. and McDowell, G. (2010). Discrete element modelling of railway ballast under monotonic and cyclic triaxial loading. *Géotechnique*, 60:459–467.

[127] Lysmer, J. and Waas, G. (1972). Shear waves in plane infinite structures. *Journal of Engineering and Mechanics Division, ASCE*, 98:85–105.

[128] Madshus, C. and Kaynia, A. (2000). High-speed railway lines on soft ground: Dynamic behaviour at critical train speed. *Journal of Sound and Vibration*, 231:689–701.

[129] Mann, A. (2002). DYNATRACK: A survey of dynamic railway track properties and their quality. Technische Universiteit Delft.

[130] Mazilu, T. (2007). Green's functions for analysis of dynamic response of wheel/rail to vertical excitation. *Journal of Sound and Vibration*, 306:31–58.

[131] McHenry, M. (2013). Pressure measurement at the ballast-tie interface of railroad track using matrix based tactile surface sensors. University of Kentucky.

[132] Mendes, P., Alves Costa, P., Godinho, L., and Lopes, P. (2015). 2.5D MFS-FEM model for the prediction of vibrations due to underground railway traffic. *Engineering Structures*, 104:141–154.

[133] Mezher, S., Connolly, D., Woodward, P., Laghrouche, O., Pombo, J., and Alves Costa, P. (2015). Railway critical velocity – Analytical prediction and analysis. *Transportation Geotechnics*, 6:84–96.

[134] Müller, K., Grundmann, H., and Lenz, S. (2008). Nonlinear interaction between a moving vehicle and a plate elastically mounted on a tunnel. *Journal of Sound and Vibration*, 310:558–586.

[135] Morales-Ivorra, S., Irene Real, J., Hernández, C., and Montalbán-Domingo, L. (2016). Derailment risk and dynamics of railway vehicles in curved tracks: Analysis of the effect of failed fasteners. *Journal of Modern Transportation*, 24:38–47.

[136] Nguyen, V.-H., Duhamel, D., and Nedjar, B. (2003). A continuum model for granular materials taking into account the no-tension effect. *Mechanics of Materials*, 35:955–967.

[137] Ni, T., Huang, Y.-H., and Lo, K.-F. (2011). An automatic procedure for train speed evaluation by the dominant frequency method. *Computers & Geotechnics*, 38:416–422.

[138] O'Brien, J. and Rizos, D. (2005). A 3D BEM-FEM methodology for simulation of high speed train induced vibrations. *Soil Dynamics and Earthquake Engineering*, 25:289–301.

[139] Olivier, B., Connolly, D., Alves Costa, P., and Kouroussis, G. (2016). The effect of embankment on high speed rail ground vibrations. *International Journal of Rail Transportation*, 4:229–246.

[140] Pakbaz, M., Mehdizadeh, R., M, V., and Bagherinia, K. (2009). Numerical prediction of subway induced vibrations: Case study in Iran-Ahwaz city. *Journal of Applied Sciences*, 9:2001–2015.

[141] Patil, S. (1987). Response of infinite railroad track to vibrating mass. *Journal of Engineering Mechanics*, 114:688–703.

[142] Picoux, B. and Le Houedec, D. (2005). Diagnosis and prediction of vibration from railway trains. *Soil Dynamics and Earthquake Engineering*, pages 905–921.

[143] Picoux, B., Rotinat, R., Regoin, J.-P., and Le Houédec, D. (2003). Prediction and measurements of vibrations from a railway track lying on a peaty ground. *Journal of Sound and Vibration*, pages 575–589.

[144] Powrie, W., Yang, L., and Clayton, C. (2007). Stress changes in the ground below ballasted railway track during train passage. *Proceedings of The Institution of Mechanical Engineers Part F-journal of Rail and Rapid Transit - PROC INST MECH ENG F-J RAIL R*, 221:247–262.

[145] Richart, F., Hall, T., and Woods, R. (1970). Vibrations of soils and foundations. *Englewood Cliffs, New Jersey: Prentice-Hall, Inc*.

[146] Rieckh, G., Kreuzer, W., Waubke, H., and Balazs, P. (2012). A 2.5D-Fourier-BEM model for vibrations in a tunnel running through layered anisotropic soil. *Engineering Analysis with Boundary Elements*, 36:960–967.

[147] Saikia, A. and Das, U. (2014). Analysis and design of open trench barriers in screening steady-state surface vibrations. *Earthquake Engineering and Engineering Vibration*, 13:545–554.

[148] Santos, J. and Correia, A. (2000). Shear modulus of soils under cyclic loading at small and medium strain level. *12th World Conference on Earthquake Engineering*, 530:90–98.

[149] Santos, N., Colaço, A., Alves Costa, P., and Calçada, R. (2016). Experimental analysis of track-ground vibrations on a stretch of the Portuguese railway network. *Soil Dynamics and Earthquake Engineering*, 90:358–380.

[150] Sheng, X., Jones, C., and Petyt, M. (1999a). Ground vibration generated by a harmonic load acting on a railway track. *Journal of Sound and Vibration*, 225:3–28.

[151] Sheng, X., Jones, C., and Petyt, M. (1999b). Ground vibration generated by a harmonic load acting on a railway track. *Journal of Sound and Vibration*, 225:3–28.

[152] Sheng, X., Jones, C., and Thompson, D. (2003). A comparison of a theoretical model for quasi-statically and dynamically induced environmental vibration from trains with measurements. *Journal of Sound and Vibration*, 267:621–635.

[153] Sheng, X., Jones, C., and Thompson, D. (2004). A theoretical study on the influence of the track on train-induced ground vibration. *Journal of Sound and Vibration*, 272:909–936.

[154] Sheng, X., Jones, C., and Thompson, D. (2005). Responses of infinite periodic structures to moving or stationary harmonic loads. *Journal of Sound and Vibration*, 282:125–149.

[155] Sheng, X., Jones, C., and Thompson, D. (2006). Prediction of ground vibration from trains using the wavenumber finite and boundary element methods. *Journal of Sound and Vibration*, 293:575–586.

[156] Shih, J.-Y., Thompson, D., and Zervos, A. (2016). The effect of boundary conditions, model size and damping models in the finite element modelling of a moving load on a track/ground system. *Soil Dynamics and Earthquake Engineering*, 89:12–27.

[157] Shih, J.-Y., Thompson, D., and Zervos, A. (2017). The influence of soil nonlinear properties on the track/ground vibration induced by trains running on soft ground. *Transportation Geotechnics*, 11:1–16.

[158] Steenbergen, M. and Metrikine, A. (2007). The effect of the interface conditions on the dynamic response of a beam on a half-space to a moving load. *European Journal of Mechanics - A/Solids*, 26:33–54.

[159] Steenbergen, M., Metrikine, A., and Esveld, C. (2007). Assessment of design parameters of a slab track railway system from a dynamic viewpoint. *Journal of Sound and Vibration*, 306:361–371.

[160] Tadeu, A. and Kausel, E. (2000). Green's functions for two-and-a-half-dimensional elastodynamic problems. *Journal of Engineering Mechanics*, 126:484–491.

[161] Takemiya, H. (2003). Simulation of track-ground vibrations due to a high-speed train: The case of X-2000 at Ledsgard. *Journal of Sound and Vibration*, 261:503–526.

[162] Takemiya, H. and Bian, X. (2005). Substructure simulation of inhomogeneous track and layered ground dynamic interaction under train passage. *Journal of Engineering Mechanics-asce - J ENG MECH-ASCE*, 131:699–711.

[163] Taniguchi, E. and Okada, S. (1981). Reduction of ground vibrations by improving soft ground. *Soil and Foundations*, 21:99–113.

[164] Thach, P.-N., Liu, H.-L., and Kong, G.-Q. (2013). Vibration analysis of pile-supported embankments under high-speed train passage. *Soil Dynamics and Earthquake Engineering*, 55:92–99.

[165] Thom, N., R. McDowell, G., F. Brown, S., and V. Brodrick, B. (2007). The Nottingham railway test facility, UK. *Proceedings of The Institution of Civil Engineers-Transport*, 160:59–65.

[166] Thompson, D. (2008). Railway noise and vibration: Mechanisms, modelling and means of control. *Elsevier Science*.

[167] Thomson, W. (1950). Transmission of elastic waves through a stratified solid medium. *Journal of Applied Physics*, 21:89 – 93.

[168] Tzanakakis, K. (2012). The railway track and its long term behaviour. *Springer Tracts on Transportation and Traffic: STTT*.

[169] Uzan, J. (1985). Characterization of granular materialss. *Transportation Research Record*, 1022:52–59.

[170] Varandas, J., Paixão, A., Fortunato, E., and Hölscher, P. (2016). A numerical study on the stress changes in the ballast due to train passages. *Procedia Engineering*, 143:1169–1176.

[171] Varandas, J. N. (2013). Long-term behaviour of railway transitions under dynamic loading. Universidade Nova De Lisboa. *Transportation Research Record.*

[172] Vucetic, M. and Dobry, R. (1991). Effect of soil plasticity on cyclic response. *Journal of Geotechnical Engineering*, 117:89–107.

[173] Waas, G. (1972). Linear two-dimensional analysis of soil dynamics problems in semi-infinite layered media. Berkeley, University of California.

[174] Wang, J. and Zeng, X. (2004). Numerical simulations of vibration attenuation of high-speed train foundations with varied trackbed underlayment materials. *Journal of Vibration and Control*, 10:1123–1136.

[175] Watts, T. J. (2018). Direct measurement of crosstie-ballast interface pressures using granular material pressure cells. University of Kentucky.

[176] Wolf, J. (2003). The scaled boundary finite element method. *John Wiley and Sons Inc*.

[177] Woodward, P., Laghrouche, O., Mezher, S., and Connolly, D. (2015). Application of coupled train-track modelling of critical speeds for high-speed trains using three-dimensional non-linear finite elements. *International Journal of Railway Technology*, 4:1–35.

[178] Xia, H., Cao, Y., and De Roeck, G. (2010). Theoretical modeling and characteristic analysis of moving-train induced ground vibrations. *Journal of Sound and Vibration*, 329:819–832.

[179] Yang, L., Powrie, W., and Priest, J. (2009). Dynamic stress analysis of a ballasted railway track bed during train passage. *Journal of Geotechnical and Geoenvironmental Engineering*, 135:680–689.

[180] Yang, Y. and Hung, H. H. (1997). A parametric study of wave barriers for reduction of train-induced vibrations. *International Journal for Numerical Methods in Engineering*, 40:3729–3747.

[181] Yang, Y. and Hung, H. H. (2001). 2.5D finite/infinite element approach for modelling visco-elastic bodies subjected to moving loads. *International Jornal for Numerical Methods in Engineering*, 51:1317–1336.

[182] Yang, Y. and Hung, H. H. (2008). Soil vibrations caused by underground moving trains. *Journal of Geotechnical and Geoenvironmental Engineering - J GEOTECH GEOENVIRON ENG*, 134:1633–1644.

[183] Yang, Y., Hung, H. H., and Chang, D. (2003). Train-induced wave propagation in layered soils using finite/infinite element simulation. *Soil Dynamics and Earthquake Engineering*, 23:263–278.

[184] Yoshida, N., Kobayashi, S., Suetomi, I., and Miura, K. (2002). Equivalent linear method considering frequency dependent characteristics of stiffness and damping. *Soil Dynamics and Earthquake Engineering*, 22:205–222.

[185] Zhai, W., CAI, C., and GUO, S. (1996). Coupling model of vertical and lateral vehicle/track interactions. *Vehicle System Dynamics*, 26:61–79.

[186] Zhai, W., He, Z., and Song, X. (2011). Prediction of high-speed train induced ground vibration based on train-track-ground system model. *Earthquake Engineering and Engineering Vibration*, 9:545–554.

[187] Zhai, W., Wang, K., and Cai, C. (2009). Fundamentals of vehicle–track coupled dynamics. *Vehicle System Dynamics*, 47:1349–1376.

[188] Zhai, W., Wang, K., and Lin, J. (2004). Modeling and experiment of railway ballast vibrations. *Journal of Sound and Vibration*, 270:673–683.

[189] Zhang, J., Andrus, R., and Juang, C. (2005). Normalized shear modulus and material damping ratio relationships. *Journal of Geotechnical and Geoenvironmental Engineering*, 131:453–464.

[190] Zhang, S., Xiao, X., Wen, Z., and Jin, X. (2008). Effect of unsupported sleepers on wheel/rail normal load. *Soil Dynamics and Earthquake Engineering*, 28:662–673.

Appendix A

Dynamic Flexibility Matrix

To introduce the concept of dynamic flexibility matrix, a stratified subgrade with horizontally parallel layers is used in this work. Referring to Figure A.1, let Point A be the origin point on the surface of the subgrade and Point B be located at the top of any stratum of the medium. Suppose a unit harmonic load $e^{i\omega t}$, where $i = \sqrt{-1}$, ω is the angular frequency, acts at Point A in each Cartesian coordinate direction.

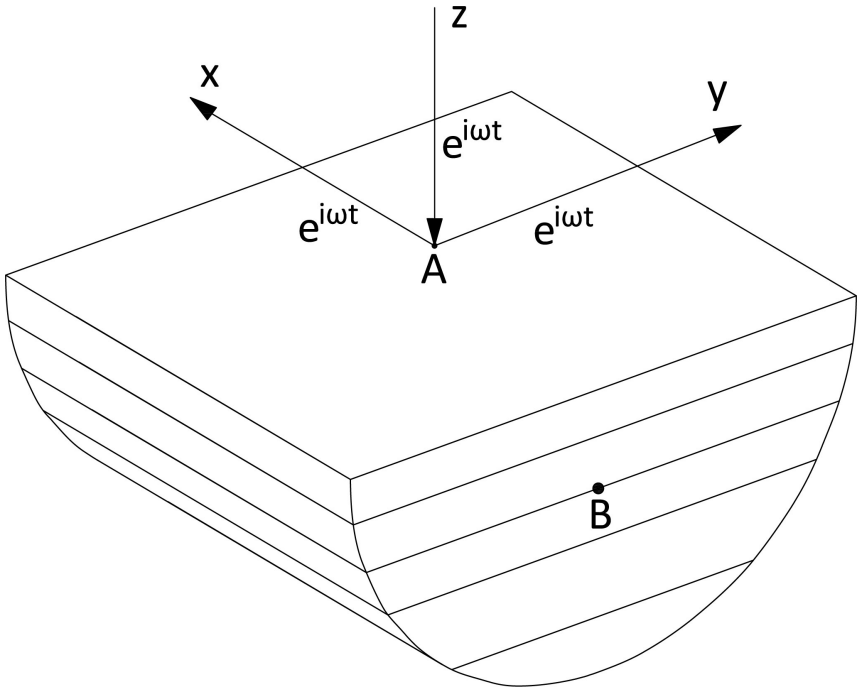

Fig. A.1 The coordinate system with horizontally parallel layers

When the unit harmonic load acts at Point A in the x dicrection, the steady state displacement amplitudes of Point B in x, y, z directions, are denoted by Q_{11}, Q_{21} and Q_{31}, respectively. Similarly, when the unit harmonic acts at Point A in the y direction, the amplitudes are denoted by Q_{12}, Q_{22}, Q_{32} and when it acts in

the z direction, the amplitudes are then Q_{13}, Q_{23}, Q_{33}. These amplitudes can be summed up in a matrix, $[Q]$, which can be defined as:

$$[Q] = \begin{bmatrix} Q_{11} & Q_{12} & Q_{13} \\ Q_{21} & Q_{22} & Q_{23} \\ Q_{31} & Q_{32} & Q_{33} \end{bmatrix} \tag{A.1}$$

The matrix defined in Equation A.1 is often referred to as the *dynamic flexibility matrix* of A to B. It means that the unit harmonic load acts at the Point A at the top of the surface and the displacements are for the Point B on the top of the horizontal layer in the subgrade. Generally, the matrix Q is complex and it is also called the *displacement Green's function*.

Assume that the harmonic load distributions, $p_x(x,y)e^{i\omega t}$, $p_y(x,y)e^{i\omega t}$ and $p_z(x,y)e^{i\omega t}$, act in the x,y,z directions respectively. The displacement amplitudes of Point B(x, y) is then given by:

$$\begin{pmatrix} u_{x,B}(x,y,\omega) \\ u_{y,B}(x,y,\omega) \\ u_{z,B}(x,y,\omega) \end{pmatrix} = \int_{-\infty}^{\infty}\int_{-\infty}^{\infty} [Q(x-\xi, y-\zeta, \omega)] \begin{pmatrix} p_x(\xi,\zeta) \\ p_y(\xi,\zeta) \\ p_z(\xi,\zeta) \end{pmatrix} d\xi d\zeta \tag{A.2}$$

Equation A.2 is a convolution integration. Taking advantage of Fourier transform,

$$\begin{cases} \tilde{f}(k_x) = \int_{-\infty}^{\infty} f(x) e^{-ik_x x} dx \\ \tilde{f}(k_x, k_y) = \int_{-\infty}^{\infty}\int_{-\infty}^{\infty} f(x,y) e^{-i(k_x x + k_y y)} dxdy \end{cases} \tag{A.3}$$

Equation A.3 can be transformed into the wavenumber-frequency domain:

$$\begin{pmatrix} \tilde{u}_{x,B}(k_x,k_y,\omega) \\ \tilde{u}_{y,B}(k_x,k_y,\omega) \\ \tilde{u}_{z,B}(k_x,k_y,\omega) \end{pmatrix} = [\tilde{Q}(k_x,k_y,\omega)] \begin{pmatrix} \tilde{p}_x(k_x,k_y) \\ \tilde{p}_y(k_x,k_y) \\ \tilde{p}_z(k_x,k_y) \end{pmatrix} \tag{A.4}$$

As can be seen from Equation A.4, all the quantities involved are in the transformed domain, therefore the matrix $\tilde{Q}(k_x,k_y,\omega)$ is often referred to as the *Fourier transformed dynamic flexibility matrix*.

Similar to the way $[Q]$ matrix is established, the concept can also be expanded to other quantities other than displacements, such as strain or stress. It means that the corresponding strain/stress transfer matrix in

the transformed domain can be constructed and it allows stresses/strains induced in all layers to be computed at any request from the author.

Appendix B

Equivalent Stiffness Formulation

The distribution of vertical stresses in the longitudinal direction of the track and along the subgrade interface is complicated. It is conditioned by the interaction between the two media. One way to solve it is to assume that the compatibility of displacements of two media is achieved by forcing the vertical displacement of the subgrade interface equal to the vertical displacement of the center line of the track, as shown in Figure 3.4. The other way to solve the media interaction problem is to assume that the compatibility of displacements at the interface is established by the average displacements in the cross section of the area, as shown in Figure 3.5.

For both interaction models presented, it should be noted that the distribution of track-subgrade interaction stresses is uniform throughout the track width is assumed. In foundation eigineering, this type of assumpttion is generally considered as a flexible foundation. According to Alves Costa [1], when the thickness of the granular layer is sufficient to permit the degradation of the action applied by the train, the first interaction model should lead to satisfactory results. However, in other situations where the transverse stiffness of the track, whether provided by the sleepers or the reinforced concrete slab (in slab track), induces a smoothing of displacements at the track-subgrade interface, the second interaction model returns more accurate outcome in the track dynamics analysis.

Equivalent stiffness for ballasted track

Assuming the track line is coincident with x-axis and b is the half width of ballasted track, the boundary condition, as defined in the work of Alves Costa [1], for the interaction problem can be mathematically defined as:

$$|y| \leq b \begin{cases} \sigma_{zz}(x,y,0,t) = \frac{F_g(x,t)}{2b} \\ u_z(x,0,0,t) = u_{bb}(x,t) \\ \sigma_{xz}(x,y,0,t) = \sigma_{yz}(x,y,0,t) = 0 \end{cases} \tag{B.1}$$

$$|y| > b \begin{cases} \sigma_{zz}(x,y,0,t) = \sigma_{xz}(x,y,0,t) = \sigma_{yz}(x,y,0,t) = 0 \end{cases} \tag{B.2}$$

Where F_g represents the interaction force on the boundary; u_{bb} is the vertical displacement of the lower track that interacts; u_z represents the vertical displacement at the subgrade interface.

Transforming the Equation B.1 to the frequency-wavenumber domain returns:

$$\begin{cases} \tilde{\sigma}_{zz}(k_x,k_y,0,\omega) = \tilde{F}_g(k_x,\omega)\frac{\sin(k_y b)}{k_y b} \\ \frac{1}{2\pi}\int_{-\infty}^{\infty} \tilde{u}_z(k_x,k_y,0,\omega)dk_y = \tilde{u}_{bb}(k_x,\omega) \\ \tilde{\sigma}_{xz}(k_x,k_y,0,\omega) = \tilde{\sigma}_{yz}(k_x,k_y,0,\omega) = 0 \end{cases} \tag{B.3}$$

Taking into account the Green's function in the transformed domain, the vertical displacement at the subgrade interface induced by the action described in Equation B.3 is given by:

$$\tilde{u}_z(k_x,k_y,0,\omega) = \tilde{u}_{zz}^G(k_x,k_y,0,\omega)\tilde{F}_g(k_x,\omega)\frac{\sin(k_y b)}{k_y b} \tag{B.4}$$

Where u_{zz}^G represents the Green's function in the frequency-wavenumber domain related to the vertical displacement induced by a vertical force with harmonic frequency ω.

By substituting Equation B.4 into Equation B.3, it can be concluded that:

$$\tilde{u}_{bb}(k_x,\omega) = \tilde{u}_z(k_x,0,0,\omega)\tilde{F}_g(k_x,\omega)\frac{\sin(k_y b)}{k_y b} \tag{B.5}$$

Given that the interaction force in the model is defined by the equivalent stiffness, the Equation B.5 can be re-arranged as:

$$\tilde{F}_g(k_x,\omega) = \tilde{k}_{eq}(k_x,\omega)\tilde{u}_{bb}(k_x,\omega) \tag{B.6}$$

Therefore, the equivalent stiffness k_{eq} can be expressed mathematically as:

$$\tilde{k}_{eq}(k_x,\omega) = \frac{2\pi}{\int_{-\infty}^{+\infty}\tilde{u}_{zz}^{G}(k_x,k_y,z=0,\omega)\frac{\sin(k_y b)}{k_y b}dk_y} \tag{B.7}$$

The equivalent stiffness relies on the wavenumber and frequency. The real part of the equivalent stiffness represents the rigidity of the subgrade, while the imaginary part refers to the damping.

Equivalent stiffness for slab track

Due to the different assumptions on the compatibility on the interface, the boundary condition used to solve the dynamic interaction problem of the slab track is given as follows:

$$|y| \leq b \begin{cases} \sigma_{zz}(x,y,0,t) = \frac{F_g(x,t)}{2b} \\ \frac{1}{2\pi}\int_{-b}^{b} u_z(x,y,0,t)dy = u_{bb}(x,t) \\ \sigma_{xz}(x,y,0,t) = \sigma_{yz}(x,y,0,t) = 0 \end{cases} \tag{B.8}$$

$$|y| > b \begin{cases} \sigma_{zz}(x,y,0,t) = \sigma_{xz}(x,y,0,t) = \sigma_{yz}(x,y,0,t) = 0 \end{cases} \tag{B.9}$$

Transforming the Equation B.8 to the frequency-wavenumber domain gives:

$$\begin{cases} \tilde{\sigma}_{zz}(k_x,k_y,0,\omega) = \tilde{F}_g(k_x,\omega)\frac{\sin(k_y b)}{k_y b} \\ \frac{1}{2\pi}\frac{1}{2b}\int_{-\infty}^{\infty}\int_{-b}^{b}\tilde{u}_z(k_x,k_y,0,\omega)e^{ik_y y}dydk_y = \tilde{u}_{bb}(k_x,\omega) \\ \tilde{\sigma}_{xz}(k_x,k_y,0,\omega) = \tilde{\sigma}_{yz}(k_x,k_y,0,\omega) = 0 \end{cases} \tag{B.10}$$

As seen from the result above, the only difference between Equation B.3 and Equation B.10 lies in the compatibility of displacements between the lower track and subgrade interface. Similarly, Equation B.10 can be re-written as:

$$\tilde{u}_{bb}(k_x,\omega) = \frac{1}{2\pi}\frac{1}{2b}\int_{-\infty}^{\infty}\int_{-b}^{b}\tilde{u}_z(k_x,k_y,0,\omega)\frac{\sin(k_y b)}{k_y b}e^{ik_y y}dydk_y\tilde{F}_g(k_x,\omega) \tag{B.11}$$

$$\tilde{u}_{bb}(k_x,\omega) = \frac{1}{2\pi}\frac{1}{2b}\int_{-\infty}^{\infty}\tilde{u}_z(k_x,k_y,0,\omega)\frac{\sin(k_y b)}{k_y b}\int_{-b}^{b}e^{ik_y y}dydk_y\tilde{F}_g(k_x,\omega) \tag{B.12}$$

Integrating over y gives:

$$\tilde{u}_{bb}(k_x,\omega) = \frac{1}{2\pi}\frac{1}{2b}\int_{-\infty}^{\infty}\tilde{u}_z(k_x,k_y,0,\omega)\frac{\sin(k_y b)}{k_y b}\frac{e^{ik_y b}-e^{-ik_y b}}{ik_y}dk_y\tilde{F}_g(k_x,\omega) \tag{B.13}$$

The displacement of the lower track in the frequency-wavenumber domain can then become:

$$\tilde{u}_{bb}(k_x,\omega) = \frac{1}{2\pi}\int_{-\infty}^{\infty}\tilde{u}_z(k_x,k_y,0,\omega)\frac{\sin(k_y b)^2}{(k_y b)^2}dk_y\tilde{F}_g(k_x,\omega) \tag{B.14}$$

The equivalent stiffness k_{eq} can be calculated as:

$$\tilde{k}_{eq}(k_x,\omega) = \frac{2\pi}{\int_{-\infty}^{+\infty}\tilde{u}_{zz}^{G}(k_x,k_y,z=0,\omega)\frac{\sin(k_y b)^2}{(k_y b)^2}dk_y} \tag{B.15}$$